Rotor Profiling and Performance Modelling of Internally Geared Screw Machines

Submitted by

Halil Lacevic

PhD Thesis

January, 2026

Centre for Compressor Technology

School of Science and Technology

City St George's, University of London

Sapere aude

Horace

Contents

List of Figures

List of Tables

Acknowledgements

Coming from an electrical engineering background, undertaking research in the niche field of screw compressor technology has been both a demanding and deeply rewarding journey. It challenged me to adapt quickly, to learn new foundations, and to apply my existing skills in a meaningful way to help push the boundaries of internally geared screw machines. I feel genuinely fortunate to have worked at the intersection of disciplines in real engineering applications, and to have learned from experts whose knowledge and standards continually raised my own.

I am especially grateful to my supervisors, Dr. Matthew Read and Prof. Ahmed Kovacevic, not only for their guidance, but for their unwavering support and encouragement throughout my study. Their trust, honesty, and high expectations pushed me to exceed what I thought I was capable of, and I am proud to have worked alongside them as colleagues and, above all, as friends. I am also sincerely thankful to Prof. Nikola Stosic, whose support during difficult moments meant more than I can express, and whose encouragement helped me continue.

This work would not have been possible without the financial and technical support provided by Carrier Global Corporation and PDM Analysis Ltd. I am grateful for their continued confidence in this research and for the practical insight that helped keep it grounded in industrial reality.

Finally, none of this would have mattered or been achievable without the love and support of my family and friends. To my mother, father, and sister: thank you for your patience, belief, and constant encouragement.

I am grateful to the United Kingdom, and to City St George's, University of London, for the opportunity to pursue this degree and for welcoming me into its higher education community. Lastly, to my home country, Bosnia and Herzegovina, I dedicate this work to you, and to the generations who will continue to learn, build, and lead the future.

Declaration

I declare that this thesis is my own work and has not been submitted in any form for another degree or diploma at any university or other institution. Where other sources of information have been used, they have been acknowledged.

I agree for this work to be submitted to the Institutional Repository of City St George's, University of London for use in accordance with the Thesis Deposit Agreement.

Halil Lacevic

London, United Kingdom, January 2026

Abstract

Screw machines are widely used in industrial applications for gas compression and transport, including refrigeration systems, compressed air supply, heat pumps, and process industries. Among them, conventional twin screw compressors are a mature technology with a long history of development and analysis. Internally geared screw machines (IGSMs) are a more recent alternative in which one rotor operates inside another on parallel offset axes. This arrangement differs fundamentally from the side-by-side rotor layout of conventional twin screw machines and may offer new opportunities for machine design and performance improvement. However, research on IGSMs remains limited and has mainly focused on geometric feasibility and simplified performance predictions.

This thesis contributes to the development of IGSM technology through three main objectives. The first is the development of a detailed numerical geometry model for IGSMs, coupled with an established performance prediction framework. The second is the use of this modelling capability to carry out an initial assessment of IGSM performance through parametric studies and comparison with conventional screw machine designs. The third is the investigation of new rotor profiling methods, including extensions of the traditional rack generation method and the use of deep neural networks for rotor profile generation.

The main outcome of the thesis is a computationally efficient modelling framework that enables lower-cost simulation of IGSMs, together with initial design guidance and feasible rotor design pathways identified through systematic parametric studies. Overall, the work helps extend current understanding of IGSMs from early geometric concepts towards more practical tools for design and performance evaluation.

Keywords: internally geared screw machine; screw compressor; rotor profiling; geometry modelling; performance prediction; parametric study; deep neural networks.

Abbreviations

IGSM	internally geared screw machine
CFD	computational fluid dynamics
HVAC	heating ventilation and air conditioning
PCA	principal component analysis
GPR	Gaussian process regression
GAN	generative adversarial network
W-GAN	Wasserstein generative adversarial network

Nomenclature

$\lambda, \bar{\sigma}$	pin-generation non-dimensional profile parameters
ω_1	main rotor rotational speed
Φ_1	main rotor wrap angle
Φ_2	gate rotor wrap angle
$\rho_{p,1}, \varphi_{p,1}$	main rotor polar coordinates
$\rho_{p,2}, \varphi_{p,2}$	gate rotor polar coordinates
σ_1, σ_1^*	main rotor meshing condition solutions
σ_2, σ_2^*	gate rotor meshing condition solutions
θ	rotor profile parameter
φ_1	main rotor rotational angle
φ_2	gate rotor rotational angle
D_1	main rotor outer diameter
D_2	gate rotor outer diameter
E	axis distance
L	rotor length
m_{21}	gearing ratio
N_1	number of lobes on the main rotor
N_2	number of lobes on the gate rotor

r_{1w} main rotor pitch circle radius

r_{2w} gate rotor pitch circle radius

r_{r_1} main rotor root circle radius

S_1 main rotor local coordinate system

S_2 gate rotor local coordinate system

S_f global fixed coordinate system

S_r rack rotor local coordinate system

VI volume index

x_1, y_1 main rotor Cartesian coordinates

x_2, y_2 gate rotor Cartesian coordinates

x_{cf}, y_{cf} fillet contact loci Cartesian coordinates

x_{cm}, y_{cm} main contact loci Cartesian coordinates

1 Introduction

Positive displacement machines are mechanical devices designed to compress or transfer a working fluid (gas or liquid) by trapping a fixed volume within a chamber and mechanically displacing it through the system. This process is achieved either by reducing the chamber volume or by forcing the fluid to move through the motion of mechanical components [1].

Positive displacement machines can function as pumps, compressors, or expanders, and they are broadly classified according to their working principle into two categories: reciprocating and rotary. In reciprocating machines, compression or pumping is achieved through the linear motion of pistons or diaphragms within cylinders, where alternating suction and discharge strokes enable the intake and delivery of the working fluid. By contrast, rotary machines introduce continuous rotational motion of elements such as vanes or screws to displace fluid steadily through the chamber, thereby reducing pulsations and enabling compact, high-speed operation.

Among rotary positive displacement machines, one of the most applied configurations is the twin screw compressor. This device consists of two intermeshing helical rotors, commonly referred to as the main and gate rotors, enclosed within a fixed casing. The main rotor is typically driven directly by an external motor, while the gate rotor is rotated either by synchronising timing gears or by direct rotor contact, depending on whether the machine operates in an oil-free or oil-injected configuration [2]. The meshing action of the rotors forms a sequence of working chambers whose volume increases from zero to maximum and then decreases back to zero as they progress along the rotor length, resulting in the compression and delivery of the working fluid.

The Centre for Compressor Technology at City St George's, University of London has led pioneering research in recent years into a novel class of screw machines known as internally geared screw machines (IGSMs) [3–5]. These machines offer potential advantages over conventional twin screw configurations, including reduced leakage areas, co-directional thermal expansion, lower rotor deflection, reduced viscous losses, and a higher swept volume for a given machine envelope. Initial investigations have primarily focused on characterising the rotor geometry of IGSMs and understanding its influence on power transfer between rotors, porting losses, and leakage paths [4–6]. This research has led to the development of preliminary computational tools for geometry and performance analysis, based on simplified representations of the compression process. However, further work is required to develop detailed and robust numerical models capable of accurately

predicting performance and thus establishing a comprehensive understanding of the potential advantages offered by internally geared screw machines.

Previous research into profile generation for IGSMs has been inspired from gerotor pump design methods, including profiles generated from combinations of cycloidal curves (see Section 2.3.2) and pin-generated profiles (see Section 2.3.3), most commonly using circular pins to allow the analytical solution of the meshing condition. While most studies have focused on circular pins, it should be noted that any arbitrary curve can, in principle, serve as a generating element provided that the meshing condition is solved numerically [7], although this introduces additional challenges related to precision and computational efficiency. In contrast, the well-established rack method (see Section 2.3.1), which revolutionised the design of conventional twin screw machines by providing a more flexible and accurate approach to profile generation, has not yet been systematically applied to the design of internally geared rotors that maintain continuous contact.

As IGSM rotor profiles are required to maintain continuous contact between rotors while ensuring a zero minimum working chamber area, it is essential to define the conditions that guarantee these criteria are satisfied. These conditions are inherently linked to the *Fundamental Law of Gearing* (see Appendix A) and the relative motion between the rotors, defined through transformation of rotor points throughout rotation (see Appendix B).

As the rack method has historically offered significant design flexibility and performance benefits in conventional screw compressors, investigating its applicability and adaptation to internally geared configurations constitutes an important objective of this study. Furthermore, the recent emergence of deep learning and generative models in compressor world presents an opportunity to extend the traditional design space [8]. The potential for implementing deep neural networks to generate novel rotor profiles represents an innovative direction for advancing automated rotor design methodologies.

For conventional twin screw machines, a variety of performance prediction approaches exist, ranging from low-order numerical formulations to high-fidelity Computational Fluid Dynamics (CFD) simulations (see Section C). Although CFD provides detailed flow insights, its computational cost makes it unsuitable for parametric and optimisation studies. In contrast, one-dimensional multi-chamber models offer a computationally efficient means of performance prediction and have been widely applied to conventional designs. To enable similar analysis for internally geared screw machines, a

robust geometry model capable of rapidly and accurately evaluating key geometric parameters is required as an input to the chamber model. Therefore, one of the principal aims of this study is to develop such a geometry model for IGSMs, ensuring reliable computation of geometric quantities across a wide range of design parameters within the defined design space.

The developed geometry model will subsequently be integrated into the existing one-dimensional chamber model implemented in the in-house simulation software, `SCORG` [9], developed at City, St George's, University of London. Although full experimental validation will ultimately be pursued once the ongoing test rig development (particularly the manufacture of the complex outer rotor) is completed, preliminary validation will be achieved through comparison with high-fidelity CFD results for representative test cases. Integration of the new geometry model into the chamber model framework will enable comprehensive parametric and performance studies, allowing systematic evaluation of the performance characteristics of internally geared screw machines and a more complete understanding of their advantages relative to conventional twin screw compressors.

2 Literature Review

2.1 Conventional Twin Screw Machine

Twin screw compressors originated in the early twentieth century and became widely used by the 1960s across refrigeration, air, and process-gas duties [9–11]. Since then, sustained advances in manufacturing tolerance, surface finishing, and profile design have delivered higher efficiencies, lower energy consumption, and improved reliability, confirming their long established standing in rotary positive displacement practice.

Operation relies on two intermeshing helical rotors on parallel, offset axes. As the rotors counter-rotate, they create successive working chambers that take in low pressure gas at the intake, trap and compress it as the enclosed volume decreases, and release high pressure gas through the outlet, producing a smooth, nearly continuous flow along the rotor length [12]. Since the delivered flow is relatively insensitive to pressure ratio within a defined operating window, these machines serve applications requiring a stable, continuous supply in oil and gas, chemical processing, food and beverage, and heating, ventilation and air conditioning (HVAC).

In practice, designs are either oil free, using timing gears to synchronise the rotors (sometimes with water injection for lubrication and cooling) for contamination-sensitive applications, or oil injected, introducing oil into the working chambers to lubricate, seal clearances, and remove heat, with the gate rotor typically driven directly by the main rotor [13–15]. Each approach has trade off. Timing gears add complexity and cost in oil free systems, while oil injected systems must manage separation and potential contamination.

A more fundamental limitation arises from geometric scaling. Conventional rotor pairings impose a lower size bound. For example, VMC Italy's V60, among the smallest commercial twin screw compressors, has a main rotor outer diameter of roughly 60mm [16]. This restricts expansion into small capacity ranges that are often served by scroll compressors. These constraints motivate alternative architectures, notably the internally geared screw machine (IGSM), which seeks to relax geometric limits and extend screw technology benefits to smaller, high efficiency applications [6].

2.2 Internally Geared Screw Machine

Another class of positive displacement machines is the gerotor pump, commonly used in oil circulation applications such as lubrication systems and hydraulic motors [17, 18]. Inspired by the internal meshing concept of gerotor designs, the internally geared screw machine was introduced in recent years as a novel variant of the twin screw compressor [6, 19]. Unlike conventional twin screw machines, which consist of two externally geared rotors positioned side by side, IGSMs feature an inner (main) rotor and an outer (gate) rotor with one additional lobe. The outer rotor surrounds the inner rotor and meshes internally with it, while both rotors rotate in the same direction on parallel but offset axes.

In a similar manner to gerotor pumps, IGSMs must achieve continuous rotor-to-rotor contact throughout rotation to ensure effective chamber formation and sealing. However, unlike gerotor pumps, which operate solely as pumping devices, IGSMs must also satisfy the condition of a zero minimum working chamber area in order to achieve compression. Furthermore, whereas gerotor pumps typically employ straight rotors, IGSMs incorporate helical rotors. This combination of internal meshing and helical geometry enables the IGSM to function as a true screw compressor while possibly extending the design space beyond that of conventional externally meshing configurations. Figure 2.1 shows the principal components of an internally geared screw machine, while Figure 2.2 illustrates its cross-section.

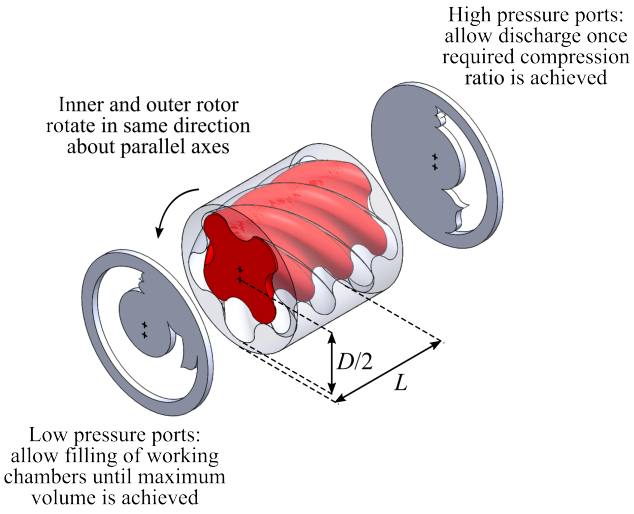

Figure 2.1: Illustration of the principal components of an internally geared screw machine [4].

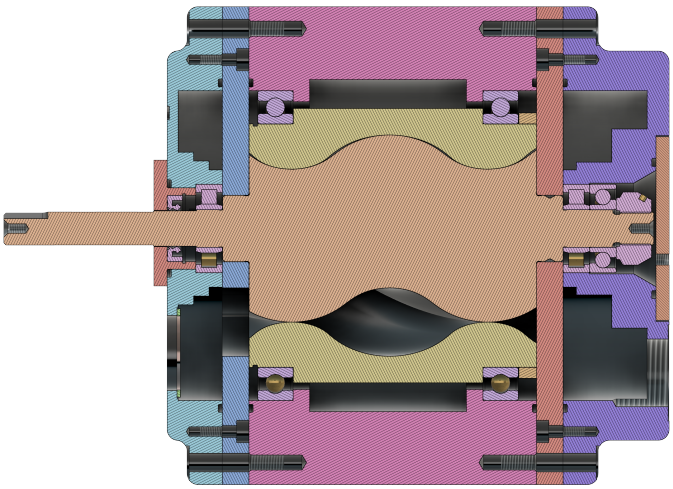

Figure 2.2: Cross sectional view of an internally geared screw machine.

IGSMs operate on the same fundamental working principles as conventional twin screw machines, relying on the continuous intake, compression, and release in the working chambers. However, the key differences is the rotor configuration, which in IGSM features internal rather than external meshing, and in the location of the working chambers, which in IGSMs are formed between the lobes of the inner and outer rotors. Additionally, inlet and outlet ports in IGSMs can only be arranged axially, in contrast to the radial port configuration used in conventional designs [6].

Internally geared screw machines offer several potential advantages over conventional twin screw compressors, particularly in compact and small-scale applications. One of the potential benefits is the reduction of internal leakage due to the fully enclosed rotor configuration and the potential for tighter sealing along the internal meshing surfaces [6]. A further advantage is the absence of a blowhole area, since the internal meshing and axial porting of IGSMs allow the design to eliminate the need for a blowhole, thereby possibly improving efficiency [6]. By overcoming the geometric constraints that limit the minimum size of conventional twin screw machines, IGSMs open the possibility of extending screw compressor technology into smaller capacity ranges, thereby offering potential competition to scroll compressors in compact applications.

Design of any rotary positive displacement machine begins with the definition of rotor profile shapes, which directly influence the machine's performance. However, before addressing the rotor profiling methods used in screw compressors, it is necessary to establish an understanding of rotor kinematics, including their motion, meshing, and relative positions.

The design process begins with the specification of the number of lobes on the rotors (main rotor: N_1, gate rotor: N_2) and their respective pitch circle radii (main rotor: r_{1w}, gate rotor: r_{2w}). These parameters are fundamental for determining the gearing ratio, $m_{21} = \frac{N_2}{N_1}$, and the centre distance E between the two rotors. The pitch circles represent the theoretical loci along which rotor lobes engage. The point of contact between the two circles, denoted as the pitch point $\mathbf{p}(p_x, p_y)$, is of particular importance as it ensures proper meshing and defines the instantaneous transfer of motion, where the velocities of both rotors are equal in magnitude and direction. If the pitch circles are externally tangent, the design corresponds to a conventional screw compressor, whereas if they are internally tangent, the system is classified as an internally geared screw machine.

In both conventional and internally geared screw compressor systems, three coordinate systems can be defined. The first, S_1, is a local system fixed to the main rotor, rotating with it. In internally geared screw machine configurations the main rotor may be either the inner or the outer rotor. However, for consistency, this study assumes the inner rotor as the main rotor. The second system, S_2, is also a local system but fixed to the gate rotor, which in internally geared screw machine corresponds to the outer rotor, and rotates accordingly. The third system, S_f, serves as the global or fixed coordinate system. It is fixed to the initial position of the main rotor and shares the same origin as S_1.

The S_2 system is offset from S_f by the centre distance E along the x-axis, where E corresponds to the distance between the two pitch circle centres. For conventional screw compressors, $E = r_{1w} + r_{2w}$, whereas for internally geared screw machines, $E = r_{2w} - r_{1w}$.

The three coordinate systems for each configuration are illustrated in Figure 2.3. In the internally geared configuration, both rotors rotate in the same direction (Figure 2.3 (a)), while in the conventional configuration they rotate in opposite directions (Figure 2.3 (b)). The angular positions of the rotors are related by the gearing ratio m_{21} such that $\varphi_1 = m_{21} \cdot \varphi_2$, where φ_1 and φ_2 denote the angular positions of the main and gate rotors, respectively.

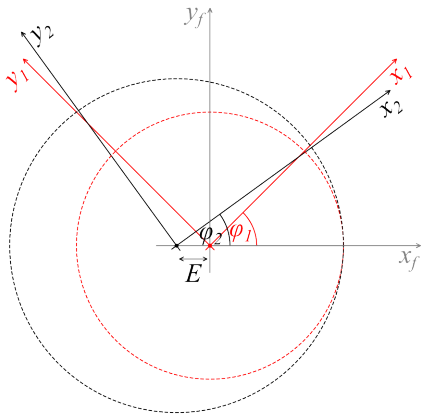

(a)

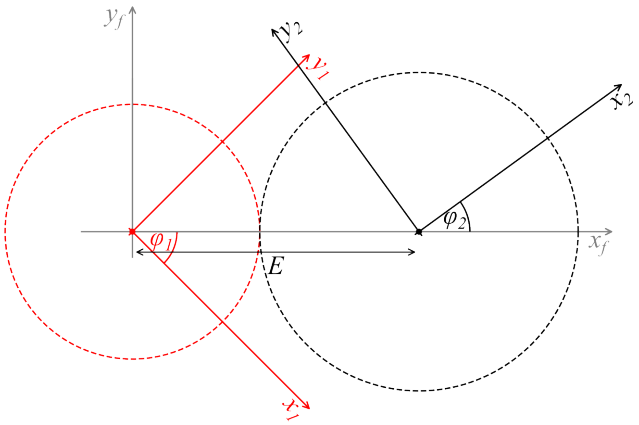

(b)

Figure 2.3: Two-dimensional representation of coordinate systems in screw compressor design: (a) internally geared system, (b) externally geared system. The main rotor local coordinate system is shown in red, the gate rotor local coordinate system in black, and the global coordinate system, fixed to the initial position of the main rotor, in grey.

2.3 Review of Profiling Methods

As early as 1961, Andreev [11] applied the envelope method, originally introduced in the 18^{th} century by Euler [20] and described in 1956 by Litvin [21], to the generation of screw compressor rotors and their tools. To date, three different generating methods for the rotor profiles of the twin screw compressor have been demonstrated [22–24]. The most popular method, illustrated numerically by Litvin and Feng [22], identifies the primary tooth profile curves on one screw rotor and then uses that rotor to generate the tooth profile of another rotor. More recently, Zaytsev and Infante Ferreira [23] proposed a differential method for rotor profile generation using a meshing line.

An alternative rack generation procedure for screw compressor rotors was first introduced in 1984 by Rinder [24]. However, in recent years, Rinder's profile has undergone significant modifications to improve the rotor tightness and reduce the blow-hole area. For example, Stosic and Hanjalic [25] overcame the large blow-hole area problem in rack-generated rotors by generating the high-pressure side of a rack using a rotor conjugate action that under-cuts a single appropriate curve on the rack.

A problem of blow-hole area present in the conventional twin screw machines is not considered in the internally-geared screw machines as there is no blow-hole area in this configuration, thus reducing the blow-hole area in rotor profiling for internally-geared screw machine does not have to be considered.

Various methods based on epitrochoidal curves for generating rotor geometry in gerotor applications have been described in previous studies [26–28]. While these methods are primarily employed to generate rotor profiles in gerotor pumps, alternative approaches incorporating non-circular pins and deviation functions have also been explored in several studies [29–31]. More recent studies on gerotor pumps have focused on generating rotor profiles to enhance performance and minimise wear [32, 33].

In earlier studies, Read et al. [6] proposed internally geared screw compressor rotor profiles based on combinations of epicycloid and hypocycloid curves, where the selection of profiles is limited. More recent studies on internally geared screw compressors [4, 34, 35] have adopted the method described by Vecchiato et al. [28], commonly referred to as the pin-generation method.

The method described by Vecchiato et al. [28] provides analytical solutions for generating rotors from predefined circular pins. By numerically solving the meshing condition, the method can be generalised to allow an arbitrary curve to be used as a pin [7]. Previously described methods focused on producing symmetric profiles predominantly. Asymmetric internally geared rotor profiles for positive displacement machines were recently proposed by Read [36] where a combination of circular pins is presented. Another approach for generating asymmetric rotor profiles was introduced by Genta et al. [37], utilising elliptical pins. Although asymmetric profiles have led to significant performance improvements in conventional twin screw machines, no clear advantage over symmetric profiles has yet been demonstrated for internally geared screw machines.

Although the rack method has long been established as a conventional profiling approach in the design of twin screw machines, it has not previously been applied to internally geared screw machines. Instead, most profiling methods reported for internally geared screw machines originate from gerotor pump geometry and may therefore be considered novel when viewed from the perspective of screw compressor rotor design. These include cycloidal approaches [6] and pin-generation based methods employing circular, arbitrary, or elliptical pins [7, 28, 36, 37]. Among these, the circular pin-generation method [28] has been used most extensively in recent internally geared screw machine studies [4, 34, 35], making it the current state-of-the-art. By contrast, the application of the rack method to internally geared screw machines, as explored in the present work, represents a new extension of a conventional twin screw profiling concept to this machine class.

2.3.1 Rack Method

The meshing condition plays a crucial role in both externally and internally geared designs. The externally geared design of rotor profiles in positive displacement machines has been extensively studied and widely applied, particularly in external spur pumps and conventional twin screw machines. The most commonly used method for generating externally geared rotor profiles involves designing a third rotor of infinite pitch radius, known as the *rack rotor*, which meshes with both the main and gate rotors. This approach, referred to as the *rack method*, is based on the principles of the *Envelope Theory* [38], originally developed within the field of differential geometry. The rack method was first introduced by Sakun [10] as a mathematical framework for defining the meshing condition, which must be satisfied by the meshing curve generated for a given pair of rotors.

Initially, the meshing condition between the rack and each rotor profile was solved analytically, imposing constraints on the selection of the meshing curve. The curve had to be analytically differentiable, limiting the options to simple geometric shapes such as circles, lines, and points. However, the advancements introduced by Stosic [39] significantly simplified the design process by proposing a numerical approach that employs central difference methods to solve the meshing condition and derive the meshing curve.

The introduction of numerical techniques to the rack method expanded the flexibility of meshing curve design, allowing for a broader range of profile shapes. This flexibility enables profile shapes to be defined through sections on the rack, facilitating the generation of various types of contact points at specific locations.

Although the meshing condition presented in Equation (A.5) may have multiple solutions for a single point on the rotor, in external gearing, such as the rotor profiles used in conventional twin screw machines, the selection of solutions is straightforward. It can be deduced that the roots of the equation always lie in the first and fourth quadrants of the rotor's local coordinate system [39]. The rack method is widely used to generate involute profiles, however, it has also played a significant role in developing highly efficient rotor profiles for conventional twin screw machines [25]. One of its key contributions to twin screw machines was the introduction of asymmetric rotor profiles, which improved sealing within working chambers operating under higher pressure differences.

The rack method for generation of screw compressor rotor profiles begins by defining the rack curve in the global coordinate system. For any given rack curve $\Big(x_r(\theta), y_r(\theta)\Big)$, the coordinates of the main and gate rotor profiles in conventional twin screw compressor or spur gears can be found using Equations (2.1) and (2.2), respectively. The transformation matrix that maps points from the rack rotor's local coordinate system to the local coordinate system of the main rotor is given in Equation (2.3). The transformation matrices that map points from the rack rotor's local coordinate system to the local coordinate systems of the externally and internally geared gate rotors are presented in Equations (2.4) and (2.5), respectively. The pitch circle radii of the main and gate rotors are denoted as r_{1w} and r_{2w}, while $\sigma_{r_i}, i = [1, 2]$ represents the solutions of the meshing condition between the rack and each corresponding rotor profile. The solutions to the meshing conditions, as described by Stosic [2], can be obtained using Equations (2.6) and (2.7). An illustration of the rack method, showing the rack curve and the corresponding derived main and

gate rotor single lobes, is provided in Figure 2.4.

$$\begin{bmatrix} x_1(\theta) & y_1(\theta) & 0 & 1 \end{bmatrix}^\top = \mathbf{M}_{r1}(\sigma_{r_1}) \begin{bmatrix} x_r(\theta) & y_r(\theta) & 0 & 1 \end{bmatrix}^\top \tag{2.1}$$

$$\begin{bmatrix} x_2(\theta) & y_2(\theta) & 0 & 1 \end{bmatrix}^\top = \mathbf{M}_{r2}(\sigma_{r_2}) \begin{bmatrix} x_r^{(1)}(\theta) & y_r(\theta) & 0 & 1 \end{bmatrix}^\top \tag{2.2}$$

$$x_r^{(1,I)}(\theta) = x_r(\theta) + E$$

$$x_r^{(1,C)}(\theta) = E - x_r(\theta)$$

$$\mathbf{M}_{r1}(\varphi_1) = \begin{bmatrix} \cos(\varphi_1) & -\sin(\varphi_1) & 0 & r_{1w}\varphi_1 \sin(\varphi_1) \\ \sin(\varphi_1) & \cos(\varphi_1) & 0 & -r_{1w}\varphi_1 \cos(\varphi_1) \\ 0 & 0 & 1 & 0 \\ 0 & 0 & 0 & 1 \end{bmatrix} \tag{2.3}$$

$$\mathbf{M}_{r2}^{(C)}(\varphi_2) = \begin{bmatrix} -\cos(\varphi_2) & \sin(\varphi_2) & 0 & -r_{2w}\varphi_2 \sin(\varphi_2) \\ \sin(\varphi_2) & \cos(\varphi_2) & 0 & -r_{2w}\varphi_2 \cos(\varphi_2) \\ 0 & 0 & 1 & 0 \\ 0 & 0 & 0 & 1 \end{bmatrix} \tag{2.4}$$

$$\mathbf{M}_{r2}^{(I)}(\varphi_2) = \begin{bmatrix} \cos(\varphi_2) & -\sin(\varphi_2) & 0 & r_{2w}\varphi_2 \sin(\varphi_2) \\ \sin(\varphi_2) & \cos(\varphi_2) & 0 & -r_{2w}\varphi_2 \cos(\varphi_2) \\ 0 & 0 & 1 & 0 \\ 0 & 0 & 0 & 1 \end{bmatrix} \tag{2.5}$$

$$\sigma_{r_1}(\theta) = \frac{y_r(\theta) - \dfrac{\partial x_r(\theta)}{\partial y_r(\theta)}\Big(r_{1w} - x_r(\theta)\Big)}{r_{1w}} \tag{2.6}$$

$$\sigma_{r_2}(\theta) = \frac{y_r(\theta) - \dfrac{\partial x_r(\theta)}{\partial y_r(\theta)}\Big(r_{2w} - x_r^{(1)}(\theta) - E\Big)}{r_{2w}} \tag{2.7}$$

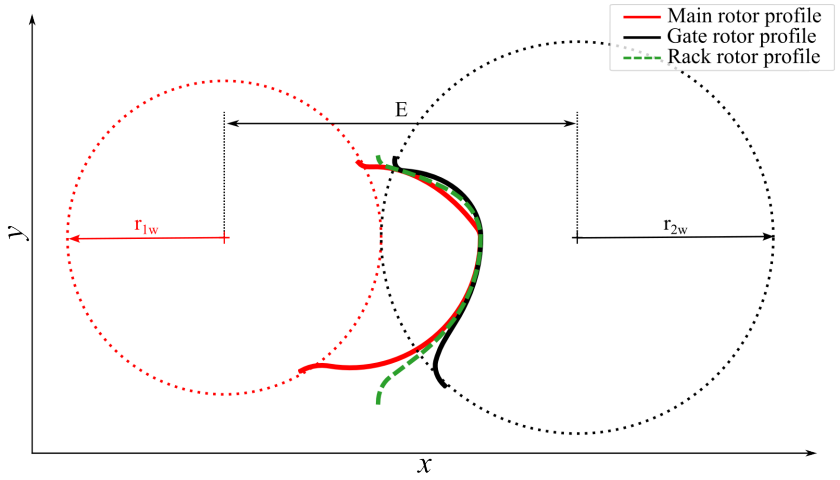

Figure 2.4: Illustration of the rack method, showing the rack single lobe together with the derived main and gate rotor single lobes.

The method constitutes a general gear-generation procedure that is widely applicable. It may be employed for the synthesis of twin screw compressor rotors, which can be regarded as helical gears with parallel axes. The formed tools used for rotor manufacturing correspond to crossed helical gears on non-parallel and non-intersecting axes, with a uniform lead in the case of hobbing, or with zero lead in the case of formed milling and grinding. Templates used for rotor inspection are identical to planar rotor hobs. In all these cases, the tool axes do not intersect the rotor axes.

The rack method is well established and commonly applied in the generation of rotor profiles for conventional twin screw machines. However, it has not previously been applied to the generation of IGSM rotors, where additional constraints must be satisfied, namely the requirement for continuous contact between the rotors and the condition of a zero minimum working chamber area.

2.3.2 Combination of Epicycloid and Hypocycloid Curves

To generate conjugate internally geared rotor profiles with continuous contact, one of the earliest approaches was the use of combined epicycloid and hypocycloid curves [6, 40]. In this method, a cycloidal curve is first defined in the local coordinate frame of one rotor (either S_1 or S_2), after which the meshing condition is applied to determine the conjugate curve in the local frame of the mating rotor. This procedure results in conjugate rotor pairs that maintain continuous contact between the generated profiles. It can be shown that when a cycloidal curve is used as the initial

profile, the resulting conjugate profile is itself a cycloid generated with respect to the corresponding rotor pitch circle (Figure 2.5).

Cycloidal based rotor profiles have previously been investigated in the context of gerotor pumps [27, 41–43], as well as in early studies of internally geared screw machines [6]. In such configurations, the generated profiles result in the inner rotor having one lobe fewer than the outer rotor. These profiles can be conveniently expressed as combinations of epicycloid and hypocycloid curve segments.

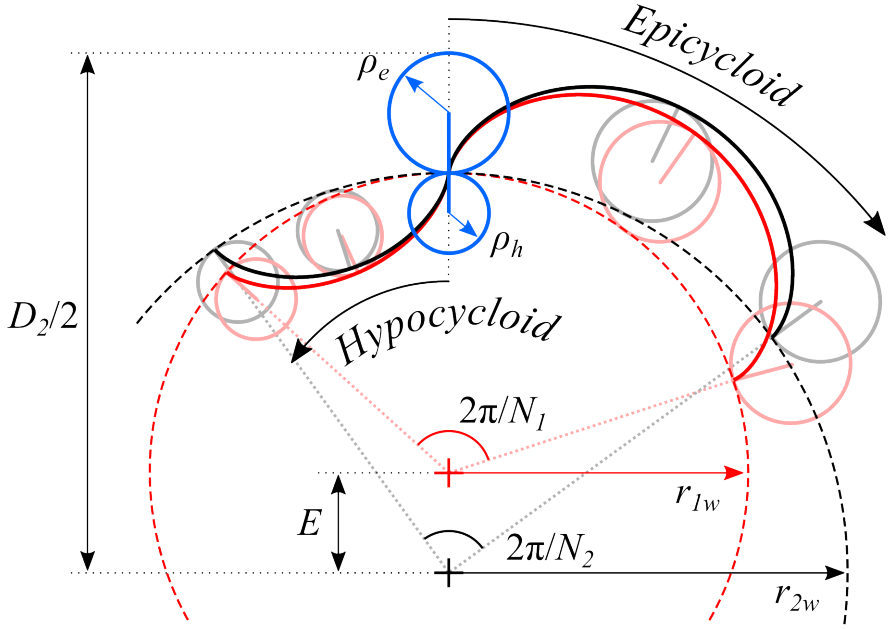

Figure 2.5: Illustration of the generation of conjugate inner (red) and outer (black) rotor lobe profiles using a combination of epicycloid and hypocycloid curves. The example shown corresponds to $N_2 = 4$, $N_1 = 3$, and $v = 0.6$ (hence $\rho_e/\rho_h = 1.5$).

The mathematical expressions describing the coordinates of the cycloidal sections of the main rotor profiles are presented in Equations (2.8) and (2.9).

$$\begin{bmatrix} x_e(\theta) \\ y_e(\theta) \end{bmatrix} = \begin{bmatrix} (r_{1w} + \rho_e)\cos\theta - \rho_e \cos\theta(\frac{r_{1w}}{\rho_e} + 1) \\ (r_{1w} + \rho_e)\sin\theta - \rho_e \sin\theta(\frac{r_{1w}}{\rho_e} + 1) \end{bmatrix} \tag{2.8}$$

$$\begin{bmatrix} x_h(\theta) \\ y_h(\theta) \end{bmatrix} = \begin{bmatrix} (r_{1w} - \rho_h)\cos\theta + \rho_e \cos\theta(\frac{r_{1w}}{\rho_h} - 1) \\ (r_{1w} - \rho_h)\sin\theta - \rho_h \sin\theta(\frac{r_{1w}}{\rho_h} - 1) \end{bmatrix} \tag{2.9}$$

Details of the profile generation method based on the combination of cycloid curves have previously been reported by Read et al. [5]. A summary is provided in Figure 2.5, where the profiles are characterised by the pitch circle radius, r_{1w}, the number of lobes, N_1, and the radius of the epicycloid generating circle, ρ_e, subject to the condition $0 \leq \rho_e \leq r_{1w}/N_1$. As illustrated in Figure 2.5, the parameters ρ_e and ρ_h are equal for both the inner and outer rotors, while the pitch circle radii are related by the gear ratio, $r_{2w}/r_{1w} = N_2/N_1$. A normalised rotor profile parameter, v, is accordingly defined in Equation (2.10).

$$v = \rho_e/E, \quad \text{where} \quad 0 \leq v \leq 1 \tag{2.10}$$

The admissible range of the profile parameter, $0 \leq v \leq 1$, corresponds to the limiting cases in which the rotor profiles are defined entirely by hypocycloid or epicycloid curves, respectively. The maximum profile diameter of the outer rotor, D_2, can be expressed as a function of the axis distance, E, the parameter v, and the number of lobes on the outer (gate) rotor, N_2, as shown in Equation (2.11). A more detailed geometrical analysis of internally geared screw machines with profiles generated from combined epicycloid and hypocycloid curves has been presented by Read et al. [5].

$$\frac{E}{D_2} = \frac{1}{2(N_2 + 2v)} \tag{2.11}$$

2.3.3 Pin-generation Method

The shape of rotor profiles generated using circular pins is defined by two key non-dimensional parameters. The first, $\lambda = a/r_{2w}$, defines the relative position of the circular pin, where a is the distance from the gate rotor local coordinate origin to the centre of the pin in S_2, and r_{2w} denotes the pitch circle radius of the outer rotor.

The second parameter, $\sigma = \rho/r_{2w}$, represents the ratio of the pin radius ρ to the gate rotor's pitch circle radius. Since certain values of σ can lead to undercuts in the resulting rotor profile, Read [4] introduced a modified, normalised parameter $\bar{\sigma} \in [0, 1]$, where the upper limit corresponds to the maximum allowable pin size $\sigma_{\max} = \sigma_{\lim}$. This reformulation allows $\bar{\sigma}$ to be interpreted as a percentage of the limiting value, ensuring that valid and manufacturable rotor profiles are generated

for any choice of $\bar{\sigma}$ within the unit interval and $\sigma = \bar{\sigma}\sigma_{\text{lim}}$.

When generating rotor profiles using the pin-generation method, in addition to specifying the non-dimensional shape parameters λ and $\bar{\sigma}$, it is also necessary to define the number of lobes on either the main (inner) or gate (outer) rotor, typically number of lobes on the main rotor N_1, as number of lobes on the gate rotor $N_2 = N_1 + 1$ in considered internally geared screw machine configurations. Furthermore, one of the key geometric dimensions, either the axis distance E or the maximum outer rotor diameter D_2, must be selected, since they are directly related through the geometric constraint given in Equation (2.12).

$$\frac{E}{D_2} = \frac{1}{2N_2\left(\lambda - \sigma + \frac{2}{N_2}\right)} \tag{2.12}$$

These relationships define the geometric scaling required to ensure proper rotor meshing and profile construction within the internally geared screw machine framework. The geometric foundation and construction principles of the pin-generation method using circular pins are illustrated in Figure 2.6. Figure 2.7 shows examples of rotor profile shapes for $N_1 = 5$ and $N_2 = 6$, where N_1 and N_2 denote the number of lobes on the main (inner) and gate (outer) rotors, respectively. The influence of varying the parameters λ and $\bar{\sigma}$ on the resulting rotor geometries is also demonstrated.

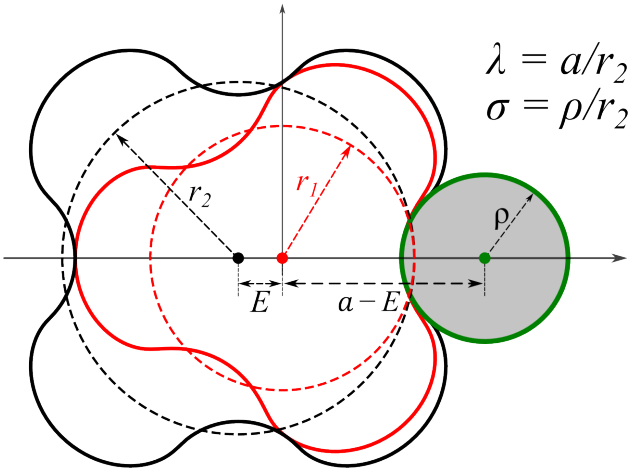

Figure 2.6: Geometric construction and coordinate system used in the pin-generation method for internally geared screw machines. The diagram illustrates the positioning of the circular pin, the pitch circles of the inner and outer rotors, and key geometric parameters such as a, r_2, and ρ.

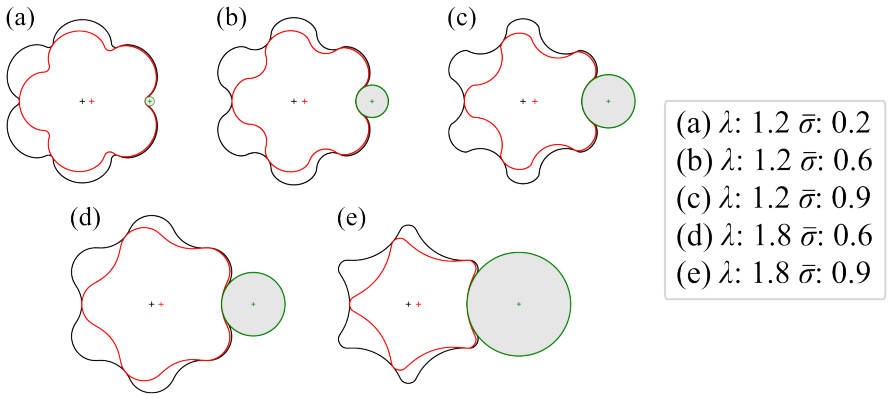

Figure 2.7: Examples of rotor profile shapes for $N_1 = 5$ and $N_2 = 6$, showing the effect of varying the non-dimensional parameters λ and $\bar{\sigma}$. These parameters influence the shape and size of the working chambers, as well as the sealing characteristics of the rotor pair.

2.4 Review of Geometry and Performance Prediction Models

Building up on the helical rotor description [39, 44], the geometry of conventional twin screw machines is well-established and has been examined extensively, providing a firm basis for working chamber formulation, volume variation, leakage paths, and end port geometry [2, 44–47]. In the chamber based approach, all phase dependent geometric quantities are expressed with respect to the main rotor rotational angle φ_1, which include the instantaneous chamber volume $V(\varphi_1)$, the inlet (low pressure) and outlet (high pressure) port flow areas $A_{\text{in}}(\varphi_1)$ and $A_{\text{out}}(\varphi_1)$, and the effective leakage path lengths or areas for interlobe, radial tip, and axial end face leakages. Parametrising the geometry by φ_1 provides a convenient time base through $\varphi_1(t) = \omega_1 t$, which enables direct tracking of mass flow, pressure, and temperature evolution with the main rotor rotational speed ω_1. The helical form is specified by the lead, the helix angle, and the wrap angle, which determine the axial progression of chambers and the phasing of port exposure along the length, and therefore the shapes of $V(\varphi_1)$ and $A_{\text{in/out}}(\varphi_1)$ that underpin process modelling and performance calculation [2, 44, 45].

Internally geared screw machine geometry is closely related to gerotor and progressive cavity [48] pumps, for which a substantial literature establishes working chamber formulations, volume curves, and leakage characterisation [49–51]. For IGSM with circular pin generated profiles (Section 2.3.3), Read et al. [4] provide a complete working chamber formulation that includes swept volumes and pressure angles for straight and for helical rotor cases. Complementary IGSM papers give end

port construction for profiles based on a combination of epicycloid and hypocycloid curves (Section 2.3.2) and define the dominant leakage paths together with leakage path length measures used in geometry analysis [6, 40].

In the context of IGSM design, geometry typically adopts gerotor style profile generation, whether circular pin or cycloidal families, while retaining the screw machine viewpoint. All phase dependent geometric quantities, such as the instantaneous chamber volume $V(\varphi_1)$, the port flow areas $A_{\mathrm{lp/hp}}(\varphi_1)$, and the leakage path measures, are parametrised by the main rotor rotational angle. This enables direct time mapping via $\varphi_1(t) = \omega_1 t$ and seamless integration with performance prediction models.

Machine learning surrogates may also be incorporated where appropriate, particularly because the geometry model developed here is intended for use in parametric studies and optimisation, where a large number of design evaluations is required. In such settings, rapid estimation of geometry dependent quantities, including chamber volume curves, port flow area variations, or leakage related measures, can substantially reduce the computational cost of design exploration while retaining the underlying chamber based formulation. Prior engineering studies have shown that surrogate models based on Gaussian processes and deep neural networks can predict distribution type quantities from geometric and operating inputs with good accuracy and shape fidelity, while providing orders of magnitude reductions in evaluation time, which makes them well suited to this role [52–55].

While the geometric aspects of IGSMs are well explored, only a limited number of studies have applied simplified non-validated one dimensional performance prediction models [5, 40] or high-fidelity computational fluid dynamics [56] to evaluate the potential benefits of the internally geared configuration. To enable extensive parametric studies and optimisation, it is important to develop a robust and reliable geometry model of the IGSM based on prior studies and to prepare it for integration with commonly used detailed one-dimensional chamber models.

One such simulation tool for conventional twin screw machines, widely applied in the past and well established, is `SCORG`. It was developed at City, St George's, University of London, and includes an implementation of the one dimensional chamber model for performance prediction [9]. The fundamental formulation of this chamber model was described in detail by Hanjalic and Stosic [12] and is summarised in Appendix C.

While this chamber model has been extensively used and validated for conventional twin screw machines [15, 46, 57], its application to internally geared screw machines has not been thoroughly investigated. Although the fundamental modelling principles remain the same, the distinct geometric configuration of IGSMs requires additional analysis to ensure the reliability and accuracy of chamber model predictions.

Apart from the described one-dimensional chamber model, high-order models based on Computational Fluid Dynamics (CFD) have also been applied to screw machines [9, 15, 58]. The chamber model offers a simplified but efficient means of simulating the pressure, temperature, and mass flow within the working chambers, incorporating empirical or analytical leakage correlations to estimate internal losses. In contrast, CFD provides a high-fidelity representation of the internal flow. These modelling tools are well established and have been extensively validated in the literature, forming the basis for design optimisation, performance evaluation, and operational diagnostics of conventional twin screw machines [59–61].

3 Objectives, Methodology and Expected Contributions

The reviewed literature indicates that internally geared screw machines are a relatively recent class of screw machine. Their rotor profiling draws on methods established for gerotor pumps, and their geometry has been studied extensively. However, a detailed geometry model that can be integrated with existing performance prediction tools and used for large scale parametric and optimisation studies remains absent. As a consequence, the potential benefits of the internally geared configuration relative to conventional twin screw machines have not been explored in depth. This gap is important because internally geared screw machines may extend the lower size bound of conventional designs. Addressing it requires a robust and reliable geometry model together with integration into a performance prediction framework. In addition, continuous contact has not previously been addressed in rotor profiling using either the rack method or deep generative neural networks. To extend the available design space, a rack based formulation for internally geared profiles and a data driven generative approach will be examined.

Overall, the work is organised around three objectives:

1. Numerical modelling of internally geared screw machines
2. Performance simulation and evaluation of the internally geared screw machine
3. Advancement of rotor profiling methods for internally geared screw machines

3.1 Numerical Modelling of Internally Geared Screw Machine Geometry

Objective: Develop a detailed geometry model based on circular pin-generated rotor profiles that supports contact point identification, working chamber formation and area calculation, volume integration for helical rotors, leakage area estimation, and end port formation with port flow areas. Include fast approximate estimators to enable rapid calculations.

Methodology

- C++17 object oriented modular implementation for the geometry core.
- Working chamber construction with polygon operations using the `Clipper2` C++ library (v1.5.4), area by the shoelace formula, and volume by cumulative trapezoidal integration with cumulative sums.

- Helical definition through lead, helix angle, and wrap angle, with linear interpolation to generate the main rotor rotational grid.
- Radial and axial leakage paths with phase dependent areas and lengths.
- Surrogate and acceleration strategies using machine learning and computational approximations, with parallel execution through multi-thread programming.

3.2 Performance Simulation and Evaluation of the Internally Geared Screw Machine

Objective: Integrate the geometry model with an existing one-dimensional chamber model, validate against available computational fluid dynamics data for IGSM in the absence of experimental measurements, and evaluate performance through parametric studies for air compression. Compare IGSM with a representative conventional twin screw machine at small scale.

Methodology

- C# coupling of the geometry module with the existing chamber model.
- Batch simulations in Python with orchestration scripts for parameter explorations and data handling.
- Use of a one-dimensional multi-chamber model to predict performance for both IGSM and conventional twin screw configurations.
- Validation by comparison with published CFD results for IGSM in oil-free and oil-injected cases.
- Parametric studies with automated post processing, Pearson correlation metrics [62], and comparison of key indicators such as volumetric efficiency, adiabatic efficiency, specific power, and volumetric flow.

3.3 Advancement of Rotor Profiling Methods for Internally Geared Screw Machines

Objective Establish conditions for continuous contact and investigate advanced profiling methods for internally geared screw machine. Adapt and assess the rack method for IGSM and explore data driven approaches based on deep neural networks.

Methodology

- Analytical development using transformation matrices with cycloidal and trochoidal constructions, including contact and curvature checks.
- Rack method formulation specific to internally geared kinematics with enforced continuous contact and a zero-minimum working chamber area.
- Data driven modelling with deep neural networks for surrogate profiling, including generative models to broaden the design space.
- Implementation and testing in Python 3.11.8 using `venv` for package management, with `PyTorch` 2.7.1 for model training and inference, and `matplotlib` 3.10.3 for plotting and diagnostics.

3.4 Computing Environment

All numerical studies will be executed on a laptop with an *AMD Ryzen 7 5800H* CPU, an *NVIDIA RTX 3060* GPU, *16 GB* RAM, and *NVMe* solid state storage. The geometry and profiling prototypes will use *MATLAB 2023b* and *Python* with `NumPy`, `SciPy`, and `PyTorch` for machine learning based surrogates. The production geometry engine will use C`++17` with `Eigen` library for linear algebra, polygon operations with the `Clipper2` library for chamber boundaries, area evaluation by the shoelace formula, and volume evaluation by cumulative trapezoidal integration with cumulative sums. Parallel execution will be used through multi-thread programming. The chamber model coupling will use *C#*. Batch studies will be orchestrated in *Python* with `pandas` for data management. Linear interpolation will be used to construct the main rotor angular grid. Reproducibility will be supported by version control and fixed random seeds in machine learning experiments.

3.5 Expected Contributions

- The development of a generalised geometry modelling framework for internally geared screw machines capable of rapidly and accurately computing phase dependent geometric quantities, including contact point locations, working chamber formation, helical chamber volumes, leakage flow areas, and end port flow areas, thereby extending the available modelling capability for this machine type.

- The introduction of computational acceleration strategies, including approximate methods and surrogate modelling pathways, to enable practical exploration of large IGSM design spaces that would otherwise be expensive using only high-fidelity deterministic calculations.

- Integration of the geometry model with a one-dimensional chamber framework, which enables efficient prediction of volumetric and adiabatic efficiency, specific power, and internal pressure evolution.

- The validation of the integrated modelling framework against higher-fidelity CFD results for representative internally geared cases, providing confidence in its predictive capability and establishing a basis for comparative parametric assessment against a conventional twin screw machine at small scale.

- The extension of the rack generation method to internally geared screw machine configurations under the constraints of continuous rotor contact and zero minimum working chamber area, together with the development of a complementary data-driven rotor profiling methodology based on generative deep neural networks.

4 Numerical Modelling of Internally Geared Screw Machine Geometry

Since internally geared screw machines represent a relatively novel class of screw compressors, the development of robust and reliable numerical models is essential for accurate optimisation and meaningful comparative analysis of their designs. Earlier research has primarily focused on the geometric characterisation of internally geared screw machines [3–5, 19]. Building up on these studies, the present work implements a detailed geometry model of an internally geared screw machine to enable efficient evaluation of working chamber volume progression, leakage paths, and port flow areas, as described in Section 4.1.

As the majority of currently implemented rotor profiles are generated using circular pins through the pin-generation method described by Vecchiato *et al.* [28] and further developed for internally geared screw machines by Read *et al.* [4], the geometry model implemented in this study relies on such profiles. This approach benefits from the availability of analytical solutions to the meshing condition, which simplifies and accelerates the modelling process.

The implemented geometry model provides a comprehensive framework for the geometric analysis of internally geared screw machines and has been integrated with an existing one-dimensional multi-chamber model previously developed at City St George's, University of London for conventional twin screw compressors [9]. This integration enables direct comparative and performance analyses between the two machine types. To further improve computational efficiency, the evaluation of port flow areas has been identified as the main bottleneck of the geometric model. Consequently, this component has been replaced with a surrogate machine learning model, as detailed in Section 4.2.

4.1 Geometry Model

In the developed geometry model, the pin-generation method introduced in Section 2.3.3 is implemented for the rotor profile generation of the internally geared screw machine. This method ensures that the generated rotor profiles satisfy both the continuous contact condition and the zero-minimum working chamber area requirement. Once the rotor profiles are defined, the complete machine geometry can be determined. The pin-generation approach requires the selection of non-dimensional rotor shape parameters $\lambda > 1$ and $\bar{\sigma} \in (0, 1)$ together with either the axis distance E or the outer rotor diameter D_2, which fully constrains the rotor pair in two dimensions.

To evaluate the machine geometry in three dimensions, it is first necessary to define the rotor length $L = L_1 = L_2$. Additionally, since the rotors are helical, the wrap angle Φ must also be specified. The wrap angle can be defined for one of the rotors, typically the main rotor, and calculated for the other using the gearing ratio. The relationship is given in Equation 4.1, where Φ_1 and Φ_2 are the wrap angles of the main and gate rotors, respectively, and $m_{21} = N_2/N_1$ is the gearing ratio based on rotor's corresponding lobe counts.

$$\Phi = \Phi_1 = m_{21}\Phi_2 \tag{4.1}$$

4.1.1 Rotor Profile Generation

Using the circular pin generation method, rotor shapes are derived from points on a circular pin. The pin is parametrised by the profile parameter $\theta \in [0, 2\pi]$ and expressed in the gate rotor local coordinate system S_2 with coordinates $\left(x_c^{S_2}(\theta),\, y_c^{S_2}(\theta)\right)$ as in Equation (4.2). The circular pin in S_2 is defined by the non-dimensional pair $(\lambda, \bar{\sigma})$, which set the centre offset a and pin radius ρ (both in S_2) as

$$a \;=\; \lambda\, r_{2w}, \qquad \rho \;=\; \bar{\sigma}\, \sigma_{\lim},$$

where r_{2w} denotes the gate rotor pitch circle radius, $\sigma_{\lim}$ is the maximum admissible pin radius ensuring generation without undercuts (as detailed by Read et al. [4]), and $\bar{\sigma} \in (0, 1]$.

$$\mathbf{c}_p^{S_2}(\theta) = \begin{bmatrix} x_c^{S_2}(\theta) & y_c^{S_2}(\theta) & 0 & 1 \end{bmatrix}^\top = \begin{bmatrix} a - \rho\cos\theta & \rho\sin\theta & 0 & 1 \end{bmatrix}^\top \tag{4.2}$$

Since the profile parameter $\theta \in [0, 2\pi]$ advances by one full revolution over a complete rotation of the gate rotor, the meshing solution expressed as the gate rotor rotational angle satisfies $\sigma_2^*(\theta) = \theta$. This angle is the rotation required, starting from the initial position, for the circular pin to rotate in gate rotor local coordinate system so that the specified point on the circle comes into conjugate contact with the main rotor.

For any prescribed rotation $\sigma_2^*(\theta)$, the corresponding meshing point on the circle is obtained by solving the meshing condition in Equation (A.5) in the gate rotor local coordinate system with the known gate rotor rotational angle $\sigma_2^*(\theta)$, which yields the meshing point on a circular pin expressed through the profile parameter $\theta_m\Big(\sigma_2^*(\theta)\Big) = \theta_m(\theta)$ as given in Equation (4.3) [28].

$$\theta_m(\theta) \;=\; \arctan\left(\frac{\sin\Big(\sigma_2^*(\theta)\Big)}{\lambda - \cos\Big(\sigma_2^*(\theta)\Big)}\right), \tag{4.3}$$

Substituting $\theta = \theta_m$ into Equation (4.2) gives the contact point coordinates on the circular pin in S_2 as defined in Equation (4.4).

$$\mathbf{c}_p^{S_2}(\theta_m) = \begin{bmatrix} x_c^{S_2}(\theta_m) & y_c^{S_2}(\theta_m) & 0 & 1 \end{bmatrix}^\top = \begin{bmatrix} a - \rho\cos\theta_m & \rho\sin\theta_m & 0 & 1 \end{bmatrix}^\top \tag{4.4}$$

One full rotation of a single circular pin traces a single lobe on the main rotor profile. The corresponding main rotor points for that lobe in the local coordinate system S_1 are obtained by the rigid transformation that maps points from S_2 to S_1. Using the transformation matrix defined in Equation (B.6) and its inverse $\Big(\mathbf{M}_{12}^{(I)}(\varphi_1)\Big)^{-1} = \mathbf{M}_{21}^{(I)}(\varphi_1)$, the circular pin contact points $\mathbf{c}_p^{S_2}(\theta_m)$ are mapped into S_1 as shown in Equation (4.5). The single lobe coordinates of the main rotor generated by the pin generation method, expressed in terms of the profile parameter θ, can be obtained directly from Equation (4.5), where $\sigma_1^*(\theta) = m_{21}\sigma_2^*(\theta)$ and m_{21} is the gearing ratio.

$$\mathbf{c}_p^{S_1}(\theta) = \begin{bmatrix} x_1^{S_1}(\theta) & y_1^{S_1}(\theta) & 0 & 1 \end{bmatrix}^\top = \mathbf{M}_{21}^{(I)}\Big(\sigma_1^*(\theta)\Big)\,\mathbf{c}_p^{S_2}\Big(\theta_m(\theta)\Big) \tag{4.5}$$

The corresponding gate rotor single lobe coordinates are obtained by enforcing conjugate meshing with the generated main rotor. For each profile parameter θ, the meshing angle between the circular pin and the main rotor is $\sigma_2^*(\theta)$, and the gate rotor rotational angle that satisfies the meshing condition is given by the analytic quantity $\sigma_2(\theta)$, expressed as a piecewise function of profile parameter θ (detailed by Vecchiato et al. [28]). This $\sigma_2(\theta)$ is evaluated using Equation (4.6).

$$\sigma_2(\theta) \;=\; \begin{cases} {\sigma_2}^*(\theta), & \theta \le \arccos(1/\lambda), \\ \dfrac{\pi - 2\Big[{\sigma_2}^*(\theta) + \theta_m\Big(\sigma_2^*(\theta)\Big)\Big]}{m_{21}} + {\sigma_2}^*(\theta), & \arccos(1/\lambda) < \theta < 2\pi - \arccos(1/\lambda), \\ {\sigma_2}^*(\theta) - \dfrac{N_1}{N_2}\,2\pi, & \theta \ge 2\pi - \arccos(1/\lambda). \end{cases} \tag{4.6}$$

Once $\sigma_2(\theta)$ is defined, solution to the meshing condition can be obtained with respect to the main rotors local coordinate system as $\sigma_1(\theta) = m_{21}\sigma_2(\theta)$. The points of the gate rotor single lobe, defined in its local coordinate system S_2 and corresponding to the same contact points $c_p^{S_1}(\theta)$ on the main rotor, can be obtained directly by applying the rigid transformation, using transformation matrix defined in Equation (B.6), that maps the contact points on the main rotor single lobe from its local coordinate system S_1 into S_2, as defined in Equation (4.7).

$$\begin{bmatrix} x_2^{S_2}(\theta) & y_2^{S_2}(\theta) & 0 & 1 \end{bmatrix}^\top = \mathbf{M}_{12}^{(I)}\Big(\sigma_1(\theta)\Big)\, \mathbf{c}_p^{S_1}(\theta), \tag{4.7}$$

Contact point on the main rotor $\mathbf{c}_p^{S_1}(\theta)$ can be defined in the global coordinate system S_f as two separate paths:

1. the main contact loci corresponding to the main solution of the meshing condition $\sigma_1^*(\theta)$,
2. the fillet contact loci corresponding to the fillet solution of the meshing condition $\sigma_1(\theta)$.

Main contact loci can be obtained by rigid transformation of contact points on the main rotor in its local coordinate system to global coordinate system S_f using transformation matrix defined in Equation (B.3) and main solution to the meshing condition, $\sigma_1^*(\theta) = m_{21}\sigma_2^*(\theta)$, as defined in Equation (4.8).

$$\begin{bmatrix} x_{c_m}^{S_f}(\theta) & y_{c_m}^{S_f}(\theta) & 0 & 1 \end{bmatrix}^\top = \mathbf{M}_{1f}^{(I)}\Big(\sigma_1^*(\theta)\Big) \begin{bmatrix} x_1^{S_1}(\theta) & y_1^{S_1}(\theta) & 0 & 1 \end{bmatrix}^\top \tag{4.8}$$

Fillet contact loci can be obtained by rigid transformation of contact points on the main rotor in its local coordinate system to global coordinate system S_f using transformation matrix defined in Equation (B.3) and fillet solution to the meshing condition, $\sigma_1(\theta) = m_{21}\sigma_2(\theta)$, as defined in Equation (4.9).

$$\begin{bmatrix} x_{c_f}^{S_f}(\theta) & y_{c_f}^{S_f}(\theta) & 0 & 1 \end{bmatrix}^\top = \mathbf{M}_{1f}^{(I)}\Big(\sigma_2(\theta)\Big) \begin{bmatrix} x_1^{S_1}(\theta) & y_1^{S_1}(\theta) & 0 & 1 \end{bmatrix}^\top \tag{4.9}$$

The single lobe profiles of the main and gate rotors can be expressed in polar form (using Equations (4.10) and (4.11)) in their local coordinate systems with polar coordinates

$$\left(\rho_{p,i}^{S_i}(\theta),\, \varphi_{p,i}^{S_i}(\theta)\right), \qquad i \in \{1, 2\}.$$

$$\rho_{p,i}^{S_i}(\theta) = \sqrt{\left(x_i^{S_i}(\theta)\right)^2 + \left(y_i^{S_i}(\theta)\right)^2} \tag{4.10}$$

$$\varphi_{p,i}^{S_i}(\theta) = \arctan\left(\frac{y_i^{S_i}(\theta)}{x_i^{S_i}(\theta)}\right) \tag{4.11}$$

The complete rotor profile is obtained by periodic extension of the single lobe polar coordinates over N_i periods for each rotor, where $\left(\rho_{p,i}^{S_i}(\theta),\, \varphi_{p,i}^{S_i}(\theta)\right)$ represents one period. The pin circle has fundamental period 2π, while in the rotor polar coordinates the fundamental period is $2\pi/N_i$. Hence the complete rotor profile polar coordinates in the corresponding local polar coordinate system can be obtained from Equations (4.12).

$$\begin{aligned} \hat{\theta} &= \theta + 2\pi j_i, \\ \rho_{p,i}^{S_i}(\hat{\theta}) &= \rho_{p,i}^{S_i}(\theta), \\ \varphi_{p,i}^{S_i}(\hat{\theta}) &= \varphi_{p,i}^{S_i}(\theta) + j_i \frac{2\pi}{N_i}, \end{aligned} \qquad \begin{aligned} &\theta \in [0, 2\pi), \quad i \in \{1, 2\}, \\ &j_i = 0, 1, \ldots, N_i - 1. \end{aligned} \tag{4.12}$$

Cartesian coordinates of the complete rotor profiles in their local coordinate systems are derived from the corresponding polar coordinates and given in Equations (4.13) and (4.14).

$$x_i^{S_i}(\hat{\theta}) = \rho_{p,i}^{S_i}(\hat{\theta}) \cos\left(\varphi_{p,i}^{S_i}(\hat{\theta})\right), \tag{4.13}$$

$$y_i^{S_i}(\hat{\theta}) = \rho_{p,i}^{S_i}(\hat{\theta}) \sin\left(\varphi_{p,i}^{S_i}(\hat{\theta})\right). \tag{4.14}$$

Contact points on the main and fillet contact loci over the complete profile are obtained as in Equations (4.15) and (4.16), which expresses the complete contact loci as the periodic extension of the single lobe parametrisation.

$$\big(x_{c_m}^{S_f}(\hat{\theta}),\, y_{c_m}^{S_f}(\hat{\theta})\big) = \big(x_{c_m}^{S_f}(\theta),\, y_{c_m}^{S_f}(\theta)\big), \tag{4.15}$$

$$\big(x_{c_f}^{S_f}(\hat{\theta}),\, y_{c_f}^{S_f}(\hat{\theta})\big) = \big(x_{c_f}^{S_f}(\theta),\, y_{c_f}^{S_f}(\theta)\big), \tag{4.16}$$

Analogously, the meshing angles are extended for full profile by corresponding periodic shift as defined in Equations (4.17) and (4.18).

$$\sigma_1(\hat{\theta}) = m_{21}\sigma_2(\hat{\theta}) = m_{21}\big(\sigma_2(\theta) + 2\pi j_2\big), \tag{4.17}$$

$$\sigma_1^*(\hat{\theta}) = m_{21}\sigma_2^*(\hat{\theta}) = m_{21}\big(\sigma_2^*(\theta) + j_2\tfrac{2\pi}{N_2}\big) \tag{4.18}$$

4.1.2 Working Chamber Formulation and Progression

To calculate the area of a single working chamber from its initial formation to the point where it disappears, the leading and trailing contact points are used to define its boundaries. At any given rotor position, the chamber is enclosed between these two contact points and the corresponding segments of the main and gate rotor profiles.

The rotor profile coordinates are obtained from the meshing condition (as described in Section 4.1.1), which maps each rotational position of the rotor to the corresponding contact point on the profile, parametrised by the profile parameter $\hat{\theta}$. For the complete main and gate rotor profiles

$$\Big(x_i^{S_i}(\hat{\theta}),\, y_i^{S_i}(\hat{\theta})\Big), \qquad i \in \{1, 2\}$$

as introduced in Equations (4.13) and (4.14), the meshing condition yields two solutions:

$$\sigma_i(\hat{\theta}) = m_{21}\,\sigma_2(\hat{\theta}) \quad \text{and} \quad \sigma_1^*(\hat{\theta}) = m_{21}\sigma_2^*(\hat{\theta}).$$

Both $\sigma_i(\hat{\theta})$ and $\sigma_i^*(\hat{\theta})$ denote the rotation angle of rotor $i \in \{1, 2\}$ required for the point with local coordinates $\big(x_i^{S_i}(\hat{\theta}),\, y_i^{S_i}(\hat{\theta})\big)$, defined by the profile parameter, to come into contact with the meshing rotor. Each period of $\sigma_i(\hat{\theta})$ and $\sigma_i^*(\hat{\theta})$ corresponds to one complete revolution of the rotor through which all contact locations on a single lobe are traced.

To follow a selected working chamber through a complete revolution, the trailing and leading contact points must be identified over the entire cycle. For a single working chamber, the bounding trailing and leading contacts occur on two adjacent single lobes. The full set of contact points encountered during one revolution is therefore the union of paths $\sigma_i(\hat{\theta})$ and $\sigma_i^*(\hat{\theta})$ over

$$\hat{\theta} \in \big(\arccos(1/\lambda),\, 4\pi - \arccos(1/\lambda)\big), \qquad i \in \{1, 2\},$$

which spans the two consecutive lobe periods needed to capture both bounding contacts.

Given that the area is evaluated at each rotational position, it is essential to express trailing and leading contact paths in terms of the rotational angle. However, since $\sigma_i(\hat{\theta})$ is not injective function on $[0, 2\pi)$, a common grid must be enforced by defining piecewise inverse functions on monotone segments, implemented via linear interpolation after a constant phase alignment, as defined in Equation (4.19). This phase alignment sets the starting instant of the observed working chamber to zero.

$$\sigma_i^{(0)} = \frac{N_2}{N_i}\arccos(1/\lambda), \qquad \tilde{\sigma}_i(\hat{\theta}) = \sigma_i(\hat{\theta}) - \Big(\frac{2\pi}{N_i} - \sigma_i^{(0)}\Big), \qquad \tilde{\sigma}_i^*(\hat{\theta}) = \sigma_i^*(\hat{\theta}) - \Big(\frac{2\pi}{N_i} - \sigma_i^{(0)}\Big). \tag{4.19}$$

With this alignment, a uniform gate rotor rotational angle grid can be defined, as shown in Equation (4.20), and the corresponding main rotor grid can be obtained from the gearing ratio, defined in Equation (4.21), where K is the resolution of the grid which controls the fidelity of all subsequent geometry calculations and $\varphi_{wc} = \sigma_1\big(4\pi - \arccos(1/\lambda)\big)$ is the end position of the working chamber.

$$\{\varphi_{2,k}\}_{k=0}^{K-1} \subset [0, \varphi_{wc}) \tag{4.20}$$

$$\varphi_{1,k} = m_{21}\,\varphi_{2,k} \tag{4.21}$$

The leading and trailing rotor single lobe intervals with respect to the complete profile parameter $\hat{\theta}$ are $(0, 2\pi]$ and $(2\pi, 4\pi]$, respectively. On these two intervals, the corresponding contact path boundaries are defined as:

$$\mathcal{S}_{i,1} = \Big\{\sigma_i(\hat{\theta}) : \hat{\theta} \in (0, 2\pi]\Big\}, \quad \mathcal{S}_{i,1}^* = \Big\{\sigma_i^*(\hat{\theta}) : \hat{\theta} \in (0, 2\pi]\Big\},$$
$$\mathcal{S}_{i,2} = \Big\{\sigma_i(\hat{\theta}) : \hat{\theta} \in (2\pi, 4\pi]\Big\}, \quad \mathcal{S}_{i,2}^* = \Big\{\sigma_i^*(\hat{\theta}) : \hat{\theta} \in (2\pi, 4\pi]\Big\}.$$

The transition between the two meshing regimes is set by the transition point $\theta^{(t)} = \arccos(1/\lambda)$. With this transition point, the following subintervals are introduced:

$$I_1 = (\theta^{(t)},\, 2\pi - \theta^{(t)}), \qquad J_1 = (2\pi - \theta^{(t)},\, 2\pi], \qquad J_2 = (2\pi,\, 4\pi - \theta^{(t)}), \qquad I_2 = (2\pi + \theta^{(t)},\, 4\pi - \theta^{(t)}).$$

The leading and trailing contact paths can then be defined for rotor $i \in \{1, 2\}$ as presented in in Equations (4.22) and (4.23), respectively.

$$\Gamma_{\mathrm{t},i} = \underbrace{\left\{\sigma_i(\hat{\theta}) : \hat{\theta} \in I_1\right\}}_{\text{fillet loci}} \cup \underbrace{\left\{\sigma_i^*(\hat{\theta}) : \hat{\theta} \in I_1\right\}}_{\text{main loci}} \cup \underbrace{\left\{\sigma_i^*(\hat{\theta}) : \hat{\theta} \in J_1\right\}}_{\text{main loci}} \tag{4.22}$$

$$\Gamma_{\ell,i} = \underbrace{\left\{\sigma_i(\hat{\theta}) : \hat{\theta} \in J_1\right\}}_{\text{fillet loci}} \cup \underbrace{\left\{\sigma_i^*(\hat{\theta}) : \hat{\theta} \in J_2\right\}}_{\text{main loci}} \cup \underbrace{\left\{\sigma_i(\hat{\theta}) : \hat{\theta} \in I_2\right\}}_{\text{fillet loci}} \tag{4.23}$$

The mappings that return the set of profile parameters at each sampled rotor rotational angle obtained from $\varphi_{i,k}$ grid are defined in Equations (4.24) and (4.25) for the leading and trailing contacts, respectively.

$$\Theta_{\ell,i}(\varphi_{i,k}) = \left\{\hat{\theta} \in I_1 : \tilde{\sigma}_i(\hat{\theta}) = \varphi_{i,k}\right\} \cup \left\{\hat{\theta} \in J_1 : \tilde{\sigma}_i^*(\hat{\theta}) = \varphi_{i,k}\right\} \cup \left\{\hat{\theta} \in J_2 : \tilde{\sigma}_i^*(\hat{\theta}) = \varphi_{i,k}\right\} \tag{4.24}$$

$$\Theta_{t,i}(\varphi_{i,k}) = \left\{\hat{\theta} \in J_1 : \tilde{\sigma}_i(\hat{\theta}) = \varphi_{i,k}\right\} \cup \left\{\hat{\theta} \in J_2 : \tilde{\sigma}_i^*(\hat{\theta}) = \varphi_{i,k}\right\} \cup \left\{\hat{\theta} \in I_2 : \tilde{\sigma}_i(\hat{\theta}) = \varphi_{i,k}\right\} \tag{4.25}$$

Each set $\Theta_{\ell,i}(\varphi_{i,k})$ and $\Theta_{t,i}(\varphi_{i,k})$ may contain one or more values of $\hat{\theta}$ for a given grid angle $\varphi_{i,k}$, reflecting the non-injective structure $\sigma_i(\hat{\theta})$.

For any sampled angle $\varphi_{i,k}$, the leading and trailing contact points that bound the observed working chamber on rotor $i \in \{1, 2\}$ are obtained by evaluating the rotor coordinates at the corresponding contact path sets:

$$\left\{\, \left(x_i(\hat{\theta}),\, y_i(\hat{\theta})\right) \;:\; \hat{\theta} \in \Theta_{\ell,i}(\varphi_{i,k}) \,\right\}, \qquad \left\{\, \left(x_i(\hat{\theta}),\, y_i(\hat{\theta})\right) \;:\; \hat{\theta} \in \Theta_{\mathrm{t},i}(\varphi_{i,k}) \,\right\}, \quad k = 0, \ldots, K-1.$$

In the global coordinate system, the same contact points on the main and fillet contact loci are

$$\left\{\, \left(x_{c_m}(\hat{\theta}),\, y_{c_m}(\hat{\theta})\right) \;:\; \hat{\theta} \in \Theta_{\ell,i}(\varphi_{i,k}) \,\right\}, \qquad \left\{\, \left(x_{c_m}(\hat{\theta}),\, y_{c_m}(\hat{\theta})\right) \;:\; \hat{\theta} \in \Theta_{t,i}(\varphi_{i,k}) \,\right\}, \quad k = 0, \ldots, K-1.$$

An example of the relationship between the distributed main rotor rotational angle $\varphi_{1,k}$ and the defined leading and trailing contact paths is shown in Figure 4.1. At the reference position $\varphi_{1,0} = 0$, the leading and trailing contact points coincide and the chamber area is zero. As $\varphi_{1,k}$ increases, the chamber forms, grows, and subsequently vanishes when the two points meet again.

This procedure enables the identification of the working chamber boundaries at every rotor position and underpins the accurate geometric calculation of the internally geared screw machine throughout the operating cycle.

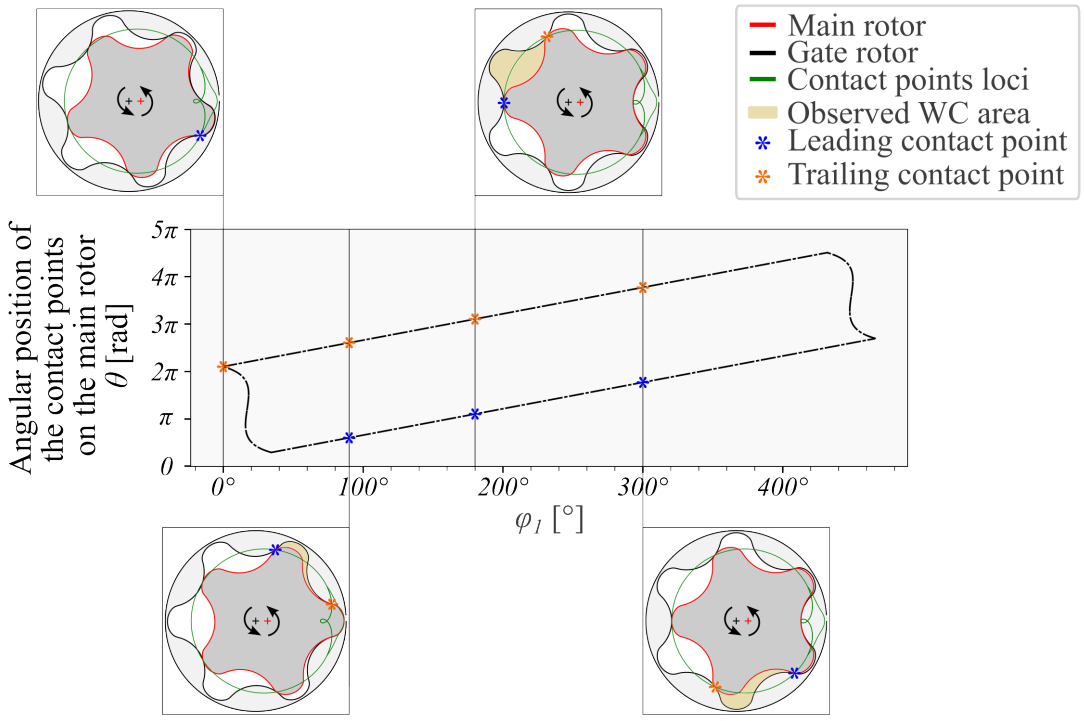

Figure 4.1: Tracking of the leading and trailing contact points for a single working chamber over one rotation cycle of the main rotor. The tracked working chamber is illustrated for four selected angles, showing the chamber formation, growth, and closure.

To compute the working chamber area at a given rotor rotational angle $\varphi_{i,k}$, all profile arcs bounded by leading and trailing contact points are considered, drawn from $\Theta_{\ell,i}(\varphi_{i,k})$ and $\Theta_{t,i}(\varphi_{i,k})$, respectively. For each contact pair at $\varphi_{i,k}$, the complete profile parameters of the leading and trailing contact points are

$$\hat{\theta}_{\ell,i}^{(m)} \in \Theta_{\ell,i}(\varphi_{i,k}), \qquad \hat{\theta}_{t,i}^{(m)} \in \Theta_{t,i}(\varphi_{i,k}), \qquad m = 1, \ldots, M(k),$$

where $M(k)$ denotes the number of active trailing–leading contact pairs at the sampled index k.

The corresponding endpoint polar data for leading and trailing contact points in the rotor local coordinate system S_i are defined in Equations (4.26) and (4.27), where $\big(\rho_{p,i}(\hat{\theta}),\, \varphi_{p,i}(\hat{\theta})\big)$, $i \in \{1, 2\}$, denote the complete main and gate rotor polar coordinates as given in Equation (4.12). The polar angle $\varphi_{p,i}$ is unwrapped along each arc from trailing to leading so that continuity is preserved.

$$\rho_{\ell,i}^{(m)} \equiv \rho_{p,i}\big(\hat{\theta}_{\ell,i}^{(m)}\big), \qquad \rho_{t,i}^{(m)} \equiv \rho_{p,i}\big(\hat{\theta}_{t,i}^{(m)}\big), \tag{4.26}$$

$$\varphi_{\ell,i}^{(m)} \equiv \varphi_{p,i}\big(\hat{\theta}_{\ell,i}^{(m)}\big), \qquad \varphi_{t,i}^{(m)} \equiv \varphi_{p,i}\big(\hat{\theta}_{t,i}^{(m)}\big). \tag{4.27}$$

Using the rotor polar coordinates defined in Equation (4.12) and contact locations parametrised by the profile parameter $\hat{\theta}$, the area of the m-th profile arc at the rotor position $\varphi_{i,k}$ is defined in Equation (4.28).

$$\mathcal{C}_i^{(m)}(\varphi_{i,k}) = \frac{1}{2} \int_{\hat{\theta}_{\mathrm{t},i}^{(m)}}^{\hat{\theta}_{\ell,i}^{(m)}} \big(\rho_{p,i}(\hat{\theta})\big)^2 \, \frac{d\varphi_{p,i}}{d\hat{\theta}}(\hat{\theta})\, d\hat{\theta}. \tag{4.28}$$

Since the rotor origins do not coincide, a triangular correction is required in the profile arc area calculation. For the m-th arc at angle $\varphi_{i,k}$, the correction $\mathcal{T}_i^{(m)}(\varphi_{i,k})$ is evaluated from the polar end points specified in Equations (4.26) and (4.27), and is defined in Equation (4.29).

$$\mathcal{T}_i^{(m)}(\varphi_{i,k}) = \frac{1}{2}\, \rho_{\mathrm{t}}^{(m)}\, \rho_{\ell}^{(m)}\, \sin\big(\Delta\varphi_{p,i}^{(m)}(\varphi_{i,k})\big), \qquad \Delta\varphi_{p,i}^{(m)} = \varphi_{\ell}^{(m)} - \varphi_{\mathrm{t}}^{(m)}\ . \tag{4.29}$$

The triangular correction represents the area of the triangle whose vertices are the rotor origin and the two polar end points corresponding to the trailing and leading contact locations, all expressed in the rotor local coordinate system S_i.

The segment area associated with the m-th profile arc at rotor position $\varphi_{i,k}$, obtained by subtracting the triangular correction from the corresponding profile arc area, is given by Equation (4.30).

$$\mathcal{S}_i^{(m)}(\varphi_{i,k}) = \mathcal{C}_i^{(m)}(\varphi_{i,k}) - \mathcal{T}_i^{(m)}(\varphi_{i,k})\ . \tag{4.30}$$

With the outer boundary provided by the gate rotor and the inner boundary by the main rotor, the working chamber area at the main rotor rotational position $\varphi_{1,k}$ is defined as the signed sum of segment contributions, as given in Equation (4.31). Here, $M(k)$ is the number of active contact pairs for rotor $i \in \{1, 2\}$ at index k. Figure 4.2 illustrates the working chamber area calculation from segment areas, including the triangular correction.

$$\mathcal{A}_{\mathrm{wc}}(\varphi_{1,k}) = \sum_{m=1}^{M(k)} \left[\mathcal{C}_2^{(m)}(\varphi_{2,k}) - \mathcal{T}_2^{(m)}(\varphi_{2,k})\right] \; - \; \sum_{m=1}^{M(k)} \left[\mathcal{C}_1^{(m)}(\varphi_{1,k}) - \mathcal{T}_1^{(m)}(\varphi_{1,k})\right] \tag{4.31}$$

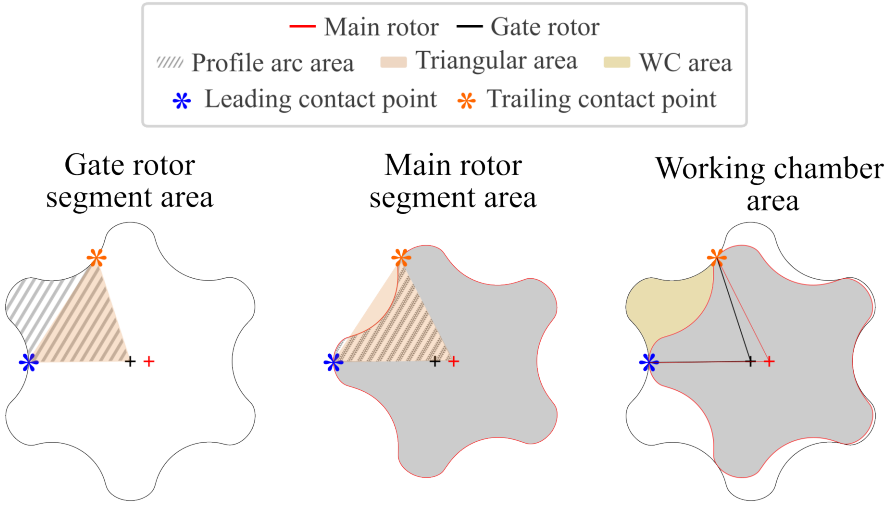

Figure 4.2: Working chamber area calculation using segment areas with triangular correction. For a given main rotor angle $\varphi_{1,k}$, the chamber boundary is partitioned into profile arc segments between the trailing and leading contact points and each segment area is computed from the profile arc area with a triangular correction.

4.1.3 Working Chamber Volume Calculation

To determine the volume of a working chamber at a given main rotor angle $\varphi_1^{(g)}$, the corresponding two-dimensional cross-sectional area must be integrated along the axial length of the rotor. This reflects how the chamber extends helically from the low-pressure to the high-pressure end face of the machine.

Let $A_{\mathrm{wc}}(\varphi_1, z)$ denote the analytical working chamber area at rotor angle φ_1 and axial position z. The total chamber volume can be obtained by integrating this area over the full rotor length L. However, due to the helical nature of the rotors, this three-dimensional integration can be reformulated in terms of the angular progression of the rotor using the wrap angle Φ_1, which defines the total angular span over which the chamber evolves. As described by Read et al [4], the resulting expression is given by:

$$V_{\mathrm{wc}}(\varphi_1^{(g)}) = \int_0^L A_{\mathrm{wc}}(\varphi_1, z)\, dz = \frac{L}{\Phi_1} \int_{\varphi_1^{(0)}}^{\varphi_1^{(g)}} \Big([A_{\mathrm{wc}}]_{\mathrm{lp}}(\varphi_1) - [A_{\mathrm{wc}}]_{\mathrm{hp}}(\varphi_1) \Big) d\varphi_1 \tag{4.32}$$

Here, $\varphi_1^{(0)}$ denotes the angular position where the chamber first begins to form, and $\varphi_1^{(g)}$ is the current rotor angle for which the volume is evaluated. The terms $[A_{\mathrm{wc}}]_{\mathrm{lp}}(\varphi_1)$ and $[A_{\mathrm{wc}}]_{\mathrm{hp}}(\varphi_1)$ represent the cross-sectional chamber areas at the low-pressure and high-pressure end faces, respectively. The scaling factor $\frac{L}{\Phi_1}$ maps the angular rotation into axial displacement, allowing the chamber volume to be computed based only on cross-sectional area data at each end face.

Given discrete samples $\Big\{ \big(\varphi_{1,k},\, \mathcal{A}_{\mathrm{wc}}(\varphi_{1,k})\big) \Big\}_{k=0}^{K-1}$ at the low-pressure end face from Equation (4.31), and the corresponding high-pressure samples shifted by wrap angle, $\Big\{ \big(\varphi_{1,k} + \Phi_1,\, \mathcal{A}_{\mathrm{wc}}(\varphi_{1,k})\big) \Big\}_{k=0}^{K-1}$, a common monotone angle grid $\{\varphi_{1,p}\}_{p=0}^{P-1}$ is formed as defined in Equation (4.33). Angles are unwrapped as required, and both datasets are linearly interpolated onto this grid to obtain

$$\mathcal{A}_{\mathrm{lp}}(\varphi_{1,p}) = [\mathcal{A}_{\mathrm{wc}}]_{\mathrm{lp}}(\varphi_{1,p}), \qquad \mathcal{A}_{\mathrm{hp}}(\varphi_{1,p}) = [\mathcal{A}_{\mathrm{wc}}]_{\mathrm{hp}}(\varphi_{1,p}).$$

$$\{\varphi_{1,p}\}_{p=0}^{P-1} \subset [\varphi_{1,0},\, \varphi_{1,K-1} + \Phi_1] \tag{4.33}$$

The volume of a single working chamber at each sampled rotational position of the main rotor is then computed by a discrete aggregated trapezoidal sum over the area difference as shown in Equation (4.34).

$$\begin{aligned} &\mathcal{V}(\varphi_{1,0}) = 0, \\ &\mathcal{V}(\varphi_{1,p}) = \mathcal{V}(\varphi_{1,p-1}) + \frac{L}{\Phi_1} \Big[\frac{\Delta\mathcal{A}(\varphi_{1,p}) + \Delta\mathcal{A}(\varphi_{1,p-1})}{2} \Big] \Delta\varphi_{1,p}, \\ &\Delta\varphi_{1,p} = \varphi_{1,p} - \varphi_{1,p-1}, \qquad \Delta\mathcal{A}(\varphi_{1,p}) = \mathcal{A}_{\mathrm{lp}}(\varphi_{1,p}) - \mathcal{A}_{\mathrm{hp}}(\varphi_{1,p}), \qquad p = 1, \ldots, P-1. \end{aligned} \tag{4.34}$$

This approach provides an efficient and accurate method to compute the evolving chamber volume as the rotors rotate, as required for performance modelling. An illustrative example of the volume integration procedure is shown in Figure 4.3.

Once the full chamber volume has been calculated over the entire chamber evolution cycle, the swept volume V_{sw}, defined as the theoretical volume displaced per revolution of the main rotor, can be obtained. It is calculated by the product of the number of main rotor lobes N_1 and the maximum volume of a single working chamber as defined in Equation (4.35).

$$V_{sw} = N_1 \left(\max_{\varphi_{1,p}} \mathcal{V}_{\mathrm{wc}}(\varphi_{1,p}) \right) \tag{4.35}$$

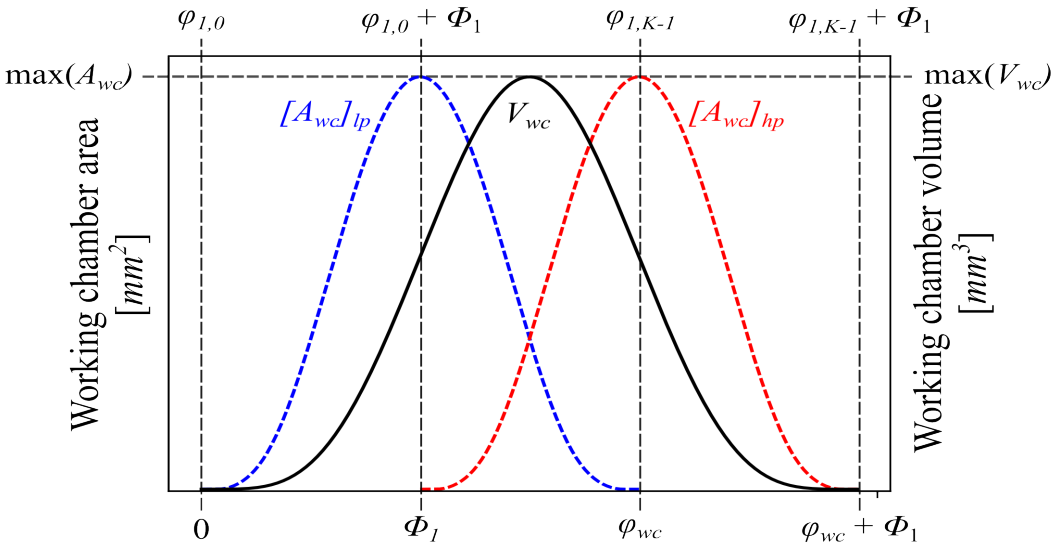

Figure 4.3: Evolution of the working chamber area and volume over the main rotor angle φ_1. The low-pressure and high-pressure side areas $[A_{wc}]_{lp}$ and $[A_{wc}]_{hp}$ are shown in blue and red, respectively, with the total working chamber volume illustrated in black.

4.1.4 Leakage Area Estimation

Due to the nature of the compression process in internally geared screw machine, the working chambers operate at varying pressure levels along the rotor length. As a result, leakage can occur through small internal clearances between moving and stationary components, allowing high-pressure gas to escape into lower-pressure regions. These leakages reduce the overall volumetric efficiency and performance of the machine.

Leakage paths in internally geared screw machines occur along specific sealing lines that connect neighbouring working chambers operating at different pressures. As illustrated in Figure 4.4, each working chamber is bounded by sections of the rotor profiles, with contact lines that may interface either with a chamber ahead (higher pressure) or behind (lower pressure) along the rotor axis. The sealing lines illustrated in Figure 4.4 represent the primary leakage paths in the IGSM configuration. These include the main leakage path: from the outer rotor tip to the main rotor tip (red), the inner path: from the outer rotor tip to the inner rotor root (blue), and the outer path: from the outer rotor root to the inner rotor tip (green). These leakage paths have previously been identified and defined in the IGSM literature. However, to the author's knowledge, a detailed leakage model that combines the established leakage treatment used in conventional twin screw machines with the specific leakage path definitions of internally geared screw machines has not yet been reported in the literature. For this reason, the present section sets out the leakage model in detail.

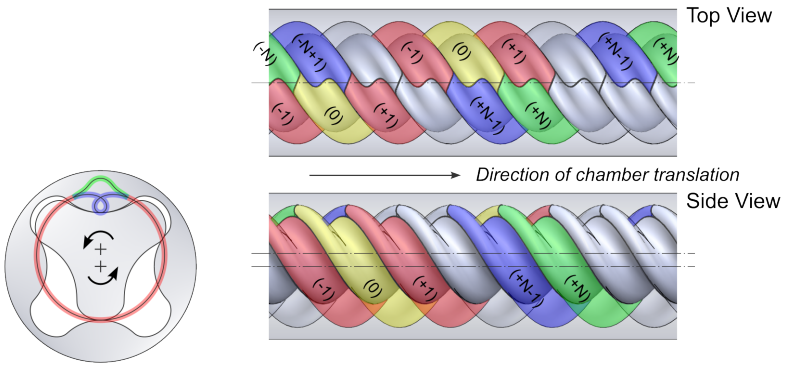

Figure 4.4: Illustration of leakage paths in an internally geared screw machine (third-angle projection). (a) rotor rotation and chamber positions; (b) top and side views of chamber indexing along the axial direction. Leakage may occur between adjacent chambers as they translate during operation.

To calculate the leakage areas for a given chamber at a specific rotor position, the relevant contact points are first identified in two dimensions. Analogously to the leading and trailing contact paths described in Section 4.1.2 and defined in Equations (4.24) and (4.25), the principal leakage paths are extracted by restricting the complete profile parameter $\hat{\theta}$ to suitable subintervals and by selecting contact points within each subinterval on either $\sigma_1(\hat{\theta})$ (fillet contact meshing) or $\sigma_1^*(\hat{\theta})$ (main contact meshing), defined in Equations (4.17) and (4.18). The three primary leakage paths: outer, main,

and inner are then given by Equations (4.36)–(4.38), where N_2 denotes the number of lobes of the gate rotor and $\theta^{(t)} = \arccos(1/\lambda)$ is the transition angle between the fillet and main meshing regimes, introduced in Section 4.1.2.

$$\Gamma_{\text{out}} = \big\{\sigma_1(\hat{\theta}) : \hat{\theta} \in (\theta^{(t)},\, 2\pi - \theta^{(t)})\big\}, \tag{4.36}$$

$$\Gamma_{\text{main}} = \big\{\sigma_1^*(\hat{\theta}) : \hat{\theta} \in (\theta^{(t)},\, 2\pi - \theta^{(t)})\big\}, \tag{4.37}$$

$$\Gamma_{\text{in}} = \big\{\sigma_1^*(\hat{\theta}) : \hat{\theta} \in \big(2\pi - \theta^{(t)},\, 2\pi - \theta^{(t)} + \tfrac{2\pi}{N_2}\big)\big\}. \tag{4.38}$$

To track the evolving leakage path, contact points parametrised by $\hat{\theta}$ must be identified for each main rotor rotational angle φ_1 by evaluating the meshing relations $\varphi_1 = \sigma_1(\hat{\theta})$ for the outer leakage path and $\varphi_1 = \sigma_1^*(\hat{\theta})$ for the main and inner leakage paths. However, since $\sigma_1(\hat{\theta})$ may not be injective function along the outer path Γ_{out}, a global inverse $\hat{\theta}(\sigma_1)$ does not exist, and direct interpolation on the uniform main rotor rotational angle grid $\{\varphi_{1,k}\}_{k=0}^{K-1}$ (Equation (4.21)) is unsuitable. To address this, Γ_{out} is partitioned, when necessary, into up to three monotonic sections determined by the principal extrema of $\sigma_1(\hat{\theta})$ on $\hat{\theta} \in (\theta^{(t)}, 2\pi - \theta^{(t)})$. On each section $\sigma_1(\hat{\theta})$ is strictly monotone, allowing $\hat{\theta}$ to be recovered by linear interpolation of $\hat{\theta}$ against φ_1.

Specifically, let $\hat{\theta}_{\min}^{\sigma_1} \in (\theta^{(t)}, \pi)$ be a point at which $\sigma_1(\hat{\theta})$ attains its minimum over $\hat{\theta} \in (\theta^{(t)}, \pi)$, if such a point exists, and let $\hat{\theta}_{\max}^{\sigma_1} \in (\pi, 2\pi - \theta^{(t)})$ be a point at which $\sigma_1(\hat{\theta})$ attains its maximum over $\hat{\theta} \in (\pi, 2\pi - \theta^{(t)})$, if such a point exists. When present, these points split Γ_{out} into, at most, three monotone sections. The main and inner leakage paths are treated analogously, however, they require no further partitioning because σ_1^* is monotone on the chosen subintervals. The parameter maps obtained from linear interpolation of $\hat{\theta}$ against $\varphi_{1,k}$, for each leakage path, are given in Equations (4.39)-(4.43).

$$\Theta_{\text{out},1}(\varphi_{1,k}) = \big\{\hat{\theta} \in \big(\theta^{(t)},\, \hat{\theta}_{\min}^{\sigma_1}\big) :\ \tilde{\sigma}_1(\hat{\theta}) = \varphi_{1,k}\big\}, \tag{4.39}$$

$$\Theta_{\text{out},2}(\varphi_{1,k}) = \big\{\hat{\theta} \in \big(\hat{\theta}_{\min}^{\sigma_1},\, \hat{\theta}_{\max}^{\sigma_1}\big) :\ \tilde{\sigma}_1(\hat{\theta}) = \varphi_{1,k}\big\}, \tag{4.40}$$

$$\Theta_{\text{out},3}(\varphi_{1,k}) = \big\{\hat{\theta} \in \big(\hat{\theta}_{\max}^{\sigma_1},\, 2\pi - \theta^{(t)}\big) :\ \tilde{\sigma}_1(\hat{\theta}) = \varphi_{1,k}\big\}, \tag{4.41}$$

$$\Theta_{\text{main}}(\varphi_{1,k}) = \big\{\hat{\theta} \in \big(\theta^{(t)},\, 2\pi - \theta^{(t)}\big) :\ \tilde{\sigma}_1^*(\hat{\theta}) = \varphi_{1,k}\big\}, \tag{4.42}$$

$$\Theta_{\text{in}}(\varphi_{1,k}) = \big\{\hat{\theta} \in \big(2\pi - \theta^{(t)},\, 2\pi - \theta^{(t)} + \tfrac{2\pi}{N_2}\big) :\ \tilde{\sigma}_1^*(\hat{\theta}) = \varphi_{1,k}\big\}, \tag{4.43}$$

Here, $\tilde{\sigma}_1(\hat{\theta})$ and $\tilde{\sigma}_1^*(\hat{\theta})$ denote the phase–shifted meshing angles, aligned so that the start of the observed working chamber cycle occurs at zero as defined in Equation (4.19).

For the leakage paths in Equations (4.39)–(4.43), given as ordered collections of profile parameters, the global polar coordinates are obtained from the corresponding contact loci Cartesian coordinates in the global coordinate system S_f. The main loci are used for the main and inner paths, and the fillet loci are used for the outer leakage path sections.

Let

$$c_p \in \{c_m, c_f\} \quad \text{with} \quad c_p = \begin{cases} c_m, & \text{for } \Theta_{\text{main}}(\varphi_{1,k}),\ \Theta_{\text{in}}(\varphi_{1,k}), \\ c_f, & \text{for } \Theta_{\text{out},s}(\varphi_{1,k}),\ s \in \{1,2,3\}, \end{cases}$$

and let $\left(x_{c_p}^{S_f}(\hat{\theta}),\, y_{c_p}^{S_f}(\hat{\theta})\right)$ denote the corresponding Cartesian loci coordinates in global coordinate system obtained from Equations (4.15) and (4.16). The global polar coordinates $\left(\rho_{p,c_p}^{S_f}, \varphi_{p,c_p}^{S_f}\right)$ for each contact point along a path (or section), evaluated at $\hat{\theta} \in \Theta_\chi(\varphi_{1,k})$ for $\chi \in \left\{\text{main, in, (out, } s)\right\}$ and $s \in \{1,2,3\}$, can be obtained using Equations (4.44) and (4.45). Polar angle $\varphi_{p,c_p}^{S_f}(\hat{\theta})$ is unwrapped independently along each path to preserve angular continuity across the ordered samples.

$$\rho_{p,c_p}^{S_f}\left(\hat{\theta}\right) = \sqrt{\left(x_{c_p}^{S_f}\left(\hat{\theta}\right)\right)^2 + \left(y_{c_p}^{S_f}\left(\hat{\theta}\right)\right)^2} \tag{4.44}$$

$$\varphi_{p,c_p}^{S_f}\left(\hat{\theta}\right) = \arctan\left(\frac{y_{c_p}^{S_f}\left(\hat{\theta}\right)}{x_{c_p}^{S_f}\left(\hat{\theta}\right)}\right) \tag{4.45}$$

The axial coordinate $z(\varphi_1)$ is related to the main rotor rotational angle through the proportionality between the main rotor wrap angle Φ_1 and the rotor length L_1:

$$\frac{\mathrm{d}z}{\mathrm{d}\varphi_1} = \frac{L_1}{\Phi_1},$$

which in discrete form gives the incremental axial displacement between consecutive contact points as

$$\Delta z_k = \frac{L_1}{\Phi_1}\,\Delta\varphi_{1,k}, \qquad \Delta\varphi_{1,k} = \varphi_{1,k} - \varphi_{1,k-1}.$$

This relation defines the axial progression of the contact locus along the rotor.

The incremental spatial distance between two consecutive contact points on the same leakage path χ is given by the Euclidean arc-length element in polar and axial coordinates, as defined in Equation (4.46), with the initial value $\Delta\ell_{\chi,0} = 0$. The polar coordinates at sample k are

$$\big(\rho_{p,k},\, \varphi_{p,k}\big) = \Big(\rho_{p,c_p}(\hat{\theta}_k),\, \varphi_{p,c_p}(\hat{\theta}_k)\Big), \qquad \hat{\theta}_k = \Theta_\chi(\varphi_{1,k}).$$

If the path or section is undefined at index k, the increment is set to $\Delta\ell_{\chi,k} = 0$.

$$\Delta\ell_{\chi,k} = \sqrt{\Big(\Delta z_k\Big)^2 + \Big(\rho_{p,k}^{S_f}\,\Delta\varphi_{p,k}^{S_f}\Big)^2}, \qquad \Delta\varphi_{p,k}^{S_f} = \varphi_{p,k}^{S_f} - \varphi_{p,k-1}^{S_f}, \qquad k = 1, \ldots, K-1. \tag{4.46}$$

The instantaneous length of path χ at $\varphi_{1,k}$ is the cumulative sum of all previous increments up to k, as defined in Equation (4.47).

$$\ell_{\chi,k} = \sum_{j=1}^{k} \Delta\ell_{\chi,j} \tag{4.47}$$

Since the outer leakage path is partitioned into up to three sections, $s \in \{1, 2, 3\}$, the instantaneous length at $\varphi_{1,k}$ is the section-wise sum of the corresponding lengths, as defined in Equation (4.48).

$$\ell_{\mathrm{out},k} = \sum_{s=1}^{3} \ell_{(\mathrm{out},s),k}(\varphi_{1,k}), \qquad k = 0, \ldots, K-1 \tag{4.48}$$

The cumulative leakage path length $\ell_{\tau,k}(\varphi_{1,k})$, for $\tau \in \{\mathrm{main}, \mathrm{in}, \mathrm{out}\}$, characterises the progressive build-up of the primary leakage path lengths as the main rotor advances. It increases progressively to a maximum, remains at that extent until the rotor has advanced by wrap angle Φ_1, and subsequently decreases. To treat the progression in three dimensions and to remain consistent with the volume calculation, the same extended main rotor rotational angle distribution $\{\varphi_{1,p}\}_{p=0}^{P-1}$ defined in Equation (4.33) is used.

To obtain the actual leakage path length between the observed working chamber and the chamber connected by that path, the cumulative length and its wrap-shifted counterpart are first mapped onto the common main rotor rotational angle grid $\{\varphi_{1,p}\}_{p=0}^{p-1}$, after which their difference is taken.

Let $\ell_{\tau,k}(\varphi_{1,k})$ denote the cumulative length for path τ, defined on $\{\varphi_{1,k}\}_{k=0}^{K-1}$. With linear interpolation $\mathcal{I}_{\{\varphi_{1,k}\}\to\{\varphi_{1,p}\}}$, mapping from $\varphi_{1,k}$ to $\varphi_{1,p}$ grid is defined in Equations (4.49) and (4.50).

$$\ell_{\tau,p}^{(0)}(\varphi_{1,p}) := \mathcal{I}_{\{\varphi_{1,p}\}\to\{\varphi_{1,p}\}}\big[\ \ell_{\tau,k}(\varphi_{1,k})\ \big](\varphi_{1,p}), \tag{4.49}$$

$$\ell_{\tau,p}^{(\Phi_1)}(\varphi_{1,p}) := \mathcal{I}_{\{\varphi_{1,k}\}\to\{\varphi_{1,p}\}}\big[\ \ell_{\tau,k}(\varphi_{1,k}+\Phi_1)\ \big](\varphi_{1,p}). \tag{4.50}$$

The actual leakage path progressive length as a function of the sampled main rotor rotational angle $\varphi_{1,p}$ is given in Equation (4.51).

$$\mathcal{L}_{\tau,p}(\varphi_{1,p}) \ = \ \ell_{\tau,p}^{(0)}(\varphi_{1,p}) \ - \ \ell_{\tau,p}^{(\Phi_1)}(\varphi_{1,p}), \qquad p=0,\ldots,P-1. \tag{4.51}$$

Equation (4.51) provides a discrete and physically consistent calculation of the total three dimensional leakage path length directly from the known contact points.

For each path, the phase-dependent leakage path length $\mathcal{L}_{\tau,p}(\varphi_{1,p})$ is multiplied by the corresponding predefined clearance gap size δ_τ to define the progressive leakage area used as working chamber boundary in the chamber model.

$$\mathcal{A}_\tau(\varphi_{1,p}) = \mathcal{L}_{\tau,p}(\varphi_{1,p})\,\delta_\tau, \qquad p=0,1\ldots,P-1. \tag{4.52}$$

The calculated leakage areas correspond to the boundaries defined by the leakage paths between the current working chamber and the chamber behind. During the progression of the working chamber, it is simultaneously connected to a chamber behind and a chamber ahead, as shown in Figure 4.4. To define the leakage areas connecting the current chamber to the chamber ahead, the areas $A_{\tau,p}(\varphi_{1,p})$ are shifted by either one lobe, $2\pi/N_1$, full revolution, $m_{21}2\pi$, or full revolution minus one lobe, $m_{21}2\pi - 2\pi/N_1$, to obtain

$$A_{\text{main},p}^{(1)}\left(\varphi_{1,p}+\frac{2\pi}{N_1}\right),$$
$$A_{\text{in},p}^{(1)}\left(\varphi_{1,p}+m_{21}2\pi-\frac{2\pi}{N_1}\right),$$
$$A_{\text{out},p}^{(1)}(\varphi_{1,p}+m_{21}2\pi)\,.$$

These leakage areas represent the primary leakage paths (main, inner, and outer) in an internally geared screw machine, correspond to radial leakage that occurs during compression. In addition to radial leakage, axial leakage may also occur at the low-pressure and high-pressure end faces.

To compute the axial leakage path length, the leading and trailing contact path parameter maps, $\Theta_{\ell,k}(\varphi_{1,k})$ and $\Theta_{t,k}(\varphi_{1,k})$ (Equations (4.25)–(4.24)), define the main and gate rotor boundary arcs of the observed working chamber. As discussed in Section 4.1.2, multiple contact pairs may exist at a single main rotor rotational position $\varphi_{1,k}$, corresponding to the opening/closure phases when the observed chamber splits into (or merges from) up to two distinct chambers.

Let $M(k)$ be the number of active trailing–leading contact pairs at $\varphi_{1,k}$, and let $(\hat{\theta}_{t,2}^{(m)}, \hat{\theta}_{\ell,2}^{(m)})$ denote the m-th pair on the gate rotor. The gate rotor boundary arc for the m-th chamber, expressed in polar coordinates of the gate rotor local frame S_2, is

$$\Big(\rho_{p,2}^{S_2}(\hat{\theta}),\, \varphi_{p,2}^{S_2}(\hat{\theta})\Big), \qquad \hat{\theta} \in \big[\hat{\theta}_{t,2}^{(m)},\, \hat{\theta}_{\ell,2}^{(m)}\big], \tag{4.53}$$

where $\big(\rho_{p,2}^{S_2}(\hat{\theta}),\, \varphi_{p,2}^{S_2}(\hat{\theta})\big)$ are the complete profile polar coordinates defined in Equation (4.12).

For a single chamber, the axial leakage path length at the low-pressure end face is approximated as the distance between the maximum radius on the corresponding gate rotor boundary arc and the main rotor root circle of radius r_{r_1}. Figure 4.5 shows the approximated axial leakage line length at the rotor position $\varphi_{1,p}$. Considering all active working chamber parts, axial leakage path length can be calculated as defined in Equation (4.54).

$$\mathcal{L}_{\text{axial},k}(\varphi_{1,k}) = \sum_{m=1}^{M(k)} \max_{\hat{\theta}\in I_m} \rho_{p,2}^{S_2}(\hat{\theta}) - r_{r_1}, \qquad I_m = \big[\hat{\theta}_{t,2}^{(m)},\, \hat{\theta}_{\ell,2}^{(m)}\big] \tag{4.54}$$

Analogous to the radial leakage paths, the axial leakage path lengths are mapped onto the common main rotor rotational angle grid $\{\varphi_{1,p}\}_{p=0}^{P-1}$. The high-pressure end face axial path length is then obtained by shifting the mapped low-pressure by wrap angle, as defined in Equation (4.55).

$$\mathcal{L}_{\text{axial},p}^{(hp)}(\varphi_{1,p}) = \mathcal{L}_{\text{axial},p}^{(lp)}(\varphi_{1,p})(\varphi_{1,p} + \Phi_1) \tag{4.55}$$

Analogous to the radial leakage paths, the phase-dependent axial leakage path lengths at the low and high pressure end faces, $\mathcal{L}^{(\mathrm{lp})}_{\mathrm{axial},p}(\varphi_{1,p})$ and $\mathcal{L}^{(\mathrm{hp})}_{\mathrm{axial},p}(\varphi_{1,p})$, are multiplied by the prescribed clearance gap δ_{axial} to yield the progressive axial leakage path area used as the working chamber boundary in the chamber model. The axial leakage area is defined in Equation (4.56).

$$\mathcal{A}_{\mathrm{axial},p}(\varphi_{1,p}) = \mathcal{L}_{\mathrm{axial},p}(\varphi_{1,p})\,\delta_{\mathrm{axial}}, \qquad p = 0, 1 \ldots, P-1. \tag{4.56}$$

The leakage areas vary with the main rotor rotational angle and serve as the phase-dependent inputs for the chamber model to account for the instantaneous leakage through each sealing path during the working cycle. Figure 4.6 illustrates the radial and axial leakage path areas connecting the current working chamber to the adjacent chambers, one behind (-1) and one ahead $(+1)$, in an internally geared screw machine.

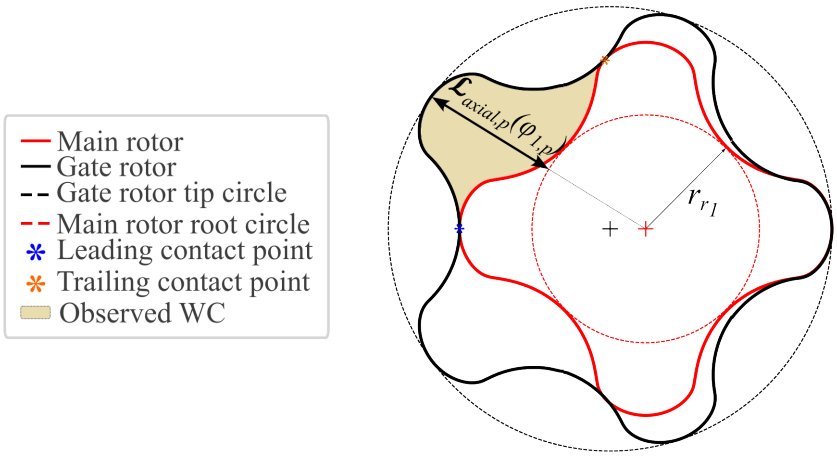

Figure 4.5: Approximation of the axial leakage line length $\mathcal{L}_{\mathrm{axial,p}}(\varphi_{1,p})$ at rotor position $\varphi_{1,p}$, measured from the maximum radius on the outer rotor profile arc to the inner rotor root circle radius.

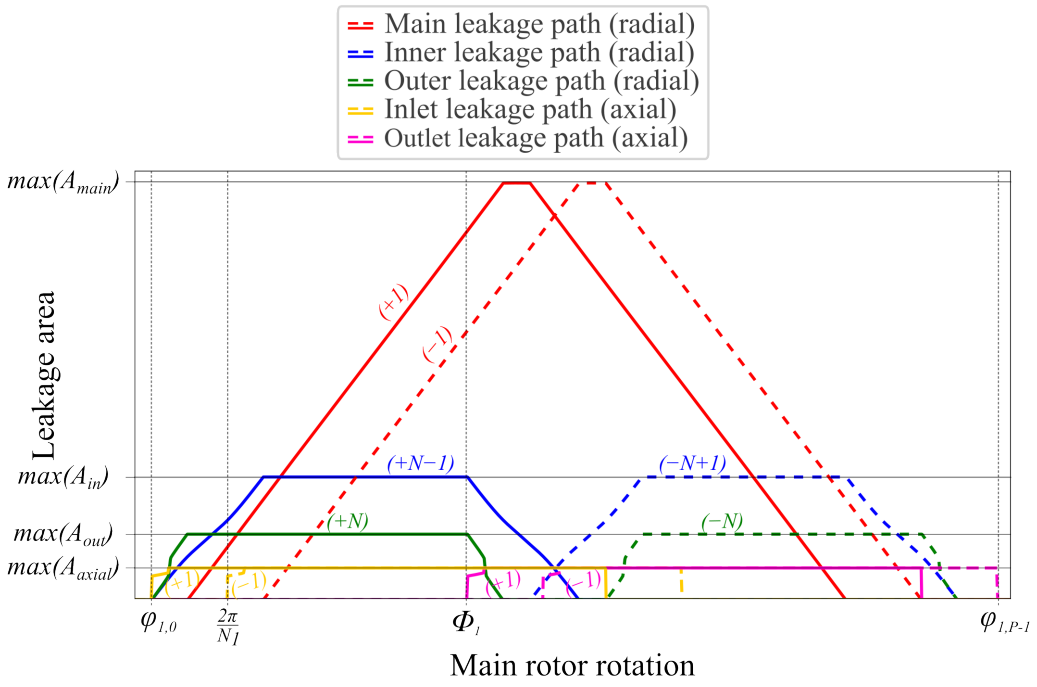

Figure 4.6: Example of existing radial and axial leakage path areas connecting the current working chamber to the adjacent chambers, behind and ahead.

4.1.5 Port Flow Area Estimation

In internally geared screw machines, compression is achieved by the geometry of the end plates, which regulate the timing of fluid entry and exit through the ports [6]. Therefore, a critical step in performance prediction is the accurate estimation of port flow areas as a function of rotor rotational position. In this study, the port shapes are determined numerically in the polar coordinate system, using geometric boundaries such as rotor profiles, contact loci, and bounding circles.

To construct the inlet port shape, the rotor position at which the working chamber reaches its maximum volume is first identified. At this position, two bounding regions are defined in the polar coordinate system:

- The outer boundary is defined by the gate rotor tip circle, the main rotor root circle and contact loci (Figure 4.7 (a) Polygon I).
- The inner region, defined as Polygon II (Figure 4.7 (a)), follows the segments of the rotor profiles and the contact loci bounded between the trailing and leading contact points.

The final inlet port shape is determined by clipping Polygon I with Polygon II, resulting in the blue shaded region shown in Figure 4.7 (a). This clipped polygon is then transformed from the polar coordinate system to the physical domain to obtain the final port shape, also illustrated in Figure 4.7 (a).

The same geometric principles apply to the construction of the outlet port. However, instead of maximum chamber volume, the relevant reference point is defined by the volume index VI, which specifies the relative rotational position at which the working chamber should begin to be exposed to the high pressure end port. An example of the outlet port formation is illustrated in Figure 4.7 (b). As with the inlet, two polygons are defined to compute the outlet port shape:

- Polygon I (Figure 4.7 (b)) is defined by the gate rotor tip circle, the main rotor root circle, the relevant segments of the rotor profiles, and the contact loci associated with the working chamber identified by the selected volume index.
- Polygon II (Figure 4.7 (b)) is based on the contact loci.

The final outlet port shape is determined by clipping Polygon I with Polygon II, resulting in the red shaded region shown in Figure 4.7 (b). The final outlet port shape in physical domain is also illustrated.

While the resulting port geometries display sharp features that may present manufacturing challenges, they represent theoretical maximum openings. As these features occur when the chamber area is small, they can likely be smoothed in practice without significantly affecting performance, however, this aspect is beyond the scope of the present study.

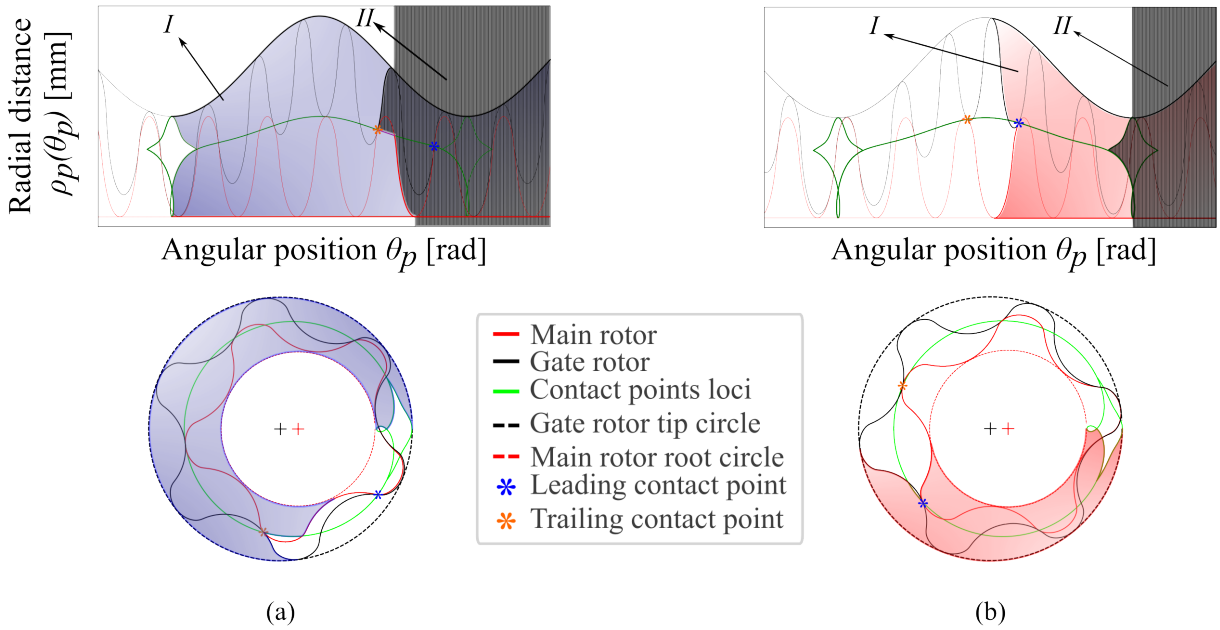

Figure 4.7: End port formation process for the internally geared screw machine. Top plots show the key curve sections for port definition in polar coordinate system. Bottom views illustrate the corresponding shaded regions that define the final end port geometry for the inlet (a) and outlet (b) side. Leading and trailing contact points determine the angular boundaries of the port openings.

Port flow areas relative to the main rotor's rotational position can be determined numerically by constructing a polygon for the tracked working chamber at each rotational step and calculating its intersection with the corresponding port shape polygon.

As discussed in Section 4.1.2, the instantaneous working chamber is bounded by the arcs of the main and gate profiles subtended between the trailing and leading contact points. The leading and trailing contact points for a given main rotor rotational position are obtained from the parameter maps $\Theta_{\ell,k}(\varphi_{1,k})$ and $\Theta_{t,k}(\varphi_{1,k})$ (Equations (4.24)–(4.25)), which define the boundary arcs of the observed chamber. Multiple contact pairs may occur at a single main rotor rotational position $\varphi_{1,k}$, corresponding to opening/closure phases when the chamber splits into, or merges from, up to two distinct chambers.

Let $M(k)$ denote the number of active trailing–leading pairs at index k for main rotor rotational position $\varphi_{1,k}$. Denote the m-th pair by $\big(\hat{\theta}_{t,2}^{(m)},\, \hat{\theta}_{\ell,2}^{(m)}\big)$, for $m = 1, \ldots, M(k)$. The corresponding boundary arc of rotor i in its local frame S_i is

$$\big(x_i^{S_i}(\hat{\theta}),\, y_i^{S_i}(\hat{\theta})\big), \qquad \hat{\theta} \in \big[\hat{\theta}_{t,2}^{(m)},\, \hat{\theta}_{\ell,2}^{(m)}\big],$$

where $\big(x_i^{S_i}(\hat{\theta}),\, y_i^{S_i}(\hat{\theta})\big)$ for $i \in \{1, 2\}$ are the complete profile local coordinates defined in Equations (4.13) and (4.14). The boundary arcs in the global coordinate system S_f are obtained by mapping points from S_i to S_f using the homogeneous transformation matrices $\mathbf{M}_{if}^{(I)}$, $i \in \{1, 2\}$ (Equations (B.3)–(B.4)), as defined in Equation (4.57).

$$\begin{bmatrix} x_i^{S_f}(\hat{\theta}) & y_i^{S_f}(\hat{\theta}) & 0 & 1 \end{bmatrix}^{\top} = \mathbf{M}_{if}^{(I)}(\varphi_{1,k}) \begin{bmatrix} x_i^{S_i}(\hat{\theta}) & y_i^{S_i}(\hat{\theta}) & 0 & 1 \end{bmatrix}^{\top}, \qquad \hat{\theta} \in \big[\hat{\theta}_{t,2}^{(m)},\, \hat{\theta}_{\ell,2}^{(m)}\big]. \tag{4.57}$$

The m-th working-chamber boundary in the global frame S_f is defined as the union of points on the main and gate rotor arcs, each traced between its trailing and leading contact parameters:

$$\begin{aligned} \mathcal{P}_{wc,k}^{(m)}(\varphi_{1,k}) &= \bigcup_{i \in \{1,2\}} \Big\{ \big(x_i^{S_f}(\hat{\theta}),\, y_i^{S_f}(\hat{\theta})\big) \;:\; \hat{\theta} \in \mathcal{I}_m \Big\}, \\ \mathcal{I}_m &= [\,\hat{\theta}_t^{(m)},\, \hat{\theta}_\ell^{(m)}\,], \qquad m = 1, 2, \ldots, M(k). \end{aligned} \tag{4.58}$$

In practice, for each $m = 1, 2, \ldots, M(k)$, $\mathcal{P}_{wc,k}^{(m)}(\varphi_{1,k})$ is discretised and the points are ordered to yield the vertex list of a simple closed polygon representing the m-th chamber boundary.

Let $\mathcal{P}_{in}$ and $\mathcal{P}_{out}$ denote the polygons of the inlet and outlet end ports, respectively, defined in the global coordinate system S_f and corresponding to the physical ports shown in Figure 2.5 (a)–(b). For each sampled main rotor rotational angle $\varphi_{1,k}$, the working chamber areas exposed to the inlet and outlet openings are obtained by overlap of the m-th working-chamber polygon against the inlet and outlet port polygons and summing the resulting overlap areas. Let the m-th overlap polygon for both inlet and outlet side be defined as

$$\mathcal{O}_{in,k}^{(m)} \;=\; \mathcal{P}_{wc,k}^{(m)}(\varphi_{1,k}) \cap \mathcal{P}_{in}, \qquad \mathcal{O}_{out,k}^{(m)} \;=\; \mathcal{P}_{wc,k}^{(m)}(\varphi_{1,k}) \cap \mathcal{P}_{out}, \qquad m = 1, \ldots, M(k).$$

Let area$(\cdot)$ denote the area of a polygon, evaluated via the shoelace formula. For a simple closed polygon $\mathcal{Q} = \{(x_j, y_j)\}_{j=1}^{n}$ with cyclic indexing $(x_{n+1}, y_{n+1}) \equiv (x_1, y_1)$, the shoelace expression is given in Equation (4.59).

$$\text{area}(\mathcal{Q}) \;=\; \frac{1}{2}\left|\sum_{j=1}^{n}\big(x_j\, y_{j+1} - x_{j+1}\, y_j\big)\right|. \tag{4.59}$$

Then the inlet and outlet exposed working chamber areas at a given main rotor rotational position $\varphi_{1,k}$ are obtained from Equation (4.60).

$$A_{in}(\varphi_{1,k}) \;=\; \sum_{m=1}^{M(k)} \text{area}\big(\mathcal{O}_{in,k}^{(m)}\big), \qquad A_{out}(\varphi_{1,k}) \;=\; \sum_{m=1}^{M(k)} \text{area}\big(\mathcal{O}_{out,k}^{(m)}\big). \tag{4.60}$$

An illustrative example of overlapping working chamber and port areas at several rotor positions is shown in Figure 4.8. These overlap computations are performed in two dimensions (in the global coordinate system S_f). To place the resulting exposed areas onto the common angular grid $\{\varphi_{1,p}\}$ used throughout the geometry calculations (defined in Equation (4.33)) and to associate them with the corresponding three-dimensional positions, the inlet and outlet traces are remapped. The inlet area is interpolated directly from the sampling set $\{\varphi_{1,k}\}$ to $\{\varphi_{1,p}\}$, whereas the outlet area is first phase-shifted by the main rotor wrap angle Φ_1 and then interpolated to the same grid as defined in Equation (4.61), where $\mathcal{I}_{\{\varphi_{1,k}\}\to\{\varphi_{1,p}\}}$ denotes interpolation from the sampled rotational angles $\{\varphi_{1,k}\}$ onto the common grid $\{\varphi_{1,p}\}$. Figure 4.9 illustrates an example of the estimated position and shape of the port flow area.

$$\begin{aligned} A_{in}^{\star}(\varphi_{1,p}) &:= \mathcal{I}_{\{\varphi_{1,k}\}\to\{\varphi_{1,p}\}}[A_{in}(\varphi_{1,k})]\,(\varphi_{1,p}) \\ A_{out}^{\star}(\varphi_{1,p}) &:= \mathcal{I}_{\{\varphi_{1,k}\}\to\{\varphi_{1,p}\}}[A_{out}(\varphi_{1,k} + \Phi_1)]\,(\varphi_{1,p}) \end{aligned} \tag{4.61}$$

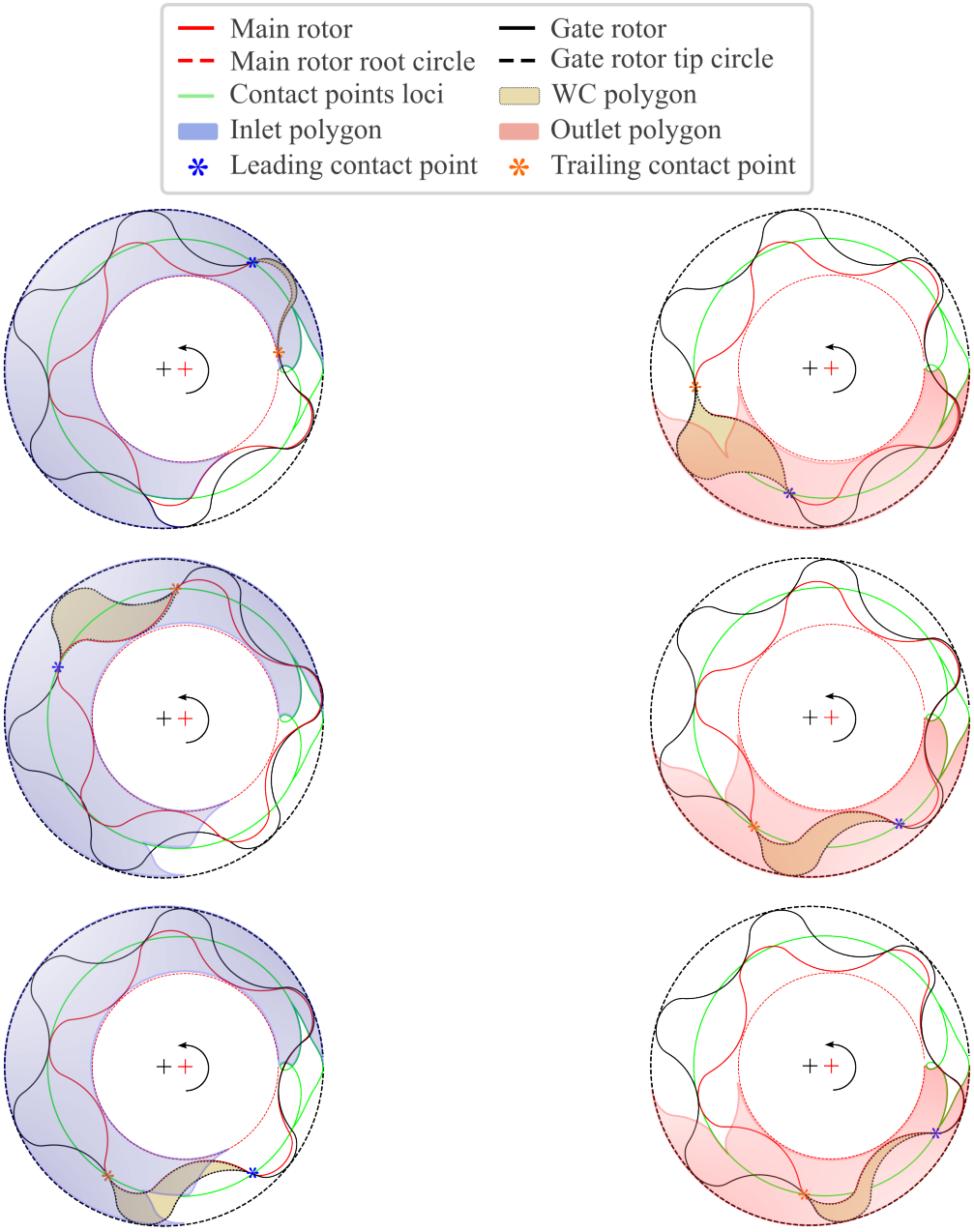

Figure 4.8: Illustration of working chamber and port end area overlap for several rotor positions: (a) inlet side and (b) outlet side.

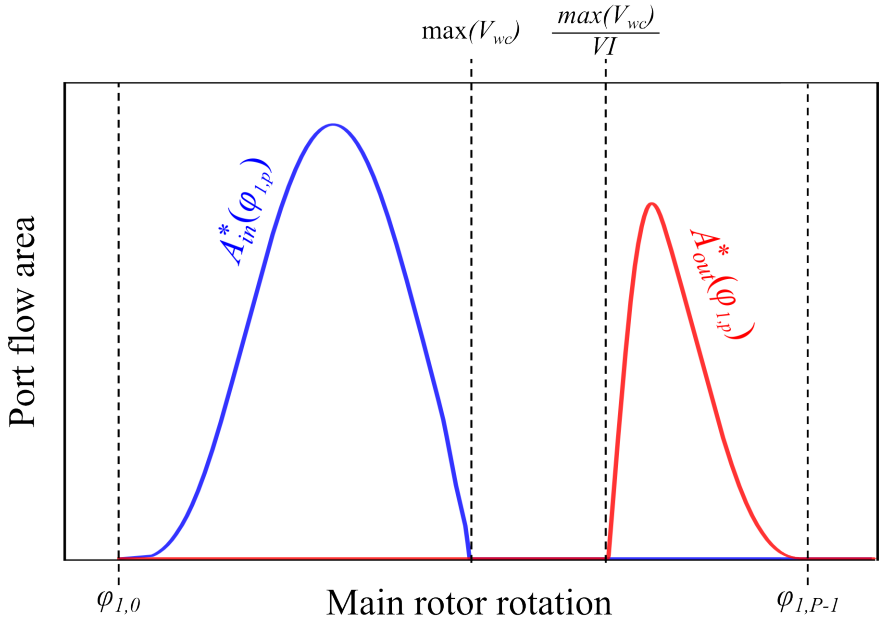

Figure 4.9: Example of estimated port flow areas shown with respect to the main rotor rotational position φ_1: inlet side (blue) and outlet side (red).

4.1.6 Computational Performance of the Geometry Model

The geometry model described in Section 4.1 is implemented in *C++*, following object oriented programming principles to provide a modular design that enables consistent evaluation and straightforward updates. As the model is intended for parametric studies and optimisation, the computational time per geometry evaluation was assessed across 10,000 configurations within the parameter ranges listed in Table 4.1. Experiments were conducted on a machine equipped with an NVIDIA RTX 3060 (laptop GPU), an AMD Ryzen 7 5800H CPU, and 16GB DDR4 RAM.

A full geometry evaluation includes (i) working chamber volume, (ii) leakage areas, and (iii) port flow areas. The last component dominates runtime due to iterative evaluation over rotor angle, repeated polygon construction, polygon–polygon intersection, and multiple applications of the shoelace formula (given in Equation (4.59)) per iteration. In a single-thread (serial) implementation, the port flow area calculation required approximately 3.8s on average. By parallelising the outlet and inlet port flow area calculations across two CPU threads, this reduced to approximately 2.2s on average. With other steps contributing about 0.093s, total average computational time per evaluation decreased from 3.818s (serial) to $\approx$ 2s (two threads). The detailed breakdown is given in Table 4.2.

Table 4.1: Parameter ranges used in the computational time analysis (10,000 configurations).

Quantity	**Symbol / Unit**	**Range**
Main rotor lobe count	N_1	$[2, 7]$
Profile parameter (pin-generation)	λ	$[1.01, 10]$
Profile parameter (pin-generation)	$\bar{\sigma}$	$[0.10, 0.99]$
Main rotor wrap angle	Φ_1 [deg]	$[100, 500]$
Built in volume index	VI	$[1.5, 10]$

Table 4.2: Mean computational times per geometry evaluation (averaged over 10,000 configurations). Serial means outlet and inlet port flow area calculations run sequentially; parallel means outlet and inlet run concurrently on two CPU threads.

Component	**Computational time**
Working-chamber volume	0.004s
Leakage areas	0.089s
Port flow areas (Serial)	3.725s
Port flow areas (Parallel)	1.904s
Total per evaluation (Serial)	**3.818s**
Total per evaluation (Parallel)	**1.997s**

4.2 Machine Learning Model for Port Flow Area Estimation

The computational performance assessment in Section 4.1.6 shows that the dominant computational cost arises from evaluating port flow areas, due to the iterative polygon construction, overlap operations, and repeated area integrations. For optimisation and parametric studies, large configuration sets quickly amplify this cost, making reductions in computational time and algorithmic complexity essential.

As port flow area evaluation accounts for the vast majority of runtime (>95%), a dedicated surrogate is well justified. Prior engineering literature demonstrates that machine learning surrogates based on Gaussian processes or deep neural networks can accurately predict distribution type quantities from geometric and operating inputs, achieving orders-of-magnitude speed-ups while preserving shape fidelity, making them well suited to this task [52–55].

4.2.1 Training Dataset

The training dataset is generated using the geometry model described in Section 4.1. Configuration points are selected within the parameter ranges listed in Table 4.1, which cover the majority of practically relevant configurations. For each configuration, the model computes paired port flow area curves for the inlet and outlet end ports together with the corresponding main rotor rotational angles. Each row of the training data therefore contains a set of scalar parameters followed by four arrays that store main rotor angles and port flow areas for both the inlet and outlet curves.

Let $S = 1600$ be the number of samples per curve and $P = 8$ the number of scalar parameters. The first P columns contain the scalar inputs listed in Table 4.3. After these P columns, four contiguous blocks of length S store the arrays for angles and port flow areas as summarised in Table 4.4. The total number of columns is $P + 4S = 8 + 4 \times 1600 = 6408$. All P parameters except the volume index VI influence the shape and angular position of the inlet port flow area curve. All parameters, including VI, influence the shape and angular position of the outlet port flow area curve.

Table 4.3: First eight parameter columns of the port flow area training dataset.

Index	**Name**	**Description**
0	N_1	Main rotor lobe count
1	$\bar{\sigma}$	Non–dimensional profile parameter (pin–generation)
2	λ	Non–dimensional profile parameter (pin–generation)
3	$\Phi_1[rad]$	Main rotor wrap angle (absolute)
4	VI	Built–in volume index
5	$\max(\mathcal{A}_{\mathrm{wc}})[mm^2]$	Maximum working chamber area
6	$\varphi_{1,c}^{(\mathrm{start})}[rad]$	Compression start angle
7	$\varphi_{1,c}^{(\mathrm{end})}[rad]$	Compression end angle

Table 4.4: Curve data blocks following the P scalar parameters: the remaining columns contain the outlet (high pressure) and inlet (low pressure) port flow area arrays together with their respective main rotor rotational angle arrays.

Column range	**Contents**
$[P : P+S)$	ϕ_{lp} main rotor angles for inlet curve
$[P+S : P+2S)$	Inlet port flow area values
$[P+2S : P+3S)$	ϕ_{hp} main rotor angles for outlet curve
$[P+3S : P+4S)$	Outlet port flow area values

4.2.2 Model Training

To prepare the port flow area curves for training, each curve is normalised by the maximum working chamber area, $\max(\mathcal{A}_{\text{wc}})$, which upper bounds the port flow area at any rotor position. This places all target values within $[0, 1]$ range and helps the model detect features consistently. Since $\max(\mathcal{A}_{\text{wc}})$ is provided as an input parameter, predicted curves can be rescaled to physical units after inference. The horizontal phase axis is standardised using the compression start and end angles $\varphi_{1,c}^{(\text{start})}$ and $\varphi_{1,c}^{(\text{end})}$ where each curve is translated and linearly scaled onto a common interval $[0, 1]$, ensuring consistent alignment across samples. Normalised examples of both inlet and outlet curves are shown in Figure 4.10.

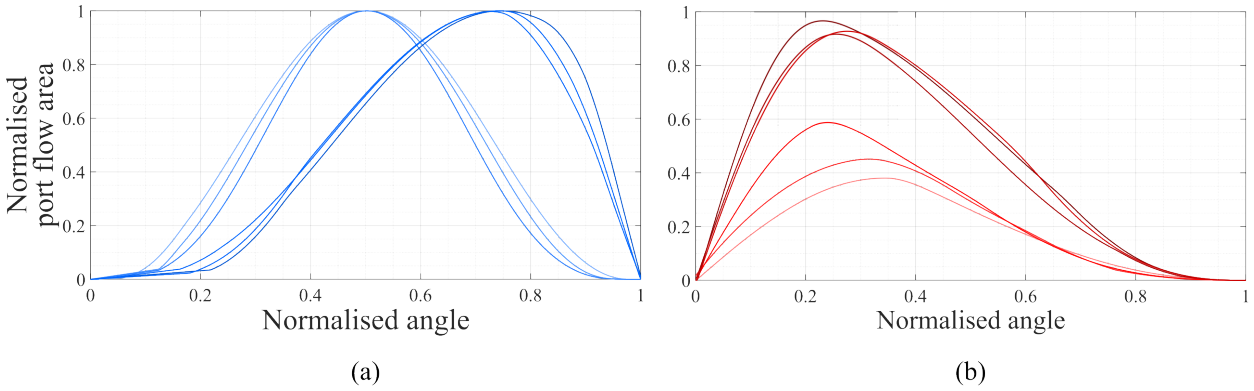

Figure 4.10: Examples of normalised port flow area curves: (a) inlet (low-pressure) port and (b) outlet (high-pressure) port, each scaled to $[0, 1]$ in both amplitude and phase.

The normalised port flow area curves can be treated as signals of the main rotor rotational angle, with shape determined by many geometric and operating variables (up to P inputs). The prediction task is therefore a supervised curve-fitting problem that learns a mapping from the parameter vector to the sampled signal. Directly regressing the full discretised curve is high-dimensional and redundant, thus the training targets are first compressed using Principal Component Analysis (PCA). PCA is a linear method that expresses each mean centred signal as a low-dimensional combination of orthonormal components while preserving most of the signal variance [63, 64].

Let $\mathbf{y} \in \mathbb{R}^S$ denote a mean–centred, discretised curve over S main rotor rotational angle samples, $\boldsymbol{\mu} \in \mathbb{R}^S$ the mean curve, and $\mathbf{Z}_k = [\,\mathbf{z}_1, \ldots, \mathbf{z}_K\,] \in \mathbb{R}^{S\times K}$ the first K principal components. PCA provides the representation

$$\mathbf{y} \approx \boldsymbol{\mu} + \mathbf{Z}_k\, \boldsymbol{a}, \qquad \boldsymbol{a} = \mathbf{Z}_k^{\top}(\mathbf{y} - \boldsymbol{\mu}), \tag{4.62}$$

where the coefficient vector $\boldsymbol{a} \in \mathbb{R}^K$ with $K \ll S$.

In this work, K is chosen so that the retained components explain at least 99% of the total signal variance, yielding accurate reconstruction with substantial dimensionality reduction. The supervised model is trained to predict the coefficient vector $\boldsymbol{a}$ from the input parameter vector $\mathbf{x} \in \mathbb{R}^P$. The normalised port flow area curve is then recovered by the inverse transform in Equation (4.62).

To map the input parameter vector to the PCA coefficients, Gaussian Process Regression is implemented [65]. Let $\mathbf{x} \in \mathbb{R}^P$ denote the input parameter vector and $\boldsymbol{a} = [a_1, \ldots, a_K]^{\top}$ the retained PCA coefficient vector. A separate Gaussian process (GP) is trained for each retained PCA coefficient a_j,

$$a_j(\mathbf{x}) \sim \mathcal{GP}\big(m_j(\mathbf{x}),\, k_j(\mathbf{x}, \mathbf{x}')\big), \qquad j = 1, \ldots, K,$$

with a zero-mean prior $m_j(\mathbf{x}) = 0$ and an Automatic Relevance Determination (ARD) squared exponential kernel [66] with a constant term and white noise,

$$k_j(\mathbf{x}, \mathbf{x}') = \underbrace{\sigma_{f,j}^2 \exp\Big(-\tfrac{1}{2} \sum_{d=1}^{P} \tfrac{(\mathbf{x}_d - \mathbf{x}'_d)^2}{\ell_{j,d}^2} \Big)}_{\text{ARD squared exponential}} + \underbrace{\sigma_{0,j}^2}_{\text{constant term}} + \underbrace{\sigma_{n,j}^2\, \delta_{\mathbf{x},\mathbf{x}'}}_{\text{white noise (Kronecker delta)}} .$$

Here, ARD is chosen to allow the model to determine which inputs matter for predicting each PCA coefficient. In high-dimensional design spaces, the input parameters (in this work, machine configuration parameters) rarely contribute equally to the output shape (in this case, port flow area shape), thus letting the model learn input-specific sensitivities supports automatic feature selection. The ARD squared exponential term provides smoothness with one length-scale per input $\{\ell_{j,d}\}_{d=1}^{P}$. Large $\ell_{j,d}$ implies that a_j barely changes along input d (low relevance), whereas small $\ell_{j,d}$ allows rapid variation (high relevance). This use of ARD within Gaussian process regression is standard and well studied in similar engineering applications [65, 67–69].

The constant term $\sigma_{0,j}^2$ captures a global covariance trend, and the white–noise term $\sigma_{n,j}^2\delta_{x,x'}$ accounts for numerical noise and improves numerical conditioning. Training maximises the log marginal likelihood to estimate the kernel hyper-parameters $\{\ell_{j,d}, \sigma_{f,j}, \sigma_{0,j}, \sigma_{n,j}\}$ from the training data [65].

The dataset is split into 70% training and 30% testing. After fitting the K independent GPs on the training set, a new input $\mathbf{x}$ yields the mean and variance for each coefficient a_j. The port flow area curve is then recovered via the inverse PCA transform in Equation (4.62). This workflow provides calibrated uncertainty for the coefficient predictions and, through PCA, for the reconstructed curves. A schematic of the PCA-GP surrogate modelling workflow is shown in Figure 4.11.

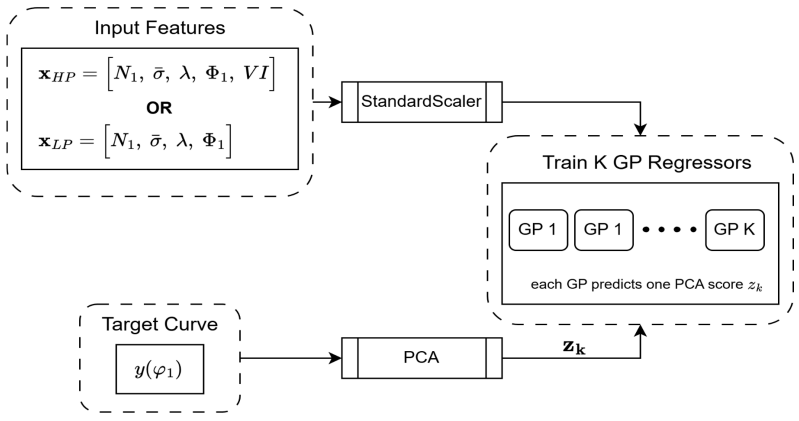

Figure 4.11: Training procedure of the PCA-GP surrogate model. The input features are standardised, while the target curve $y(\varphi_1)$ is reduced using PCA. The retained PCA coefficients are then predicted using K independent Gaussian process regressors.

4.2.3 Model Evaluation

Training is performed separately for inlet and outlet port flow area models. For the inlet case, test set metrics are summarised in Table 4.5, reporting the explained variance ratio, root–mean–squared error (RMSE), mean–absolute error (MAE), R^2, and distributional measures of the integral error (median and 95th percentile).

The explained variance ratio of 0.99 indicates that PCA preserves essentially all curve energy with $K = 6$ principal components. The RMSE and MAE are very small, and $R^2 = 0.99$ confirms excellent predictive fit. Median and 95th–percentile integral errors of 0.07% and 0.26% show that the area under the predicted curve is recovered with high accuracy across the test set. Figure 4.12 shows examples of normalised true and predicted inlet port flow area curves for four test cases, demonstrating close agreement in shape.

Table 4.5: Test set metrics for the predicted inlet (low pressure) port flow area; errors are computed in original units.

Metric	**Value**
Explained variance ratio	0.99
RMSE	5.0×10^{-6}
MAE	3.0×10^{-6}
R^2	0.99
Median relative integral error	0.07%
95th percentile integral error	0.26%

Analogous to the inlet port flow area model, the outlet model is evaluated on the held-out test set and summary metrics are reported in Table 4.6. With $k = 5$ components and an explained variance ratio of 0.99, PCA retains the essential structure of the outlet port flow area curves while reducing dimensionality. Test errors are very small in the original units, and $R^2 = 0.99$ indicates that the surrogate explains nearly all variance in the held-out data. The median and 95th-percentile integral errors (0.21% and 0.61%) are slightly higher than for the inlet case, but still reflect accurate recovery of the area under curve behaviour across the test set. Figure 4.13 shows examples of normalised true and predicted outlet port flow area curves for four test cases, demonstrating close agreement in shape.

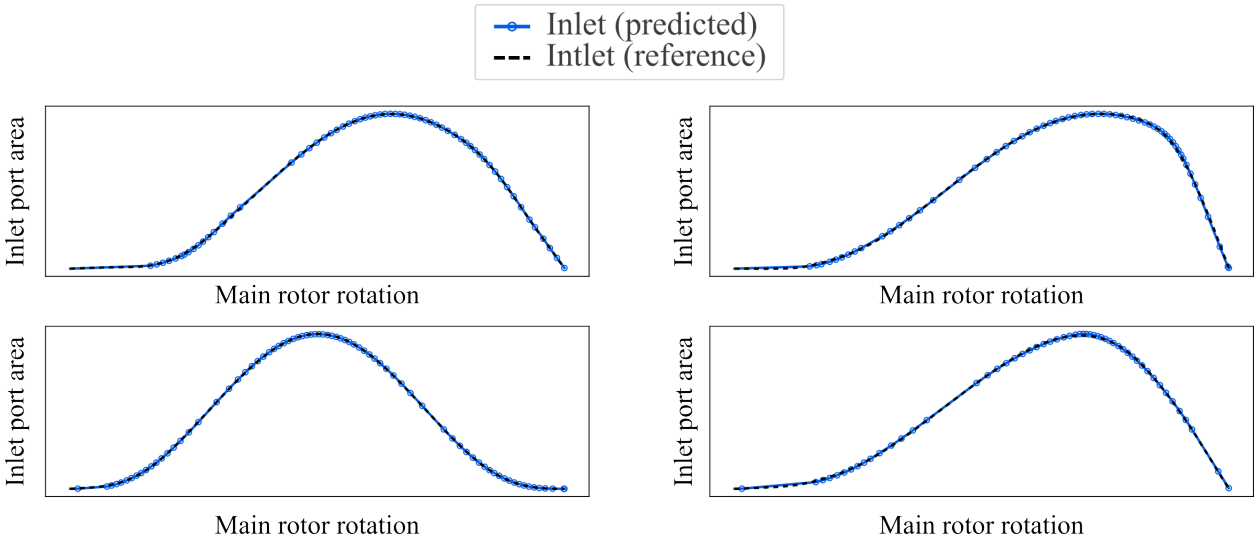

Figure 4.12: Normalised inlet port flow area curves for four test cases from the held-out set, showing close agreement between the surrogate estimates and the reference (ground-truth) curves; both amplitude and phase are scaled to $[0, 1]$.

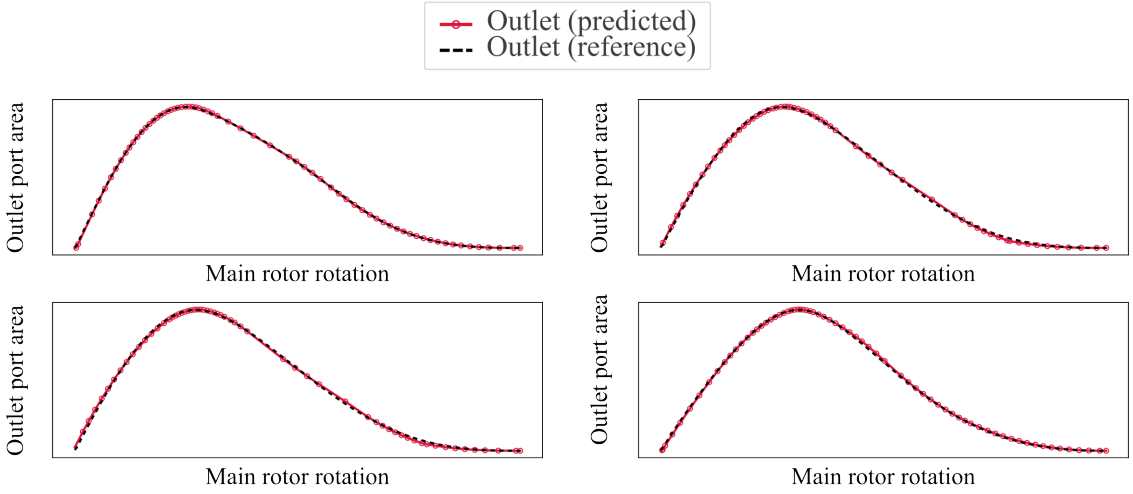

Figure 4.13: Normalised outlet port flow area curves for four test cases from the held-out set, showing close agreement between the surrogate estimates and the reference (ground-truth) curves; both amplitude and phase are scaled to $[0, 1]$.

Both models provide suitable surrogates for estimating port flow area curves from the machine configuration inputs and produce outputs in normalised form. To recover physical units, the predicted curves are rescaled using maximum working chamber area, $\max(\mathcal{A}_{\text{wc}})$, and mapped onto the appropriate main rotor rotational angle grids, with the inlet defined from 0 to the compression

Table 4.6: Test set metrics for the predicted outlet (high pressure) port flow area; errors are computed in original units.

Metric	**Value**
Explained variance ratio	0.99
RMSE	4.0×10^{-6}
MAE	2.0×10^{-6}
R^2	0.99
Median relative integral error	0.21%
95th percentile integral error	0.61%

start angle $\varphi_{1,c}^{(\text{start})}$ and the outlet defined from the compression end angle $\varphi_{1,c}^{(\text{end})}$ to the cycle end. An example of predicted port flow areas in physical scale is shown in Figure 4.14, together with reference curves obtained via the polygon-based method described in Section 4.1.5.

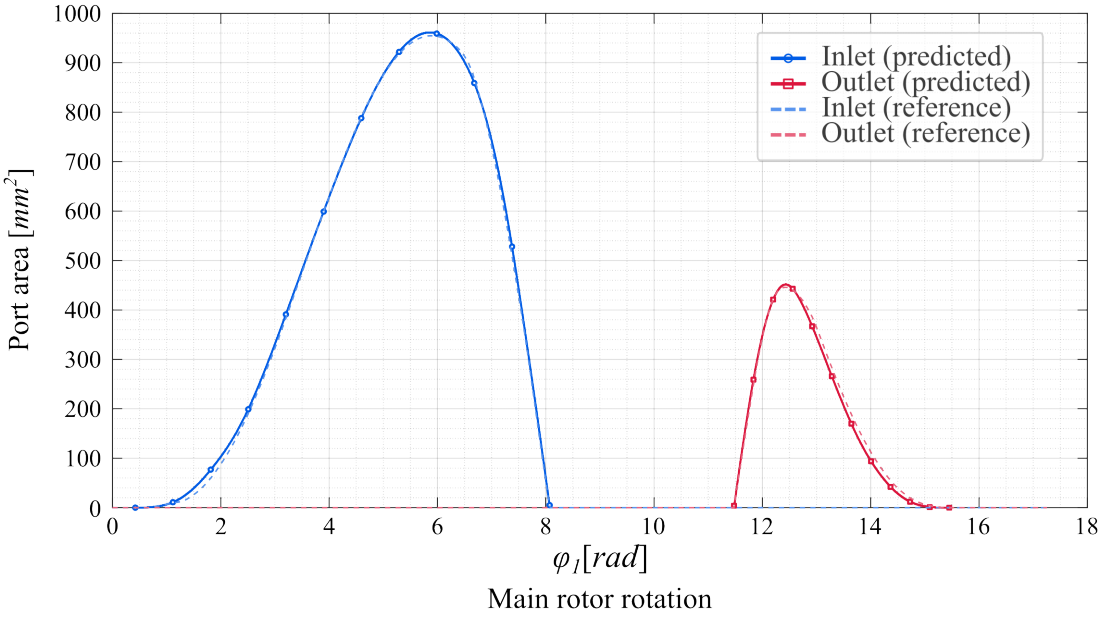

Figure 4.14: Example of reconstructed physical port flow area curves from the surrogate (inlet and outlet), rescaled by $\max(\mathcal{A}_{\text{wc}})$ and mapped to their respective angle intervals. Reference curves from the polygon-based calculation (Section 4.1) are shown for comparison. Here machine configuration is $\lambda = 1.1$, $\bar{\sigma} = 0.8$, $E = 8.3$mm, $VI = 3$, $\Phi_1 = 200°$ and $L_1 = 0.130$mm.

Computational performance is benchmarked over the same bounds as Table 4.1 using 10,000 con-

figurations. Table 4.7 compares the polygon based baseline with the surrogate estimator and shows clear speed ups of two orders-of-magnitude in favour of the surrogate.

Table 4.7: Timing per geometry evaluation for 10,000 configurations. Speed up is reported relative to the polygon based serial baseline.

Method	**Mode**	**Time per evaluation**	**Speed up**
Polygon based	Serial	3.818 s	1×
Polygon based	Parallel (2 threads)	1.997 s	≈ 1.91×
Surrogate	Serial	20 ms	≈ 191×
Surrogate	Parallel (2 threads)	10 ms	≈ 382×

Although the model is reliable and accurate for machine configuration inputs within the training bounds, its ability to generalise to inputs outside the limits in Table 4.1 should be addressed in future work if deployment beyond these ranges is intended.

4.3 Outcome

This chapter presented a detailed numerical implementation of the internally geared screw machine geometry model. The workflow covers: (i) rotor profiling using circular pin–generation method, (ii) working chamber formation through contact point identification and tracking, (iii) working chamber area computation and volume integration, (iv) modelling of the relevant leakage paths, and (v) formulation of inlet and outlet port flow areas.

Since the polygon-based port flow area evaluation was identified as the dominant computational cost over the operating envelope analysed in Section 4.1.6, a surrogate that combines Principal Component Analysis (PCA) with Gaussian Process Regression (GPR) was introduced in Section 4.2. This surrogate delivers substantially faster estimates of inlet and outlet port flow areas while preserving accuracy within the studied configuration bounds.

The resulting geometry module is well suited for integration with performance prediction tools, and it provides rapid evaluation of geometry quantities, making it suitable for large parametric and optimisation studies.

5 Performance Simulation and Evaluation of the Internally Geared Screw Machine

Developing reliable and accurate performance prediction models for internally geared screw machines is a crucial step in the design process. CFD tools are widely used for such analyses but are computationally intensive and time-consuming, thus there is clear value in a robust chamber model that enables faster simulations, particularly for optimisation where many design points must be explored. In this work, the developed geometry model is coupled with an existing one-dimensional chamber model to assess performance. Section 4.1 details the geometry formulation for the internally geared screw machine, including identification and tracking of contact points and the associated working chamber. The working chamber volume, leakage areas, and port flow areas are evaluated as functions of the main rotor rotational position and are passed as inputs to the `SCORG` multi-chamber model [9]. Although this model has been validated for conventional twin screw machines in the past [15, 46, 57], validation for internally geared screw machines requires dedicated experiments on a purpose-built test rig. As that rig is still under development due to the complexity of manufacturing the outer rotor, experimental validation is not yet feasible. As an initial evaluation of the integrated approach, chamber model predictions are therefore compared with higher-fidelity CFD simulations reported in recent IGSM study [56], providing a preliminary check on trends and magnitudes in the absence of experimental measurements.

Conventional twin screw compressors have a lower size limit and one of the smallest commercially available models is VMC Italy's V60 with a 60mm main rotor diameter [16]. One of the initial assumptions regarding internally geared screw machine potential benefits is the ability to operate below this lower bound. As a first step, a parametric study is conducted to identify internally geared screw machine geometries with the same volume displacement as the V60. This study maps the design space and highlights parameter combinations associated with higher predicted efficiency. A representative design from the sweep is then selected and benchmarked against the V60 across a range of rotational speeds and pressure ratios, along with a comparison of overall geometry and machine size.

5.1 Comparison of CFD and Chamber Model

In the present work, CFD is used primarily as a reference for verification of the implemented IGSM geometry and chamber based thermodynamic model. The CFD data used for this validation is taken from Rane et al. [56], where the representative internally geared screw machine case summarised in Table 5.1 was examined in detail. The same case is adopted here for direct comparison between the CFD predictions and the chamber model results. As the numerical methodology, assumptions, and boundary conditions are consistent with that earlier study, the detailed CFD setup is given in Appendix D, while the chamber model used for comparison is summarised in Appendix C. This section therefore focuses only on the validation context and results.

Table 5.1: Representative internally geared screw machine (IGSM) configuration used to compare computational fluid dynamics (CFD) results with the one dimensional chamber model, collected from a recent CFD study [56].

Unit	Value	Description
(-)	6	Outer rotor lobe number (N_2)
(-)	5	Inner rotor lobe number (N_1)
(mm)	100	Diameter of outer rotor (D_2)
(mm)	130	Length of both rotors (L)
(mm)	6.712	Axis spacing distance (E)
(-)	1.4	Profile shape parameter (λ)
(-)	0.8	Profile shape parameter ($\bar{\sigma}$)
(°)	234	Inner rotor wrap angle (Φ_1)
(-)	2	Built-in volume ratio (VI)

Both models, chamber and CFD, are evaluated for oil-free and oil-injected conditions across a range of discharge pressures and rotor speeds. The cases included in this comparison are listed in Table 5.2.

Table 5.2: Operating conditions used for comparison between CFD and chamber model for both oil-free and oil-injected IGSM configurations.

Intake pressure [bar]	Discharge pressure [bar]	Main rotor speed [rpm]
Oil-free		
1	2	2000
1	2	3000
1	2	4000
1	3	3000
1	3	4000
Oil-injected		
1	2	2000
1	2	3000
1	2	4000
1	3	2000
1	3	3000
1	3	4000

Figure 5.1 compares the predictions from the chamber model and CFD simulations for various performance parameters across a range of main rotor speeds and discharge pressures in oil-free operation. The corresponding numerical values of the CFD and chamber model predictions for these oil-free cases are summarised in Tables 5.3 and 5.4, respectively.

The chamber model accurately predicts the air flow rate (Figure 5.1 (a)), showing excellent agreement with CFD results at both $2bar$ and $3bar$ discharge pressures. Although a slight mismatch is observed at lower rotor speeds, the linear trend with increasing speed is well captured.

Predicted input power shows good agreement (Figure 5.1 (b)), especially at discharge pressure of $2bar$. For $3bar$, the chamber model slightly over-predicts the required power compared to CFD, but the trend with increasing speed remains consistent.

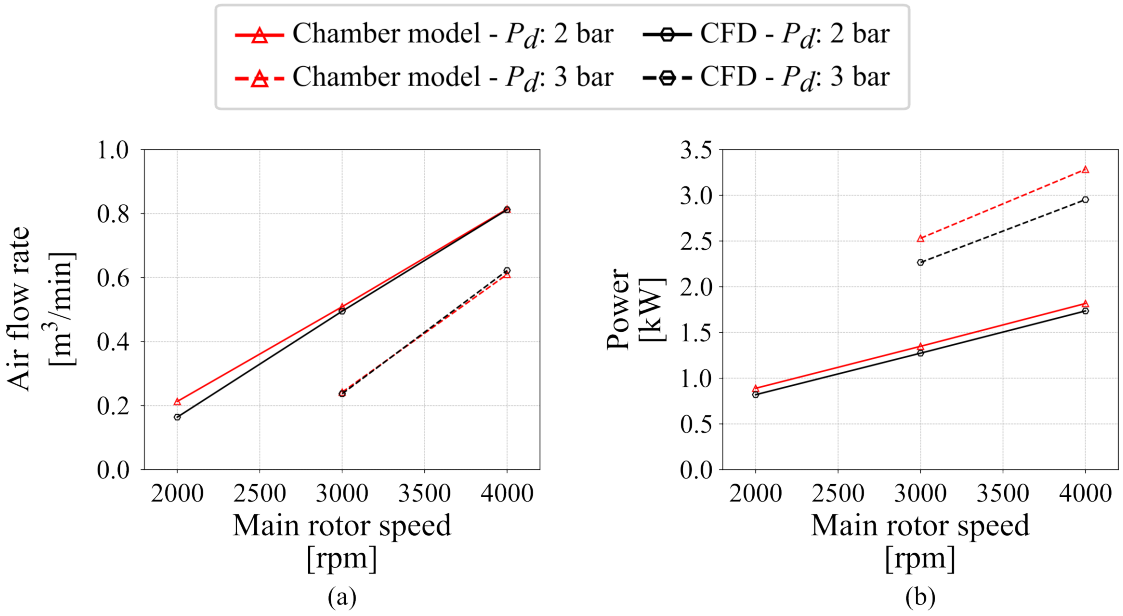

Figure 5.1: Comparison between the chamber model and CFD results for the oil-free internally geared screw machine configuration specified in Table 5.1, evaluated for operating conditions defined in Table 5.2. The plots show: (a) air flow rate and (b) indicated power across varying main rotor speeds for two pressure ratios.

Table 5.3: CFD model results for the oil-free IGSM configuration listed in Table 5.1, used for comparison with the chamber model in Figure 5.1.

P_2 (bar)	ω_1 (rpm)	Q (m^3/min)	Power (W)	η_v (%)	T_2 (°C)	P_{sp} (kW/(m^3/min))	η_{ad} (%)
2	2000	0.16	820	27.64	240	5.01	25.50
2	3000	0.49	1274	55.76	158	2.57	49.70
2	4000	0.81	1735	68.56	132	2.14	59.80
3	3000	0.24	2265	26.72	420	9.55	22.50
3	4000	0.62	2952	52.51	268	4.75	45.30

Table 5.4: Chamber model results for the oil-free IGSM configuration listed in Table 5.1, used for comparison with the CFD results in Figure 5.1.

P_2 (bar)	ω_1 (rpm)	Q (m^3/min)	Power (W)	η_v (%)	T_2 (°C)	P_{sp} (kW/(m^3/min))	η_{ad} (%)
2	2000	0.21	890	32.06	187	4.19	30.58
2	3000	0.51	1349	57.45	157	2.65	48.23
2	4000	0.81	1817	68.84	138	2.23	57.20
3	3000	0.24	2530	27.28	470	10.46	20.56
3	4000	0.61	3284	51.57	293	5.39	39.93

Figure 5.2 compares the performance predictions of the chamber model with CFD results for oil-injected operation of the internally geared screw machine. The comparison includes various performance parameters for the evaluated cases.The corresponding numerical values of the CFD and chamber model predictions for these oil-injected cases are summarised in Tables 5.5 and 5.6, respectively.

In Figure 5.2 (a), the air flow rate predicted by the chamber model shows decent agreement with CFD across all operating conditions. Both models capture the linear increase in flow rate with rotor speed. This indicates the chamber model's robustness in simulating flow behaviour under oil-injected conditions.

Figure 5.2 (b) presents the power input required by the machine. The chamber model closely tracks the CFD results for evaluated cases. The increasing trend is also captured accurately suggesting that the behaviour of chamber model is sufficient.

The discrepancy between the chamber model and CFD predictions seen in Figures 5.1 and 5.2 is more pronounced for the oil-free cases, particularly in the predicted indicated power at the higher discharge pressure. From Tables 5.3–5.6, it can be observed that the air flow rate is generally matched consistently, whereas the discharge temperature shows the largest deviation among the reported quantities. This indicates that the overprediction of power is likely associated with differences in the predicted thermodynamic state during compression, which is strongly influenced by the leakage flow representation. In oil-free operation, the clearance flows are not modified by the presence of injected oil, making the prediction more sensitive to the simplified clearance gap geometry

used in the chamber model. Therefore, future work should consider a more detailed representation of the clearance gap geometry to better reproduce the three-dimensional leakage topology captured by CFD. The reduced discrepancy observed in the oil-injected cases further supports this interpretation, since the oil-injection treatment in the existing chamber model, described in Appendix C, effectively alters the flow and heat-transfer behaviour within the clearances.

Overall, the chamber model performs reliably for oil-injected operation, reproducing key trends and magnitudes across performance metrics. Discrepancies at low speeds and higher pressures are modest and expected due to the complexity of flow modelling and heat transfer in oil-injected machines, which are not explicitly resolved in the chamber model. Nevertheless, these results support the chamber model's suitability for design exploration and optimisation tasks where faster performance estimation is required.

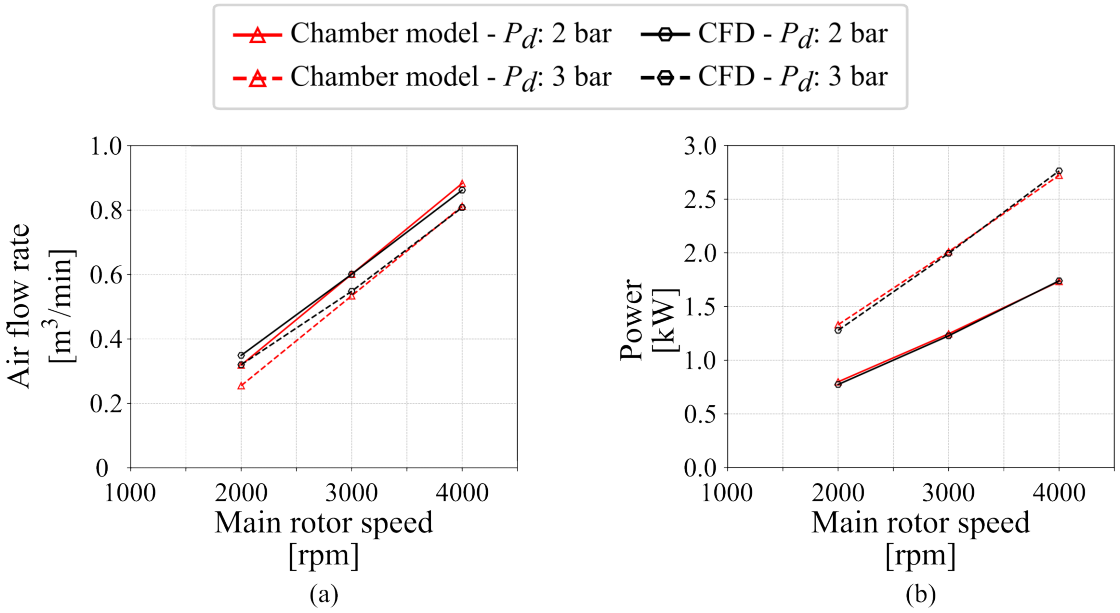

Figure 5.2: Comparison between the chamber model and CFD results for the oil-injected internally geared screw machine configuration defined in Table 5.1, using operating conditions listed in Table 5.2. The subfigures present: (a) air flow rate and (b) indicated power across different main rotor speeds for two discharge pressures.

Table 5.5: CFD model results for the oil-injected IGSM configuration listed in Table 5.1, used for comparison with the chamber model in Figure 5.2.

P_2 (bar)	ω_1 (rpm)	Q (m^3/min)	Power (W)	η_v (%)	T_2 (°C)	P_{sp} (kW/(m^3/min))	η_{ad} (%)
2	2000	0.35	774	58.98	72.50	2.22	57.50
2	3000	0.60	1228	67.83	81.50	2.04	62.60
2	4000	0.86	1740	72.94	101.50	2.02	63.30
3	2000	0.32	1278	54.14	71.60	3.99	53.80
3	3000	0.55	1995	61.81	83.40	3.64	59.10
3	4000	0.81	2764	68.39	94.40	3.42	62.90

Table 5.6: Chamber model results for the oil-injected IGSM configuration listed in Table 5.1, used for comparison with the CFD results in Figure 5.2.

P_2 (bar)	ω_1 (rpm)	Q (m^3/min)	Power (W)	η_v (%)	T_2 (°C)	P_{sp} (kW/(m^3/min))	η_{ad} (%)
2	2000	0.32	799	54.04	66.73	2.50	51.08
2	3000	0.60	1246	67.82	74.04	2.07	61.63
2	4000	0.88	1734	74.74	79.41	1.96	65.09
3	2000	0.25	1331	43.19	77.46	5.22	41.24
3	3000	0.53	2011	60.21	88.99	3.77	57.08
3	4000	0.81	2723	68.72	97.37	3.35	64.16

5.2 Parametric Study

Confidence in the developed geometry and integrated one-dimensional chamber model, established through comparison with higher-fidelity CFD simulations, motivates a parametric study to assess the influence of key geometric parameters on performance. The aim of this study is to identify internally geared screw machine configurations comparable with the V60 screw compressor (one of the smallest commercially available twin screw machines) in air-compression applications.

Profile shapes in this study follow the circular pin–generation method, parametrised by the non-dimensional pair $(\lambda, \bar{\sigma})$ as described in Section 4.1.1. The explored configuration ranges are listed in Table 5.7. The main rotor wrap angle is fixed at $\Phi_1 = 300^\circ$ to match the V60 main rotor wrap angle, and a total of 1,600 configurations are evaluated.

Table 5.7: Parameter ranges used in the parametric study, defining the 1,600 observed internally geared screw machine configurations.

Parameter	**Symbol**	**Range / value**
Non-dimensional profile parameter	λ	1.1 to 11
Non-dimensional profile parameter	$\bar{\sigma}$	0.10 to 0.99
Gate rotor length-to-diameter ratio	L_2/D_2	0.5 to 5
Main rotor lobe count	N_1	2, 3, 4, 5
Main rotor wrap angle	Φ_1	300° (fixed)

To ensure a fair comparison between the two machine types, the parametric study imposes the displacement (swept) volume of $V_{sw} \approx 0.150\ \ell/rev$, matching the volume displacement of the V60 twin screw design across all configurations. For each parameter combination in Table 5.7, the normalised swept volume in Equation (5.1) is evaluated as a function of the main rotor lobe count and the pin-generation profile parameters, using the reference case $L_2^{\text{ref}} = 1$ and $D_2^{\text{ref}} = 1$. This normalised quantity represents the fraction (percentage) of the outer enveloping cylinder volume.

$$\bar{V}_{sw}(N_1, \lambda, \bar{\sigma}) = \frac{V_{sw}(N_1, \lambda, \bar{\sigma})}{L_2^{\text{ref}}(D_2^{\text{ref}})^2} \tag{5.1}$$

For any configuration in this parametric study, once the profile parameters and the gate rotor length-to-diameter ratio L_2/D_2 are defined, the gate rotor diameter D_2 required to match the target displacement volume is obtained from the normalised swept volume, as defined in Equation (5.2).

$$D_2 = \sqrt[3]{\frac{V_{sw}^{target}(N_1, \lambda, \bar{\sigma})}{\bar{V}_{sw}(N_1, \lambda, \bar{\sigma})\frac{L_2}{D_2}}} \tag{5.2}$$

The built in volume ratio is fixed at $VI = 4$ for all configurations, matching the volume index of the V60 twin screw compressor, and the clearance gaps are fixed and set equal to those of the V60 configuration. Speed limitations were assessed using the SKF guidance on rolling bearing operating temperature and speed limitations [70], which indicates that the allowable speed is governed by heat generation, lubrication conditions, bearing design and thermal balance. Based on this guidance, a rough assessment suggested that, for the bearing sizes expected in this machine class, a practical upper operating range for the gate rotor bearing corresponds to approximately 25–30 m/s tip speed. Therefore, the gate rotor tip speed was fixed at $v_2 = 25$ m/s for all configurations.

In future design, a more detailed bearing selection study should be carried out to confirm the allowable speed for the final bearing arrangement. The results of the parametric study are shown in Figure 5.3, where adiabatic and volumetric efficiencies are reported for each configuration. The configurations are grouped by the main rotor lobe count, with profile shape parameters and overall size varied through the profile diameters and rotor length.

From Figure 5.3, performance trends indicate that lower lobe counts yield higher adiabatic and volumetric efficiencies. Within the evaluated set, the highest efficiencies occur for $N_1 = 2$. Moreover, the magnified region around the maxima reveals a clear efficiency frontier formed by three leading points, all arising from configurations with $N_1 = 2$. The complete machine specifications, together with the predicted volumetric efficiency η_v and adiabatic efficiency η_a, are listed in Table 5.8. The corresponding profile shapes, plotted to a common scale for all three cases, are shown in Figure 5.4.

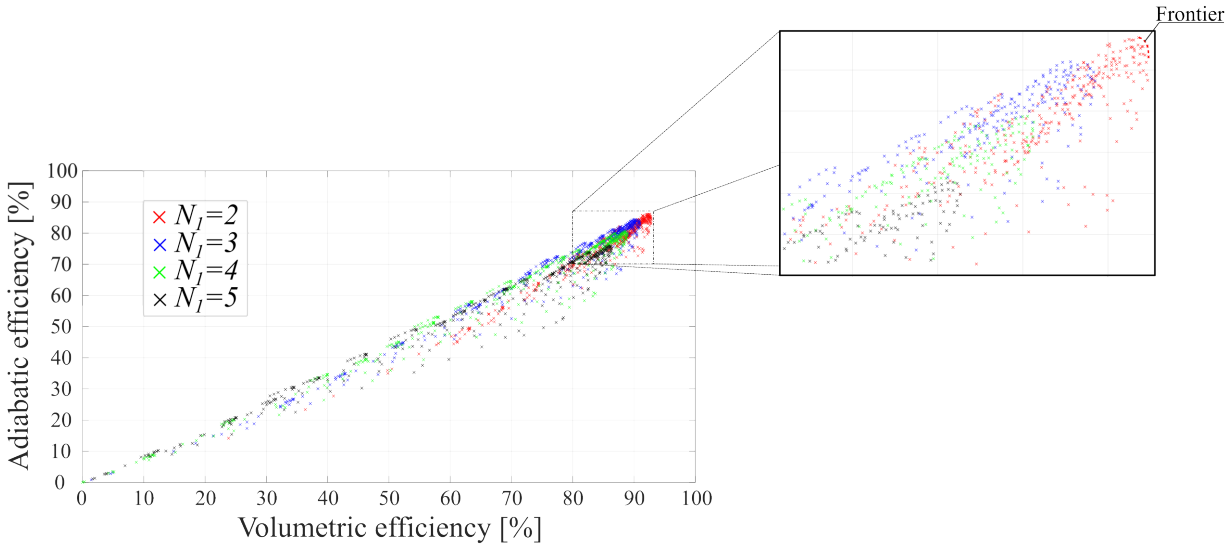

Figure 5.3: Parametric study of adiabatic and volumetric efficiencies grouped by main rotor lobe count; the efficiency frontier is formed by three configurations with $N_1 = 2$.

Table 5.8: Configurations and predicted performance of the three frontier cases identified in the parametric study.

FRONTIER										
Name	η_a [%]	η_v [%]	λ	$\bar{\sigma}$	N_1	L_2/D_2	E [mm]	L_2 [mm]	D_2 [mm]	D_1 [mm]
IG52	86.09	92.45	1.32	0.77	2	1.75	8.30	120.40	68.78	52.18
IG55	85.21	92.66	1.10	0.77	2	1.50	8.30	108.10	71.89	55.30
IG60	84.34	92.79	1.10	0.55	2	1.25	8.30	96.40	77.00	60.40

To isolate the effect of length-to-diameter ratio on performance, Figure 5.5 reports the efficiencies for the frontier configurations identified in Figure 5.3 and Table 5.8, holding the profile shape parameters fixed while varying the gate rotor length-to-diameter ratio L_2/D_2. Across all three frontier profiles, the optimal L_2/D_2 lies between 1.0 and 2.0. Ratios below or above this range yield lower adiabatic and volumetric efficiencies.

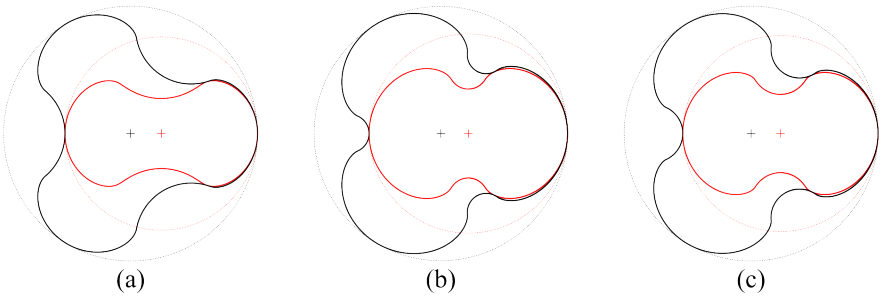

Figure 5.4: Profile shapes for the three frontier cases, shown at a common scale: (a) IG52, (b) IG55, (c) IG60.

To further analyse how geometry parameters influence internally geared screw machine performance, a Pearson correlation matrix [62] is computed. The Pearson product–moment correlation coefficient r quantifies the strength and direction of a linear relationship between two variables X and Y,

$$r = \frac{\mathrm{cov}(X, Y)}{\mathrm{std}(X)\ \mathrm{std}(Y)}, \qquad r \in [-1, 1],$$

with $r = 1$ indicating perfect positive linear association, $r = -1$ perfect negative linear association, and $r = 0$ no linear correlation. Here, $\mathrm{cov}(X, Y)$ is the covariance between X and Y, and $\mathrm{std}(X)$ denotes the standard deviation of X (analogously for Y).

The geometric predictors taken from the parametric study are the main rotor lobe count N_1, the non-dimensional profile parameters $\bar{\sigma}$ and λ, and the outer rotor length–to–diameter ratio L_2/D_2. The performance variables examined are volumetric efficiency η_v, adiabatic efficiency η_a, indicated power P_{ind}, and volumetric flow rate Q (Table 5.9).

The results indicate that λ is negatively correlated with η_v and η_a (about -0.67 to -0.68) and with Q (-0.61), suggesting that larger λ values are associated with lower predicted efficiencies and flow. The lobe count N_1 shows a moderate negative correlation with the same three metrics (≈ -0.44 to -0.54), implying that increasing N_1 tends to reduce efficiency and flow within the sampled space. By contrast, $\bar{\sigma}$ exhibits weak positive correlations with η_v and η_a (≈ 0.21–0.24) and with Q (≈ 0.20), indicating a mild beneficial trend. The ratio L_2/D_2 correlates strongly and positively with P_{ind} (0.70) and moderately with Q (0.42), while its association with efficiencies is weakly positive (≈ 0.12–0.15). Overall, these correlations suggest that, within the studied bounds, lower λ and (to a lesser extent) lower N_1 favour higher efficiencies and flow, whereas increasing L_2/D_2 mainly drives up indicated power. These are linear associations and should be interpreted

as directional guidance rather than causation and they are most useful for narrowing the design space prior to targeted optimisation.

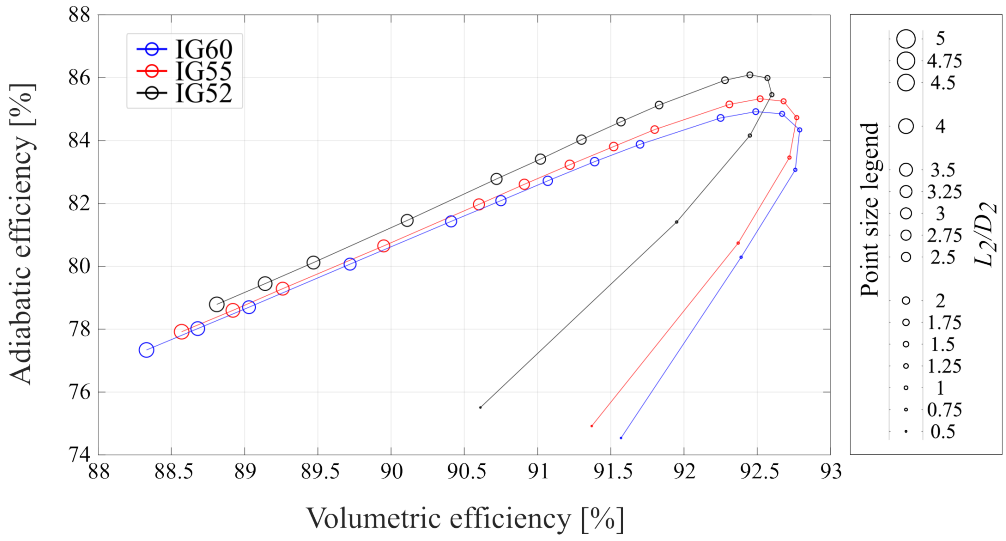

Figure 5.5: Adiabatic vs. volumetric efficiency for the three frontier profile shapes (IG60, IG55, IG52). Marker size encodes the gate rotor length-to-diameter ratio L_2/D_2 (0.5–5.0). Peak performance occurs for $L_2/D_2 \in [1, 2]$.

Table 5.9: Pearson correlation matrix between geometric predictors (main rotor lobe count N_1, profile parameters $\bar{\sigma}$ and λ, and outer rotor length to diameter ratio L_2/D_2) and performance variables (volumetric efficiency η_v, adiabatic efficiency η_a, indicated power P_{ind}, and volumetric flow rate Q).

	N_1	$\bar{\sigma}$	λ	L_2/D_2
η_v	-0.44	0.21	-0.67	0.12
η_a	-0.47	0.24	-0.68	0.15
P_{ind}	-0.48	0.16	-0.40	0.70
Q	-0.54	0.20	-0.61	0.42

5.3 Comparison of Conventional Twin and Internally Geared Screw Compressor

A direct performance comparison between internally geared screw machines and conventional twin screw machines has not previously been reported. Given that internally geared screw machines are intended for the lower size limit of conventional twin screw designs, an appropriate first benchmark is one of the smallest commercially available air compressor in the conventional class. In this section, a design selected from the internally geared screw machine parametric study is compared against the V60 twin screw compressor. The parametric sweep over the chosen input ranges identified three configurations on the efficiency frontier (Table 5.8). Among these configurations, the mid-point case (IG55) is selected for comparison.

Both the V60 twin screw and the IG55 internally geared screw machines are configured to deliver approximately 0.150 ℓ/rev with identical clearance gaps. Table 5.10 summarises the geometries of both machines. The V60 has a slightly larger main rotor diameter, whereas its gate rotor diameter is significantly smaller due to the different rotor arrangement. To achieve the same displacement, the IG55 has a slightly larger rotor length. The overall envelopes, represented in a common scale are shown in Figure 5.6, highlight the resulting differences in size.

Table 5.10: Geometric comparison between the IG55 internally geared screw machine and the V60 twin screw compressor, highlighting key parameters (lobe counts, axis distance, rotor diameters and lengths) used for subsequent performance comparison.

Name	N_1	N_2	E [mm]	D_1 [mm]	D_2 [mm]	L [mm]
IG55	2	3	8.30	55.30	71.89	108.10
V60	4	5	42.00	59.73	47.35	92.58

Performance is assessed for both machines over main rotor speeds of 3000–7500 rpm and discharge pressures of 7, 10, and 13 bar, selected to match benchmarks from the V60 technical catalogue [16]. The predicted performance comparison is shown in Figure 5.7.

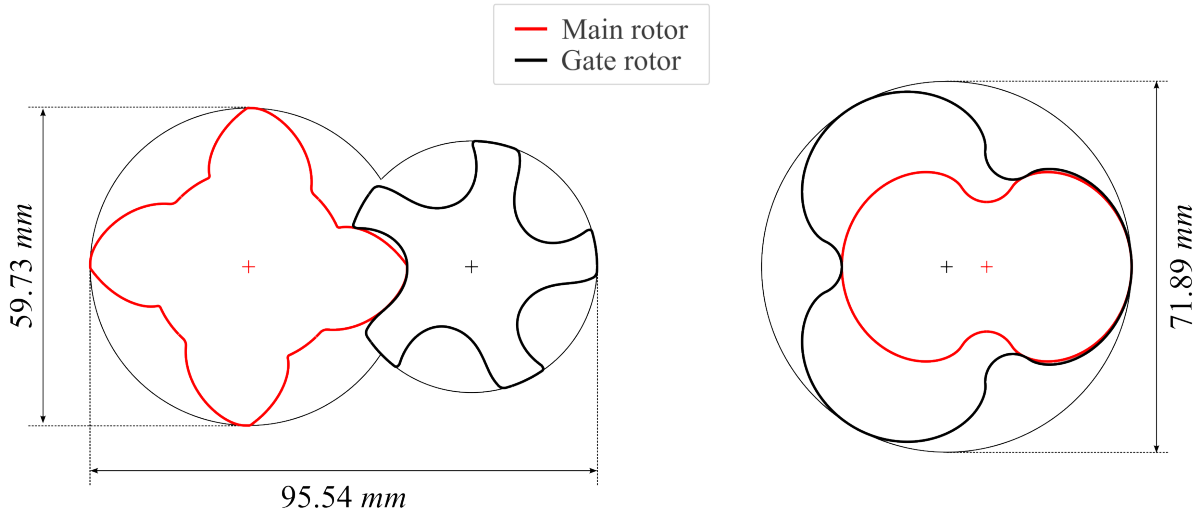

Figure 5.6: Overall envelopes of the V60 twin screw (a) and IG55 internally geared screw machine (b) shown on a common scale, with main and gate rotor profiles and key diameters indicated.

Figure 5.7 (a) presents the predicted volumetric flow rates across the tested shaft speeds and discharge pressures. The flow rate increases approximately linearly with shaft speed, as expected for fixed displacement. For a given speed and discharge pressure, IG55 (solid lines) delivers a slightly higher flow than the V60 (dashed lines). Increasing discharge pressure from 7 to 13 bar shifts the curves downward for both machines, reflecting increased internal leakage and losses that reduce delivered flow. The relative separation between the IG55 and V60 curves remains broadly consistent across the speed range, indicating similar pressure sensitivity of volumetric performance.

Figure 5.7 (b) shows indicated power as a function of delivered flow. For each discharge pressure, power rises approximately linearly with flow, and the slope represents the specific power. At a given flow and pressure, IG55 (solid lines) consistently requires less indicated power than the V60 (dashed lines), indicating lower specific power and therefore better predicted efficiency. Increasing discharge pressure shifts the lines upward for both machines (higher power demand at the same flow), with similar slopes for IG55 and V60, suggesting comparable pressure sensitivity. The power gap between IG55 and V60 is maintained across the operating range and is most pronounced at higher pressures.

Figure 5.7 (c) presents specific power as a function of flow rate. Specific power decreases with increasing flow for all cases, reflecting that fixed losses and leakage constitute a smaller fraction of

the input at higher flow rates. At a given discharge pressure, IG55 (solid lines) exhibits consistently lower specific power than the V60 (dashed lines), indicating a more favourable power–flow trade-off. Raising discharge pressure shifts the curves upward for both machines, with the penalty most pronounced at low flow where leakage and loss effects dominate. The IG55–V60 gap remains across the range and is largest at the highest pressure level, suggesting that IG55 maintains its advantage under more demanding pressure ratios.

Figure 5.7 (d) shows volumetric efficiency as a function of flow rate. Volumetric efficiency increases with flow for all cases and tends to level off near 90% at the highest flow rates, consistent with leakage becoming a smaller fraction of the swept volume. At a given flow and discharge pressure, IG55 (solid lines) attains higher η_v than the V60 (dashed lines). Increasing discharge pressure lowers η_v for both machines, with the penalty most evident at low flow. The separation between IG55 and V60 persists across the range but narrows slightly at high flow where both approach their asymptotic efficiencies.

Figure 5.7 (e) shows adiabatic efficiency as a function of flow rate. Adiabatic efficiency rises with increasing flow and tends to level off around 85–90% at the highest flow rates, indicating that losses become less dominant. At any given flow and discharge pressure, IG55 (solid lines) attains higher η_a than the V60 (dashed lines), consistent with its lower specific power. Raising discharge pressure shifts both machines downward in η_a, with the penalty most evident at low flow. The gap between IG55 and V60 persists across the range but narrows slightly near the high-flow flat region.

Across the examined operating range, IG55 consistently outperforms the V60. For a given speed and discharge pressure, IG55 delivers slightly higher flow, requires lower indicated power at the same flow, and therefore achieves lower specific power and higher efficiencies. Volumetric and adiabatic efficiencies for both machines improve with increasing flow and flatten toward high flow rates. Increasing discharge pressure penalises both machines in flow and efficiency and raises power demand, with the penalty most apparent at low flow where leakage loss effects dominate. The relative separation between IG55 and V60 remains broadly consistent, indicating that IG55 maintains its advantage across speeds and pressures under the matched-displacement, matched-clearance, and fixed $VI = 4$ assumptions. Although these trends suggest that the internally geared screw machine architecture is beneficial at this size scale, the results are not conclusive. A definitive comparison requires controlled experimental measurements once the IGSM test rig is available.

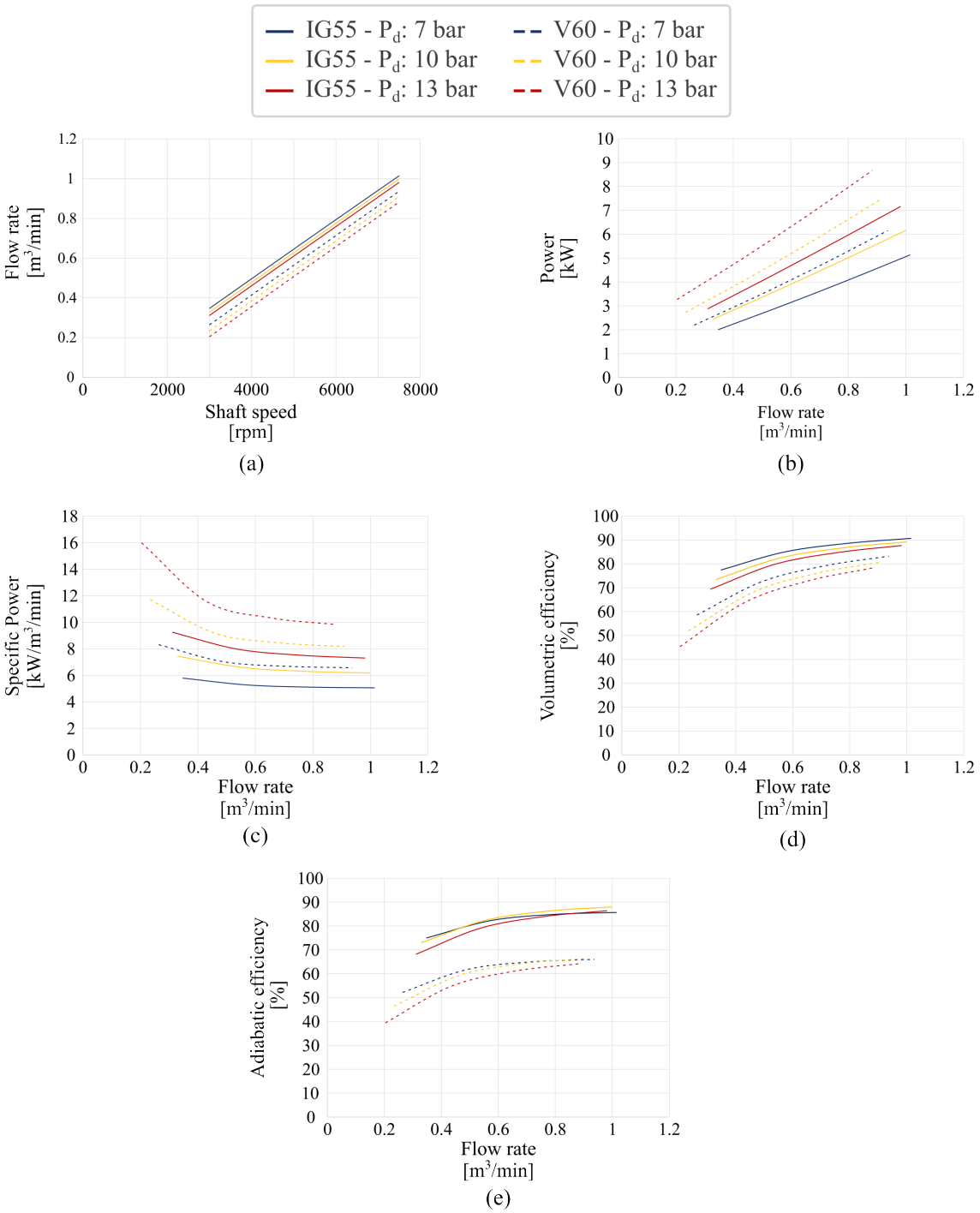

Figure 5.7: Comparison of the IG55 internally geared screw machine and the V60 twin screw compressor across a range of operating shaft speeds and discharge pressures. (a) volumetric flow rate vs shaft speed, (b) indicated power vs flow, (c) specific power vs flow, (d) volumetric efficiency vs flow, and (e) adiabatic efficiency vs flow.

5.4 Outcome

The geometry model developed in Section 4.1 has been integrated with the existing one-dimensional chamber model within the `SCORG` software, developed at City St George's, University of London [9]. In the absence of experimental data, the chamber model was compared against CFD results from recent internally geared screw machine studies for a representative case, providing initial confidence in its suitability for parametric exploration and optimisation.

A parametric study on circular pin–generated profiles, defined by the non-dimensional pair $(\lambda, \bar{\sigma})$ (see Section 4.1.1), indicates that lower λ values tend to yield higher predicted efficiencies, while increasing the main rotor lobe count N_1 generally reduces efficiency within the examined bounds.

From this study, an internally geared screw machine configuration was identified and benchmarked against the V60, a representative small-scale conventional twin screw compressor. Across the observed speeds and discharge pressures, the IGSM delivered higher flow and higher efficiencies, translating into lower power demand and demonstrating promising potential for small-scale air-compression applications.

These findings should be regarded as preliminary. The next priorities are to complete the experimental test rig and obtain measurements to validate the chamber model and verify the proposed design.

6 Advancement of Rotor Profiling Methods for Internally Geared Screw Machines

Previous studies on internally geared screw machines have implemented either pin generated profiles (Section 2.3.3) or profiles constructed from combinations of epicycloid and hypocycloid curves (Section 2.3.2). These shapes are attractive due to the simplicity of their generation, but analytical treatment typically restricts them to circular pins. Since machine performance depends strongly on rotor geometry, which together with other parameters governs displaced volume, leakage paths, contact forces, and related effects, it is well motivated to explore advanced rotor profiling methodologies.

The rack method introduced in Section 2.3.1 has proved effective for conventional twin screw machines and (spur) gears, offering a standard approach in which the rotor shape is defined on a rack, the rotor with infinite radius. However, despite its importance in conventional designs, this method has not been investigated for cases that require continuous contact and a zero minimum working chamber area.

This section presents the fundamental steps for applying the rack method to internally geared rotor profiles, including the conditions that guarantee continuous contact. The implementation is illustrated through several cases, and the general procedure is detailed.

In addition, given the growing use of data driven approaches, particularly methods based on deep neural networks, this study also explores the generation of internally geared screw machine profiles using deep learning.

6.1 Existence of the Continuous Contact

The meshing condition presented in Equation (A.5) can be challenging to solve analytically. However, it can also be effectively addressed through geometrical analysis, as initially described by Buckingham [71]. To enhance the understanding of continuous contact between the rotors, this section presents a detailed geometrical analysis of the meshing condition.

Consider a general lobe curve of the main rotor, as illustrated in Figure 6.1 (a). A representative point C on the main rotor has coordinates $\left(x_1^{S_1}(\theta), y_1^{S_1}(\theta)\right)$ in the rotor's local coordinate system S_1.

The normal at point C can be calculated using the first derivative of the rotor profile curve, and the normal angle, ψ_1, is determined as shown in Equation (6.1). The polar coordinates of the rotor in its local coordinate system are given by Equations (6.2) and (6.3).

$$\psi_1(\theta) = \arctan\left(\frac{-dx_1^{S_1}(\theta)}{dy_1^{S_1}(\theta)}\right) \tag{6.1}$$

$$\varphi_{p_1}(\theta) = \arctan\left(\frac{y_1^{S_1}(\theta)}{x_1^{S_1}(\theta)}\right) \tag{6.2}$$

$$\rho_{p_1}(\theta) = \sqrt{\left(x_1^{S_1}(\theta)\right)^2 + \left(y_1^{S_1}(\theta)\right)^2} \tag{6.3}$$

The first solution of the meshing condition, denoted by the angle $\sigma = \sigma_1$, must be determined. Triangle $\triangle ABC$, illustrated in Figure 6.1 (a), can be isolated and analysed, as shown in Figure 6.1 (b). Using geometric principles, the corresponding angles within $\triangle ABC$ are defined and expressed in Equations (6.4) and (6.5).

$$\varphi_c(\theta) = \psi_1(\theta) - \varphi_{p_1}(\theta) \tag{6.4}$$

$$\gamma(\theta) = \pi - \left(\psi_1(\theta) - \sigma\right) \tag{6.5}$$

By applying the sine rule in triangle $\triangle ABC$ (as shown in Equations (6.6) and (6.7)) and incorporating the relationships defined in Equations (6.4) and (6.5), the angle of the contact point, σ, can be calculated. The first solution for the meshing angle of a rotor point is provided in Equation (6.8).

This solution of the meshing condition corresponds to the one used in the rack method, which lies in the first or fourth quadrant of the coordinate system. The second potential solution, which lies in the second or third quadrant, is shown in Equation (6.9).

$$\frac{\sin\Big(\varphi_c(\theta)\Big)}{r_{1w}} = \frac{\sin\Big(\gamma(\theta)\Big)}{\rho_{p_1}(\theta)} \tag{6.6}$$

$$\gamma(\theta) = \arcsin\left(\frac{\rho_{p_1}(\theta)}{r_{1w}} \cdot \sin\Big(\varphi_c(\theta)\Big)\right) \tag{6.7}$$

$$\sigma(\theta) = \psi_1(\theta) - \gamma(\theta) \tag{6.8}$$

$$\sigma^*(\theta) = \psi_1(\theta) + \gamma(\theta) - \pi \tag{6.9}$$

The meshing angles σ and σ^* alone do not constitute a sufficient condition to ensure continuous contact between the rotors. They provide an analytical means of defining the potential meshing angles at rotor points. However, to maintain continuous contact, the transition between the roots of the meshing equation must be smooth. This requires a transition point P_t at which both solutions coincide.

In other words, at the transition point, $\sigma = \sigma^*$, or equivalently, solving Equations (6.8) and (6.9) indicates that $\gamma = \frac{\pi}{2}$. To ensure continuous contact, the solutions for the angle γ, as described in Equations (6.7), must remain continuous across the entire domain.

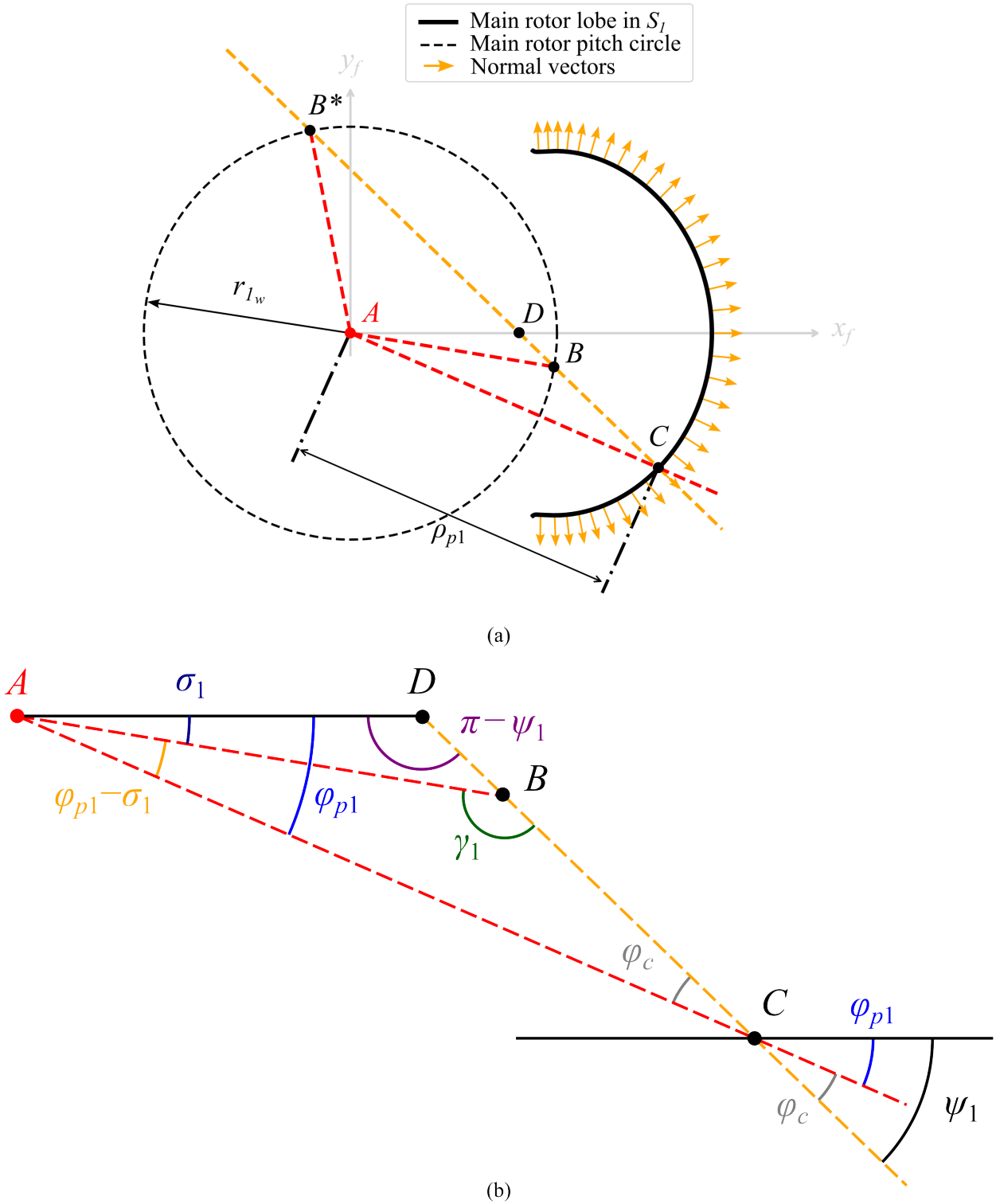

Figure 6.1: Geometrical interpretation of the meshing condition: (a) a single lobe on the main rotor profile, and (b) a close-up view of triangle $\triangle ABC$.

6.2 Rack Method for Internally Geared Rotor Profiles

Conventional twin screw machine rotor profiles are typically generated using the rack method (see Section 2.3.1), which leverages the principles of the Envelope Theory formulated by Euler [38] in the field of differential geometry. This theory allows for the mathematical calculation of the equation of a curve that envelopes a family of curves, making it applicable for generating equations of conjugate shapes on paired rotors. Using the enveloping method, for any given rotor profile, a corresponding conjugate rotor profile depending on it's pitch circle can be found by applying the meshing condition. The rack rotor represents a special case when the pitch circle has "infinite radius". In other words, rack rotor represents straight rotor that is used to envelope main and gate rotor. The shape of the rack can be defined by segments which makes this method very powerful.

Although the rack method has been widely used in conventional twin screw machines, it has never been applied to internally geared screw machines. However, the rack method is commonly used in internal gearing, particularly for generating involute profiles for gears. It is known that the rack method can produce internal gears, but the question remains whether it can produce internal gears that satisfy the necessary conditions for continuous contact between the rotors and a zero-minimum working chamber area, which is essential for efficient compression in internally geared screw machines.

Since the initial rack method described by Stosic [39] does not account for the second root of the meshing equation, as described geometrically in Section 6.1, continuous contact cannot be guaranteed. An initial investigation conducted by Lacevic et al. [72] incorporated a combination of cycloid and inverted cycloid curves on the rack, resulting in fully valid internally geared rotor profiles that ensure both continuous contact and a zero-minimum working chamber area.

However, the rack described in this initial investigation most likely represents a special case due to the inherent properties of cycloidal curves. This study presents an extended approach using the rack method to generate one rotor, which can then be used to derive the corresponding rotor. A special case, where the rack is based on a trochoidal curve and the meshing condition is solved analytically, is described alongside the general approach for generating valid internally geared rotors, with or without a zero-minimum working chamber area.

6.2.1 Analytical Solution for Cycloid Racks

Inspired by the shapes generated through combinations of epi and hypo cycloidal curves (Section 2.3.2), the initial stage of this research focused on generating rack rotor profiles based on the same geometries.

A cycloid is a parametric curve traced by a point on the circumference of a circle of radius r_c as it rolls without slipping along a straight line. The general parametric form of a cycloid is expressed in Equation (6.10), where θ denotes the angular rotation of the generating circle and serves as a curve parameter.

$$x_c(\theta) = r_c\,(\theta - \sin\theta)\,, \qquad y_c(\theta) = r_c\,(1 - \cos\theta)\,, \tag{6.10}$$

The geometric dimensions of the cycloid are governed by the radius of the generating circle r_c as shown in Figure 6.2. The *height* h_c of one cycloidal arch, corresponding to the maximum vertical displacement, is given by

$$h_c = 2r_c, \tag{6.11}$$

while the *width* w_c, corresponding to the horizontal distance covered in one complete rotation of the circle, is given by

$$w_c = 2\pi r_c. \tag{6.12}$$

As shown in Equations (6.11) and (6.12), both the height and the width of the cycloid period scale linearly with the radius of the generating circle.

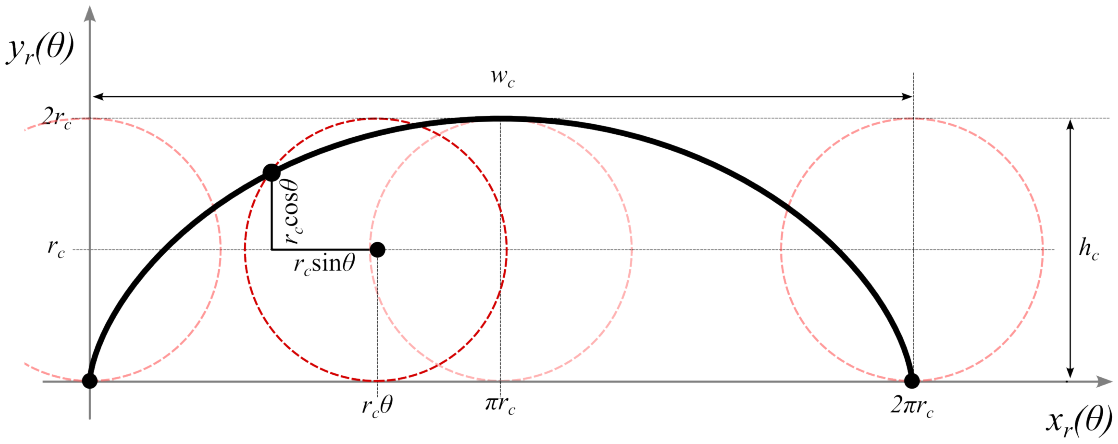

Figure 6.2: Geometry of a single cycloid arch generated by a circle of radius r_c rolling without slip along the x axis. The construction shows the parametric coordinates $x_c(\theta)$ and $y_c(\theta)$, the pitch $w_c = 2\pi r_c$, and the height $h_c = 2r_c$. Faint circles indicate successive positions of the rolling circle, and the points $r_c\cos\theta$ and $r_c\sin\theta$ mark the projection of the generating point.

In the context of rack rotor generation for internally geared screw machines, the rack profile can be defined by combining two distinct cycloidal segments: one generated by a circle of radius $r_c^{(a)}$ for the addendum portion, and another generated by a circle of radius $r_c^{(d)}$ for the dedendum portion. The dedendum cycloid is geometrically inverted relative to the addendum cycloid to form the lower part of the rack profile. The combination of these two curves produces a single continuous waveform that serves as the basis for the rack rotor geometry.

To produce a valid rack rotor profile from such a combination, several geometric and meshing conditions must be satisfied. Firstly, to ensure geometric continuity, the radii of the addendum and dedendum generating circles must satisfy

$$r_c^{(a)} + r_c^{(d)} = E, \tag{6.13}$$

where E is the axis distance between the main and gate rotors. The total vertical height of the combined cycloid is therefore equal to $2E$, as implied by Equation (6.11). When the condition given by Equation (6.13) is fulfilled and the addendum and dedendum cycloids are combined to guarantee C^1 continuity, the resulting rack rotor profile can be used to generate the conjugate main and gate rotor profiles.

For a more convenient design of the rack rotor profile using cycloidal curves, the pitch circle radius of the main rotor can first be defined as r_{1w}, with the number of lobes on the main rotor denoted as N_1. The corresponding gate rotor parameters are then obtained from the internally geared configuration as

$$N_2 = N_1 + 1, \qquad r_{2w} = \frac{N_2}{N_1}\, r_{1w},$$

and the axis distance is therefore

$$E = r_{2w} - r_{1w}.$$

Since the radii of the generating circles must satisfy the geometric constraint in Equation (6.13), the radius of the addendum generating circle can be conveniently expressed as

$$r_c^{(a)} = E\,\bar{\lambda}_c,$$

where $\bar{\lambda}_c \in (0,1)$ represents the fractional contribution of the addendum section within a single lobe on the rack rotor profile. The corresponding dedendum generating circle radius then follows as

$$r_c^{(d)} = E - r_c^{(a)} = E\,(1 - \bar{\lambda}_c).$$

This parametrisation allows flexible shaping of the rack profile by adjusting $\bar{\lambda}_c$ while maintaining geometric validity across the addendum and dedendum regions. To ensure continuous and periodic cycloidal motion for any chosen addendum fraction $\bar{\lambda}_c \in (0,1)$, the angular period of the combined cycloid curve is defined as

$$T = 4\pi,$$

where T represents the full period of one addendum and one dedendum cycle. A single period in the physical domain, corresponding to the total advancement of the curve in the x-direction, is given by

$$\Delta x = 2\pi \left(r_c^{(a)} + r_c^{(d)} \right) = 2\pi E. \tag{6.14}$$

For any angular parameter $\theta \in \mathbb{R}$, the in-period phase τ and the integer period index n are defined as

$$\tau = \theta - nT, \qquad n = \left\lfloor \frac{\theta}{T} \right\rfloor, \tag{6.15}$$

where $\tau \in [0, T)$ describes the angular phase within the present period, and n indicates how many full periods have elapsed.

The angular boundary separating the addendum and dedendum regions is given by

$$\tau_a = \bar{\lambda_c} T, \qquad \tau_d = T - \tau_a.$$

The local phase angles are re-parametrised to always span the interval $[0, 2\pi]$ as

$$u = 2\pi \frac{\tau}{\tau_a}, \qquad v = 2\pi \frac{\tau - \tau_a}{\tau_d}.$$

The base (single lobe) parametric curve $\Big(x_r(\tau),\, y_r(\tau)\Big)$ in the local coordinate system of the rack rotor, S_r, is given in Equation (6.16).

$$\begin{aligned} x_r^{S_r}(\tau) &= \begin{cases} r_c^{(a)} \left(u - \sin u\right), & 0 \le \tau < \tau_a, \\ 2\pi r_c^{(a)} + r_c^{(d)} \left(v - \sin v\right), & \tau_a \le \tau < T, \end{cases} \\ y_r^{S_r}(\tau) &= \begin{cases} r_c^{(a)} \left(1 - \cos u\right), & 0 \le \tau < \tau_a, \\ r_c^{(d)} \left(-1 + \cos v\right), & \tau_a \le \tau < T \end{cases} \end{aligned} \tag{6.16}$$

To extend the curve periodically in the local coordinate system of the rack rotor, S_r, when $|\theta| > T/2$, the total curve is defined as

$$x_p^{S_r}(\theta) = x_b^{S_r}(\tau) + n\,\Delta x, \qquad y_p^{S_r}(\theta) = y_b^{S_r}(\tau), \tag{6.17}$$

where Δx is defined in Equation (6.14). This formulation ensures that the curve is continuous across all periods in θ, regardless of the addendum fraction $\bar{\lambda_c}$.

The parametric derivatives of $x_r(\tau)$ and $y_r(\tau)$ with respect to τ are obtained analytically from Equation (6.16) and given in Equation (6.18).

$$\begin{aligned} \frac{dx_r}{d\tau}(\tau) &= \begin{cases} \dfrac{2\pi r_c^{(a)}}{\tau_a} \left(1 - \cos u\right), & 0 \le \tau < \tau_a, \\ \dfrac{2\pi r_c^{(d)}}{\tau_d} \left(1 - \cos v\right), & \tau_a \le \tau < T, \end{cases} \\ \frac{dy_r}{d\tau}(\tau) &= \begin{cases} \dfrac{2\pi r_c^{(a)}}{\tau_a} \sin u, & 0 \le \tau < \tau_a, \\ -\dfrac{2\pi r_c^{(d)}}{\tau_d} \sin v, & \tau_a \le \tau < T \end{cases} \end{aligned} \tag{6.18}$$

At the interface between the addendum and dedendum regions, where $\tau = \tau_a$, continuity of both position and slope is satisfied:

$$
\begin{aligned}
x_r(\tau_a^-) &= x_r(\tau_a^+) = 2\pi r_c^{(a)}, \\
y_r(\tau_a^-) &= y_r(\tau_a^+) = 0, \\
\left.\frac{dx_r}{d\tau}\right|_{\tau_a^-} &= \left.\frac{dx_r}{d\tau}\right|_{\tau_a^+} = 0, \\
\left.\frac{dy_r}{d\tau}\right|_{\tau_a^-} &= \left.\frac{dy_r}{d\tau}\right|_{\tau_a^+} = 0.
\end{aligned}
$$

Thus, the cycloidal combination defined by Equation (6.17) is both positionally and tangentially continuous (C^1) for any value of $\bar{\lambda_c} \in (0, 1)$, ensuring a smooth transition between the addendum and dedendum portions.

Examples of rack rotor profiles generated in the local coordinate system of the rack rotor using the combination of cycloidal curves described above are shown in Figure 6.3.

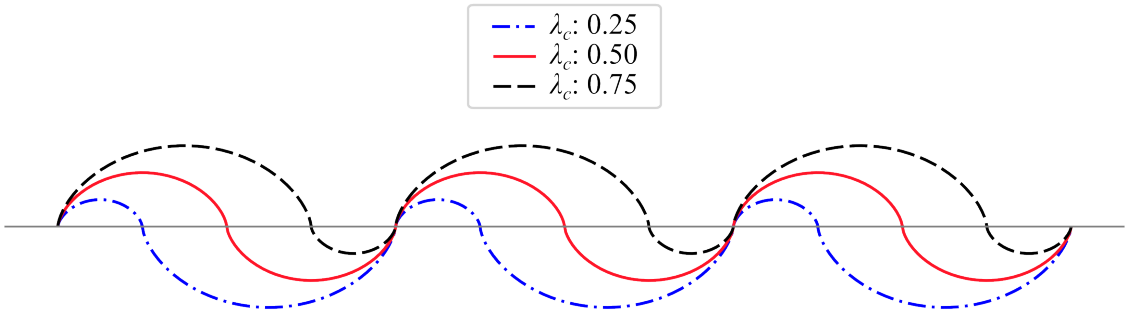

Figure 6.3: Examples of cycloid rack curves in their local coordinate system, generated from the parametric equations in Equation (6.17).

The local coordinates of the rack profile are transformed into the global coordinate system S_f by applying the transformation matrix $\mathbf{M}_{rf}$ (Equation (6.19)) as shown in Equation (6.20). A single lobe of the rack profile is generated for $\theta \in [0, 4\pi]$, where θ serves as the general profile curve parameter.

$$\mathbf{M}_{rf} = \begin{bmatrix} 1 & 1 & 0 & r_{1w} \\ -1 & 1 & 0 & 0 \\ 0 & 0 & 1 & 0 \\ 0 & 0 & 0 & 1 \end{bmatrix} \tag{6.19}$$

$$\begin{bmatrix} x_r^{S_f}(\theta) & y_r^{S_f}(\theta) & 0 & 1 \end{bmatrix}^\top = \mathbf{M}_{rf} \begin{bmatrix} x_r^{S_r}(\theta) & y_r^{S_r}(\theta) & 0 & 1 \end{bmatrix}^\top \tag{6.20}$$

The main and gate rotor profiles in the internally geared configuration can then be derived from the rack rotor profile, expressed in the global coordinate system, by determining the first root of the meshing condition using Equations (2.6) and (2.7), and subsequently applying the coordinate transformations defined in Equations (2.3) and (2.5), respectively.

An example of valid rotor profiles with $N_1 = 4$ and $N_2 = 5$ generated using a cycloid-based rack curve with $\bar{\lambda_c} = [0.25, 0.75]$ is shown in Figure 6.4. This figure demonstrates that conjugate profiles have been successfully produced using the rack method and that the necessary conditions for achieving continuous contact between the rotors and maintaining a zero-minimum working chamber area are satisfied. The locations of the contact points can be determined from the first root of the meshing condition given by Equation (2.6), while the second root can be obtained from the geometrical solution defined in Equation (6.9). From Figure 6.4, it can be observed that the locations of the contact points form a continuous path, illustrating the maintained continuous contact between the main and gate rotors.

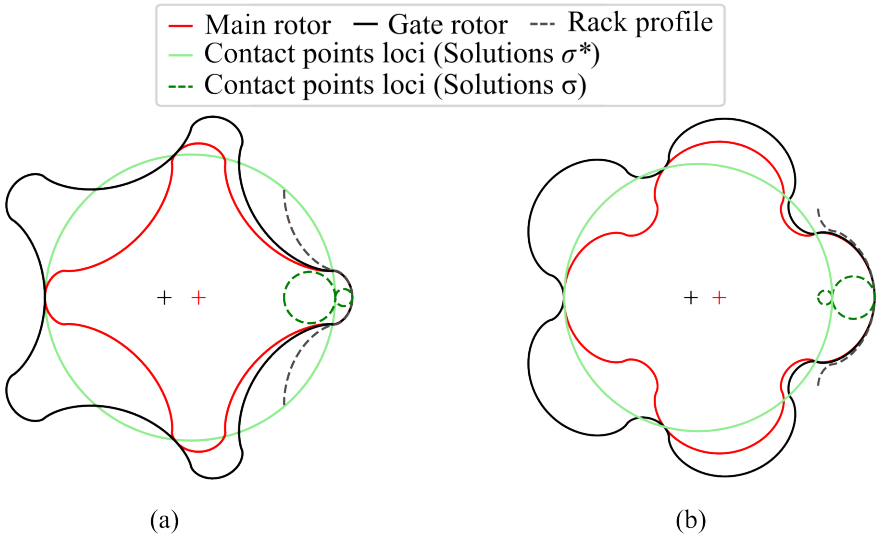

Figure 6.4: Examples of valid rotor profiles generated using a cycloid based rack curve for $N_1 = 4$ and $N_2 = 5$ with (a) $\lambda_c = 0.25$ and (b) $\lambda_c = 0.75$.

6.2.2 Analytical Solution for Trochoidal Racks

A cycloid curve can be expressed as a special case of a more general family of curves known as *trochoids*. A trochoid is defined as the locus of a point attached to a circle as it rolls without slipping along a straight line. Depending on the position of the tracing point relative to the rolling circle, three types of trochoid curves can be distinguished:

(i) If the tracing point lies on the circumference of the rolling circle, the curve is a *cycloid*.

(ii) If the tracing point lies inside the rolling circle, the curve is a *curtate trochoid*.

(iii) If the tracing point lies outside the rolling circle, the curve is a *prolate trochoid*.

Similar to cycloidal curves, trochoid curves are frequently used in engineering applications, particularly in rotor profile design, due to their smooth, periodic, and geometrically well-defined shapes.

Since the rack method based on cycloid curves has been shown to generate valid rotor profiles for internally geared screw machines, it is valuable to extend this approach to more general trochoidal forms. Given that the cycloid represents a specific case of the trochoid, analysing trochoid-based rack generation provides a broader understanding of the limitations and adaptability of the rack method for internally geared rotor design.

The general form of a trochoid is given in Equation (6.21), where a_t and b_t are the parameters defining the geometry of the curve. Here, a_t denotes the radius of the rolling circle, b_t specifies the offset distance of the tracing point from the circle's centre, and θ is the angular parameter describing the rotation of the rolling circle, corresponding to the curve parameter.

$$\begin{aligned} x_t(\theta) &= a_t\theta - b_t \sin\theta, \\ y_t(\theta) &= a_t - b_t \cos\theta \end{aligned} \tag{6.21}$$

The relationship between a_t and b_t defines the specific type of trochoid curve:

(i) $b_t = a_t$: cycloid (the tracing point lies on the rolling circle),

(ii) $b_t < a_t$: curtate trochoid (the tracing point lies inside the rolling circle),

(iii) $b_t > a_t$: prolate trochoid (the tracing point lies outside the rolling circle).

The width of a single period and height of a trochoid are defined respectively as

$$w_t = 2\pi a_t, \qquad h_t = 2b_t.$$

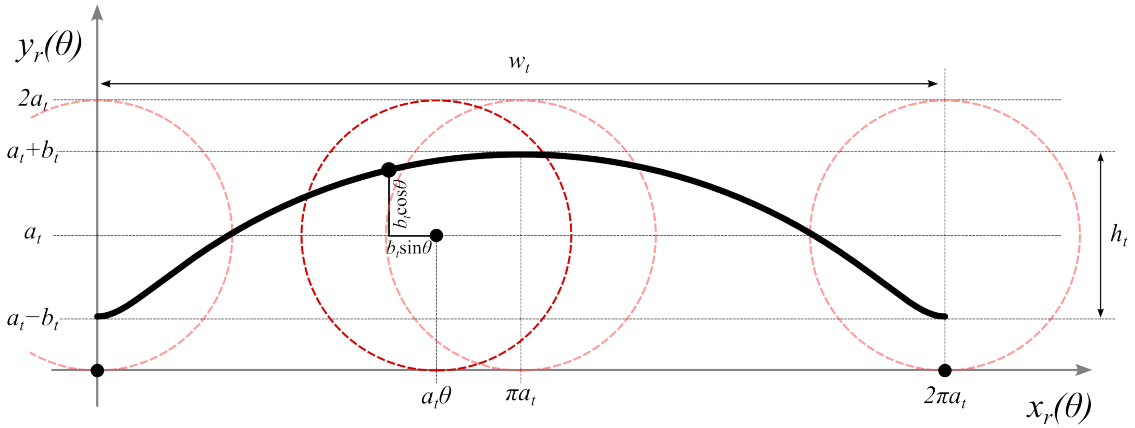

Figure 6.5: Geometry of a single trochoid arch generated by a circle of radius a_t rolling without slip along the x axis, with a generating point offset b_t from the circle centre. The construction shows the parametric coordinates $x_t(\theta)$ and $y_t(\theta)$, the pitch $w_t = 2\pi a_t$, and the height $h_t = 2b_t$. Faint circles indicate successive positions of the rolling circle, and the points $a_t\cos\theta$ and $a_t\sin\theta$ mark the projection of the point inside the circle.

The coordinates of the rack rotor profile, derived from the trochoid curve, in its local coordinate system are defined in Equations (6.22) and (6.23), where $b_t = a_t/\lambda_t$, k_t is an adjustable shape parameter, and a_t is the radius of the rolling circle, which must satisfy the gearing ratio between the rack and the main rotor as $a_t = r_{1w}N_1$. Here, r_{1w} is the pitch circle radius, and N_1 is the number of lobes of the main rotor.

The non-dimensional parameter λ_t characterises the type of trochoid curve, with this study focusing on curtate trochoid curves that satisfy the condition $\lambda_t > 1$ to ensure physically valid rack profiles. The corresponding analytical derivatives of the rack curve are given in Equations (6.24) and (6.25), confirming that the profile is continuously differentiable over its entire domain.

Examples of rack profiles generated by trochoid curves for different values of λ_t with $k_t = 0$ are illustrated in Figure 6.6. The local coordinates of the rack profile are transformed into the global coordinate system S_f by applying the transformation matrix $\mathbf{M}_{rf}$ (Equation (6.19)) as shown in Equation (6.20). A single lobe of the rack profile is generated for $\theta \in [0, 2\pi]$, where θ serves as the general profile curve parameter.

$$x_r^{S_r}(\theta) = a_t\theta - (a_t/\lambda_t)\sin\theta \tag{6.22}$$

$$y_r^{S_r}(\theta) = a_t - \frac{a_t}{\lambda_t}\cos\theta + k_t \tag{6.23}$$

$$\frac{dx_r^{S_r}}{d\theta}(\theta) = a_t - \frac{a_t}{\lambda_t}\cos\theta \tag{6.24}$$

$$\frac{dy_r^{S_r}}{d\theta}(\theta) = \frac{a_t}{\lambda_t}\sin\theta \tag{6.25}$$

The coordinates of the rack generated main (inner) rotor can be derived from the rack profile by combining the global rack coordinates, obtained from Equation (6.20), with the solutions to the meshing condition between the rack profile and the main rotor profile, as described by Stosic [39] and given in Equation (2.7). This relationship can be expressed and solved in matrix form, as shown in Equation (6.26), where the matrix $\mathbf{M}_{r1}(\sigma_{r_1})$ defines the transformation from the rack coordinate system to the main rotor's local coordinate system, as presented in Equation (2.3).

$$\begin{bmatrix} x_1^{S_1}(\theta, \sigma_{r_1}) & y_1^{S_1}(\theta, \sigma_{r_1}) & 0 & 1 \end{bmatrix}^\top = \mathbf{M}_{r1}(\sigma_{r_1})\mathbf{M}_{rf} \begin{bmatrix} x_r^{S_r}(\theta) & y_r^{S_r}(\theta) & 0 & 1 \end{bmatrix}^\top \tag{6.26}$$

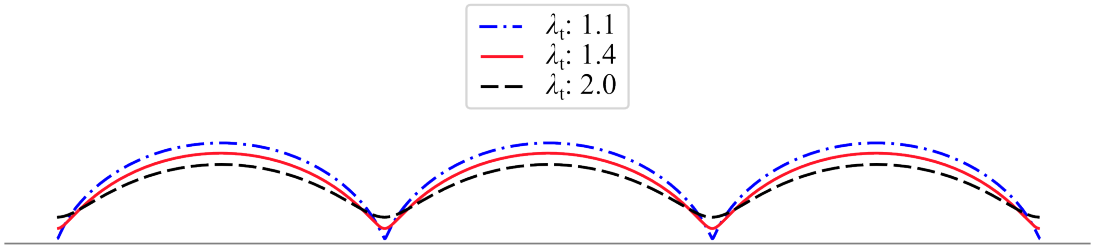

Figure 6.6: Rack profiles generated from a trochoid curve with $k_t = 0$ and $\lambda_t \in \{1.1, 1.4, 2.0\}$.

The coordinates of the rack generated internally geared gate (outer) rotor as described in the rack method can be derived from the rack profile by combining the global rack coordinates, obtained from Equation (6.20), with the solutions to the meshing condition between the rack profile and the gate rotor profile obtained from Equation (2.7). The relationship can be expressed and solved in matrix form, as shown in Equation (6.27), where $\mathbf{M}_{r2}^{(I)}(\sigma_{r_2})$ defines the transformation from the rack coordinate system to the internally geared gate rotor's local coordinate system, as presented in Equation (2.5).

$$\begin{bmatrix} x_2^{S_2}(\theta, \sigma_{r_2}) & y_2^{S_2}(\theta, \sigma_{r_2}) & 0 & 1 \end{bmatrix}^\top = \mathbf{M}_{r2}^{(I)}(\sigma_{r_2}) \begin{bmatrix} x_r^{S_f}(\theta) & y_r^{S_f}(\theta) & 0 & 1 \end{bmatrix}^\top 0 \tag{6.27}$$

An example of a pair of internally geared main and gate rotors generated from the same trochoid-based rack is shown in Figure 6.7. Although this approach produces two rotors that mesh correctly around the pitch point, the resulting profiles are not suitable for internally geared screw compressor applications due to the lack of continuous contact along the profile. This outcome highlights the cycloid rack as a special and valid case, attributed to the distinctive geometric properties of the cycloid curve, such as its constant curvature and concavity, which ensure continuous contact throughout the meshing cycle.

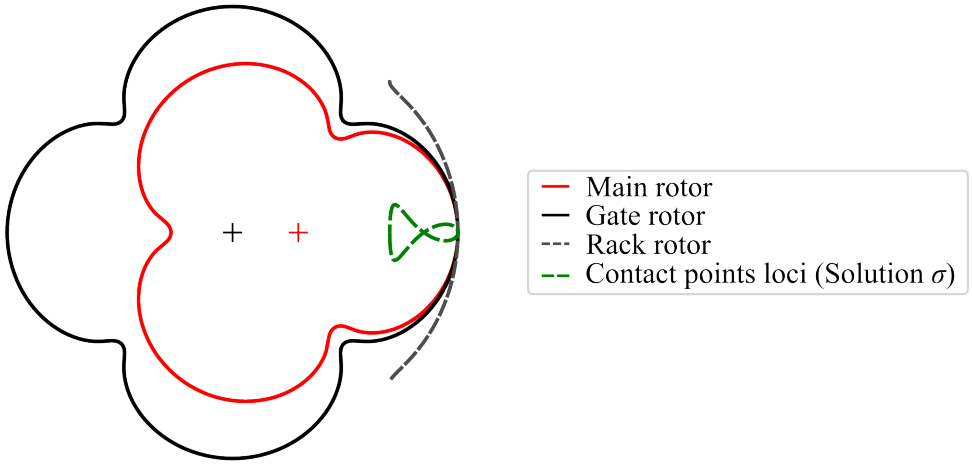

Figure 6.7: Example of invalid internally geared screw machine rotor profiles derived from a single trochoid based rack. These profiles do not satisfy the continuous contact condition.

The rack method, in its conventional form, considers contact points only in the first and fourth quadrants, corresponding to the first root of the meshing condition. While this approach ensures valid contact around the pitch point, it does not guarantee continuous engagement between the main and gate rotors along the entire rotation. Therefore, additional analysis is required to identify and satisfy the conditions necessary for maintaining uninterrupted contact between the rotors throughout the meshing cycle.

The main rotor profile can still be derived directly from the rack profile using Equation (6.26). However, since the gate (outer) rotor in the trochoid-based approach does not necessarily maintain contact with the same rack profile, it becomes essential to determine the correct gearing ratio in terms of the axis distance E between the rack-generated main rotor and its corresponding gate rotor that satisfies the continuous contact requirement. The meshing condition for the generated main rotor profile can thus be formulated using Equation (6.28), which provides the basis for identifying the continuous contact solution.

The transition point $P_t^{S_1} = \left(x_1^{S_1}(\theta_t), y_1^{S_1}(\theta_t)\right)$, introduced in Section 6.1, can be identified in the main rotor's local coordinate system S_1 at the maximum of the function $\gamma(\theta)$, as defined in Equations (6.29) and (6.30).

$$\gamma(\theta) = \arcsin\left(\frac{\rho_{p_1}(\theta)}{N_1 E}\sin\Big(\varphi_c(\theta)\Big)\right) \tag{6.28}$$

$$0 = \frac{d\gamma(\theta)}{d\theta}(\theta_t) \tag{6.29}$$

$$0 = \rho_{p_1}(\theta_t)\frac{d\varphi_c(\theta)}{d\theta}(\theta_t)\cos\Big(\varphi_c(\theta_t)\Big) + \sin\Big(\varphi_c(\theta_t)\Big)\frac{d\rho_{p_1}(\theta)}{d\theta}(\theta_t) \tag{6.30}$$

The corresponding axis distance E required to achieve continuous contact between the rotors can be determined with respect to the identified transition point $P_t^{S_1}$ using Equation (6.31). The axis distance between the main rotor, generated by a trochoid rack, and the corresponding gate rotor that ensures continuous contact is directly related to the trochoid parameter b_t, given as $E = b_t = a_t/\lambda_t$.

$$E = \left|\frac{\rho_{p_1}(\theta_t)\sin\Big(\varphi_c(\theta_t)\Big)}{N_1}\right| \tag{6.31}$$

The axis distance (E) between the main rotor, generated by the trochoid-based rack profile, and the meshing gate rotor can be used to calculate the pitch circle radii of the rotors as $r_{1w} = N_1 E$ and $r_{2w} = N_2 E$, where $N_2 = N_1 + 1$. Additionally, both solutions to the meshing condition can be determined using Equations (6.8), (6.9), and (6.28).

By applying the transformation between the main and gate rotor's local coordinate systems, as given in Equation (B.6), along with the solutions to the meshing condition, the gate rotor profile can be derived as defined in Equation (6.32). The meshing condition can be established for each point on the main rotor profile based on the profile parameter θ.

$$\begin{bmatrix} x_{r_2}^{(2)}(\theta,\sigma) & y_{r_2}^{(2)}(\theta,\sigma) & 0 & 1 \end{bmatrix}^\top = \mathbf{M}_{12}^{(I)}(\sigma)\begin{bmatrix} x_{r_1}^{(1)}(\theta) & y_{r_1}^{(1)}(\theta) & 0 & 1 \end{bmatrix}^\top \tag{6.32}$$

For $\theta_t \leq \theta \leq 2\pi - \theta_t$ (defined here as the addendum section), the main rotor profile coordinates $\Big(x_1^{S_1}(\theta), y_1^{S_1}(\theta)\Big)$ will have two solutions to the meshing condition (Equations (6.8) and (6.9)), representing contact points in all four quadrants. For other points on the main rotor profile (defined here as the dedendum section), only the first solution, defined by Equation (6.8), will exist.

The locations of the contact points in the global coordinate system S_f can be determined by transforming them from the main rotor's local coordinate system using the transformation matrix given in Equation (B.3). Examples of valid internally geared rotors with continuous contact, where main rotor profile is generated using the rack method and gate rotor profile is derived from the main rotor profile are shown in Figure 6.8.

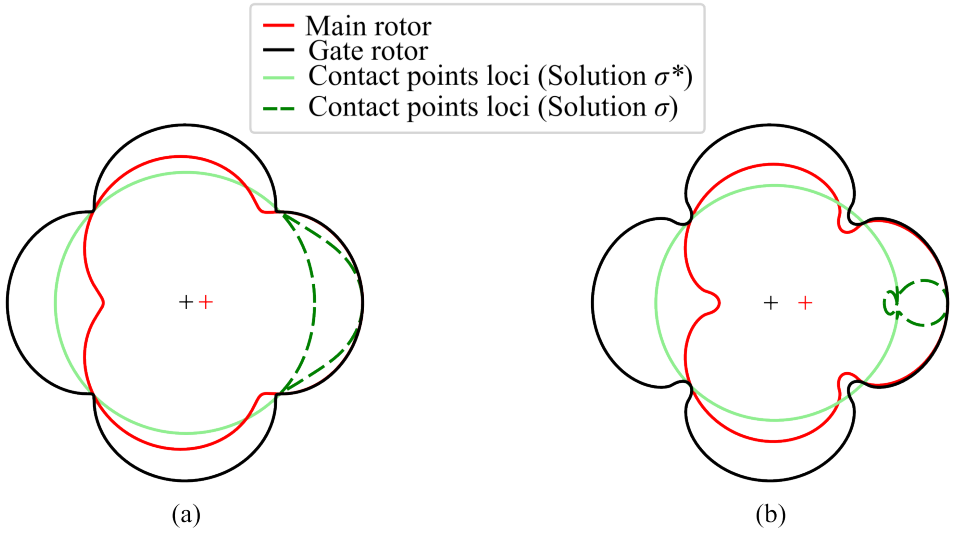

Figure 6.8: Examples of internally geared rotor profiles with (a) $\lambda_t = 1.2$, $k_t = -0.5$ and (b) $\lambda_t = 1.2$, $k_t = 1$, where the main rotor profile is generated using a trochoid-based rack, and the gate rotor is derived from the corresponding main rotor profile ($N_1 = 3$, $N_2 = 4$).

6.2.3 Numerical Solution for General Rack Curves

A general rack curve can be defined in its local coordinate system as $x_r^{(S_r)}(\theta), y_r^{S_r}(\theta)$, where θ is the general profile curve parameter. Using the rack method to generate one rotor and subsequently deriving the second rotor while ensuring that the geometrical meshing condition is satisfied provides a suitable approach for generating valid rotor profiles with continuous contact. The width of a single lobe on the rack must satisfy the gearing ratio $w_{rack} = \frac{2\pi}{N_1} r_{1w} = \frac{2\pi}{N_2} r_{2w}$.

In Section 6.2.2, the generation of the main (inner) rotor using the rack profile was described, and an analytical solution for the trochoidal rack was provided. The gate rotor was then derived from the main rotor. To emphasise the feasibility of this approach, this section describes the procedure for generating the gate (outer) rotor using the general rack profile and deriving the meshing main rotor with continuous contact.

The rack coordinates can be expressed in the global coordinate system using Equation (6.20), while the coordinates of the gate rotor in the internally geared configuration, defined in its local coordinate system S_2, can be obtained by applying the transformation matrix $\mathbf{M}_{r2}^{(I)}(\sigma_{r_2})$ given in Equation (2.5), as shown in Equation (6.27). Here, $\sigma_{r_2} = m_{21}\sigma_{r_1}$ represents the solution of the meshing condition defined in Equation (2.7).

The existence of continuous contact between the generated gate rotor and the desired main rotor for a given gearing ratio can be ensured by numerically solving Equation (6.33) for the axis distance E, where θ_t, representing the location of the transition point, is determined from Equation (6.30).

$$\gamma_2(\theta_t) = \arcsin\left(\frac{\rho_{p_2}(\theta_t)}{N_2 E}\sin\Big(\varphi_c(\theta_t)\Big)\right) \tag{6.33}$$

The main (inner) rotor coordinates in its local coordinate system S_1 can be derived using Equation (6.34), where $\mathbf{M}_{12}^{-1}(\sigma)$ denotes the transformation matrix that maps points from the gate rotor's local coordinate system into the main rotor's coordinate system. This matrix is defined as the inverse of the transformation from the main to the gate rotor's coordinate system, given in Equation (B.6). The parameter σ represents the combined solution of the meshing conditions, such that $\sigma = \sigma^*$ from Equation (6.9) when $\theta > \theta_t$ and $\dfrac{d\gamma}{d\theta}(\theta) < 0$, and $\sigma = \sigma_{r_2}$ from Equation (2.7) otherwise.

$$\begin{bmatrix} x_{r_1}^{(1)}(\theta,\sigma) & y_{r_1}^{(1)}(\theta,\sigma) & 0 & 1 \end{bmatrix}^\top = \mathbf{M}_{12}^{-1}(\sigma)\begin{bmatrix} x_{r_2}^{(2)}(\theta) & y_{r_2}^{(2)}(\theta) & 0 & 1 \end{bmatrix}^\top \tag{6.34}$$

To demonstrate the feasibility of the proposed methodology, two distinct rack profiles are used to generate pairs of internally geared rotors. The first rack profile is constructed using a sinusoidal curve, where the amplitude of the sine wave, denoted as A_s, is a controllable parameter. Another parameter influencing the resulting rotor shape is the vertical offset, k_s, which can be applied to the

y-coordinate of the rack profile in its local coordinate system. Examples of sinusoidal rack profiles generated for different amplitudes with zero offset ($k_s = 0$) in its local coordinate system are shown in Figure 6.9.

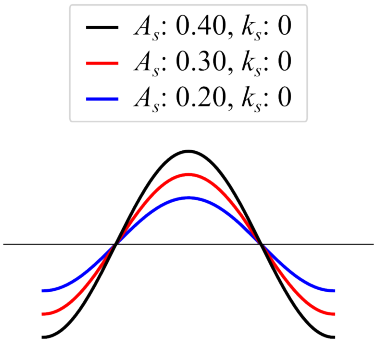

Figure 6.9: Examples of rack profiles generated using sinusoidal curves with varying amplitudes and zero vertical offset ($k_s = 0$).

The second rack profile is based on a geometric combination of two circular arcs: one arc defines the dedendum portion of the profile, while the other defines the addendum. This approach enables greater control over the curvature and overall shape of the generated profiles.

The geometry of the arc-based rack profile is defined by two non-dimensional shape parameters. The first, α_p, represents a normalised arc angle such that the true arc angle is $\alpha = \pi \cdot \alpha_p$, with $\alpha_p \in [0, 1]$. The second parameter, a_p, defines the normalised chord length of the central arc, with $a_p \in [0, 1]$. Together, these parameters control the angular span and horizontal extent of the arc segments, respectively, thereby influencing the overall profile geometry. Representation of these non-dimensional shape paremeters and their influence on rack rotor shape are shown in Figure 6.10 (a). Examples of rack profiles generated using combinations of circular arcs for various values of the non-dimensional shape parameters a_p and α_p are presented in Figure 6.10 (b).

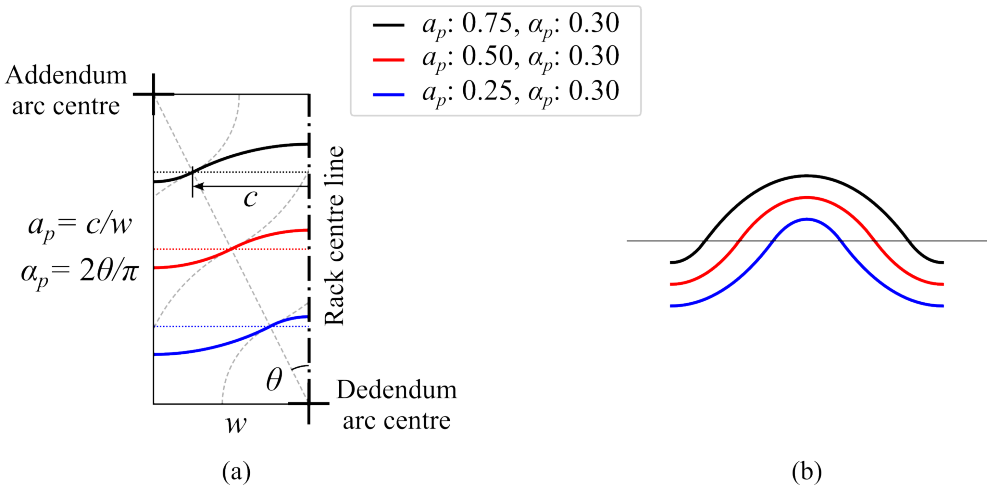

Figure 6.10: Rack rotor profiles based on geometric combination of two circular arcs: (a) representation of non-dimensional shape parameters a_p and α_p; (b) rack profiles constructed using a combination of circular arcs with varying non-dimensional shape parameters α_p and a_p.

Examples of internally geared rotor profiles generated using sinusoidal rack profile and rack profile produced by a combination of circular arcs are shown in Figure 6.11 and Figure 6.12, respectively. The resulting rotors maintain continuous contact and are suitable for various applications in positive displacement machines. However, they do not necessarily provide a zero-minimum working chamber area, which is crucial for efficient compression in internally geared screw compressors.

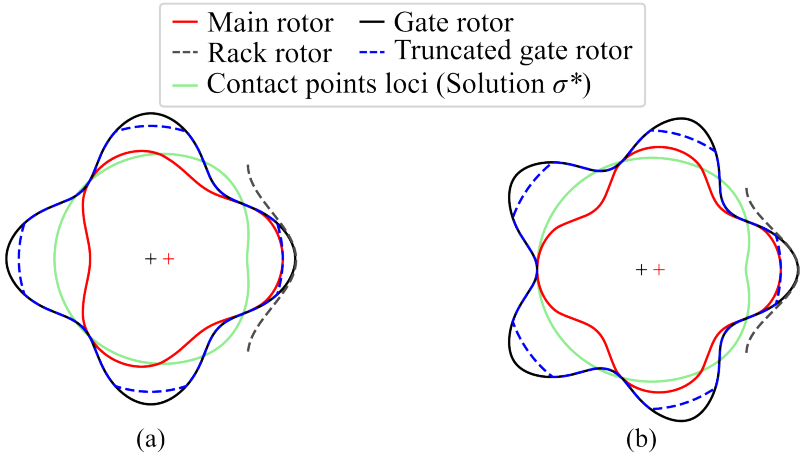

Figure 6.11: Examples of internally geared rotor profiles, where (a) $N_1 = 3$, $N_2 = 4$ and (b) $N_1 = 4$, $N_2 = 5$, both achieving continuous contact and a non-zero minimum working chamber area. The profiles are generated using a sinusoidal curve (Figure 6.9 where $A_s = 0.2, k_s = 0$) on the rack profile.

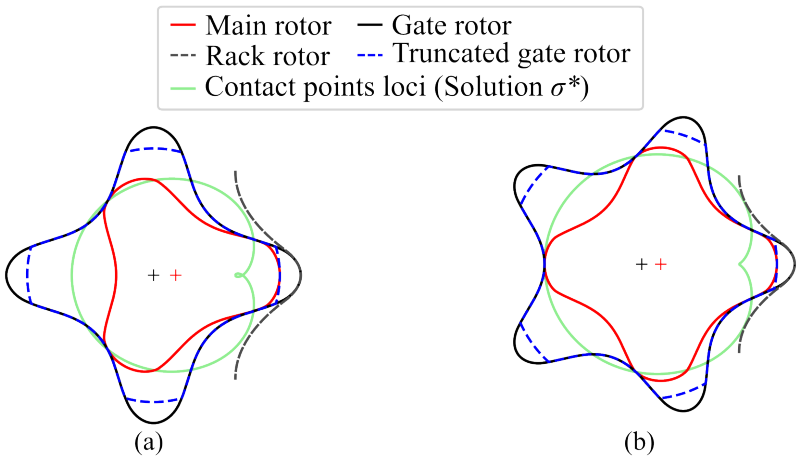

Figure 6.12: Examples of internally geared rotor profiles, where (a) $N_1 = 3$, $N_2 = 4$ and (b) $N_1 = 4$, $N_2 = 5$, both achieving continuous contact and a non-zero minimum working chamber area. The profiles are generated using a combination of circular arcs (Figure 6.10 where $a_p = 0.25, \alpha_p = 0.3$) on the rack profile.

A simple method of reducing the minimum working chamber area is to truncate the gate rotor profile using circular arc sections sized to achieve contact (or a specified gap) when the tip of the main rotor aligns with the root of the gate rotor, as shown in Figure 6.11 and Figure 6.12. However, if a zero-minimum working chamber area is crucial, this issue was previously addressed and resolved by Vecchiato et al. [28], and the same approach is applied in this paper. Once the meshing rotors are generated, a portion of the main (inner) rotor can be used to form the fillet part of the gate (outer) rotor, sealing the gap and ensuring a zero-minimum working chamber area, as described by Vecchiato et al. [28].

For the rack generated main rotor in Equation (6.34), a corresponding fillet part of the gate rotor that ensures both continuous contact and a zero-minimum working chamber area can be defined by solving the meshing condition for the main rotor using Equation (6.8) and applying Equation (6.32) to determine the fillet coordinates.

Examples of fully valid internally geared rotor profiles produced from the sinusoidal curve on the rack profile (based on the profiles from Figure 6.11) with both continuous contact and a zero-minimum working chamber area are shown in Figure 6.13. Although this procedure is demonstrated here using profiles defined by the sinusoidal rack curve, it is equally applicable to any other rack curve formulation. A comparison between the conventional rack method and the proposed internally

geared methodology is provided in Tables 6.1 and 6.2.

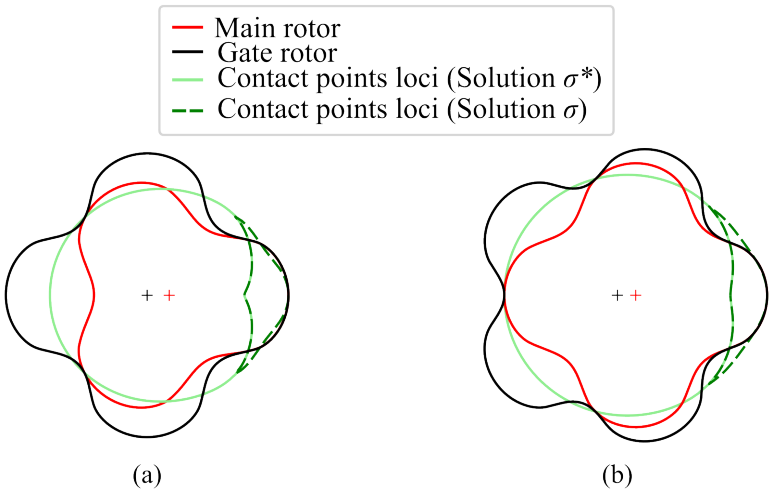

Figure 6.13: Examples of internally geared rotor profiles from Figure 6.11, where (a) $N_1 = 3$, $N_2 = 4$ and (b) $N_1 = 4$, $N_2 = 5$, incorporating a modified fillet on the gate (outer) rotor to achieve a zero minimum working chamber area.

Various curve types can be applied to different sections of the rack profile, provided they result in smooth and geometrically valid rack rotor profiles. Determining the optimal combination of such curves would require detailed optimisation studies customised to specific curve families and specific engineering applications, which is beyond the scope of this study.

Table 6.1: Main steps of the conventional rack method for the conventional twin screw rotor profile generation.

Step	**Description**
1	Generate the rack profile to be used as the generating curve for the rotor pair.
2	Derive the main rotor profile from the rack profile using the conventional rack generation procedure.
3	Derive the gate rotor profile from the rack profile using the conventional rack generation procedure.

Table 6.2: Main steps of the proposed rack method for internally geared screw machine rotor profile generation.

Step	Description
1	Generate the rack curve to be used as the initial generating curve.
2	Derive the gate rotor profile from the rack curve using the conventional rack generation procedure.
3	Derive the main rotor profile from the gate rotor while solving the necessary meshing condition to ensure continuous contact between the rotors.
4	Derive the gate rotor again from the main rotor to correct the fillet region and ensure zero minimum working chamber area.

6.2.4 Preliminary Profile Shape Evaluation

To demonstrate the capability of the proposed methodology in enabling comparative evaluation and geometrical analysis of generated profiles, a preliminary evaluation metric is defined in terms of the relative swept volume for a gerotor pump application. For each generated rotor profile, relative swept volume, $\bar{V}_{sw}$, is defined as the ratio of the total volume swept by the working chambers during one full rotation to the reference volume enclosed by the outer rotor tip cylinder. It provides a straightforward non-dimensional basis for comparing different profiles and supports preliminary parameter space exploration within selected families of rack generated profiles.

For rack profiles generated using sinusoidal curves (Figure 6.9 (a)), two shape parameters, amplitude A_s and vertical offset k_s, are varied. In the case of rack profiles constructed from a combination of circular arcs (Figure 6.9 (b)), the non-dimensional parameters a_p and α_p are varied within their allowable limits.

The influence of these parameters on the relative swept volume is illustrated in Figure 6.14 (a) and (b) for the sinusoidal and circular-arc-based rack profiles, respectively. In Figure 6.14, both cases show distinct regions where the relative swept volume varies as a function of the shape parameter combinations, demonstrating the influence of these parameters on the relative swept volume. In both cases, the maximum relative swept volume, $\bar{V}_{sw}^{max}$, reaches approximately 45% of the outer rotor tip cylinder volume. The rotor profiles corresponding to the parameter combinations that

produce the maximum relative swept volume for both sinusoidal and circular-arc-based rack configurations are shown in Figure 6.15 (a) and (b), respectively.

The circular-arc profiles remain valid across the entire parameter space, as evidenced by the continuous validity in Figure 6.14 (b). Although the sinusoidal profiles display a generally linear and smooth trend across the explored domain, some parameter combinations, however, produce undercuts that invalidate the rotor geometry (as it can be seen in Figure 6.14 (a) non valid region). Examples of these undercuts on the generated inner rotor profile (occurring for sinusoidal rack parameters within the invalid region) are shown in Figure 6.16.

These undercuts highlight limitations on parameter selection imposed by the geometrical constraints and the nature of the rack curve formulations. Such limitations must be explored in detail for specific curve families, with trends and allowable parameter bounds defined in future studies. Within this study, the rack-curve selections serve demonstration purposes only and were not chosen based on any detailed optimization or application-specific analysis.

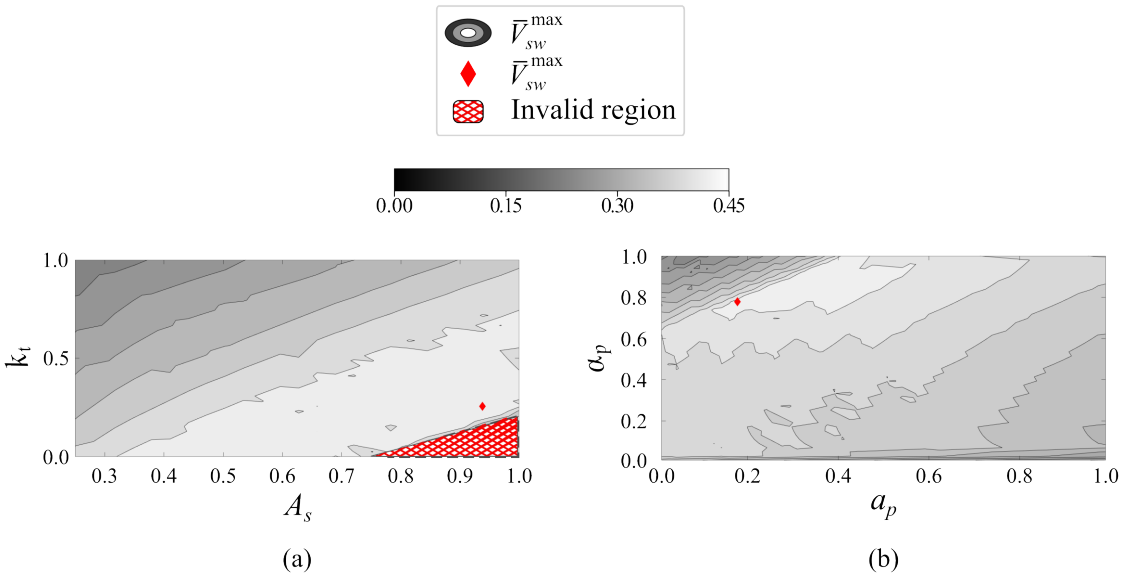

Figure 6.14: Contour plots of the relative swept volume $\bar{V}_{sw}$ as a function of rack profile parameters: (a) sinusoidal-based racks with varying amplitude A_s and vertical offset k_s; (b) circular-arc-based racks with varying non-dimensional parameters a_p and α_p.

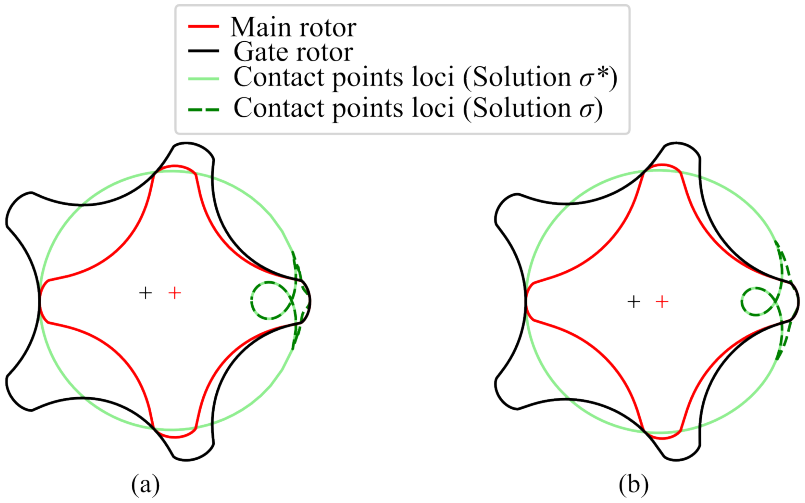

Figure 6.15: Rotor profiles corresponding to the maximum relative swept volume (Figure 6.14) for each rack configuration: (a) sinusoidal-based rack with $A_s = 0.94$ and $k_s = 0.26$ achieving $\bar{V}_{sw}^{max} = 44.7\%$; (b) circular-arc-based rack with $a_p = 0.18$ and $\alpha_p = 0.78$ achieving $\bar{V}_{sw}^{max} = 43.4\%$.

Figure 6.16: Examples of undercuts that occur on the inner rotor profiles of a sinusoidal rack generated profile for non-valid regions in Figure 6.14 (a).

6.3 Deep Neural Networks for Internally Geared Rotor Profile Generation

With advances in numerical methods and computational power, increasingly sophisticated procedures for generating rotor profiles in rotary positive displacement machines have emerged. More recently, data driven approaches have gained attention. In particular, deep neural networks, especially Generative Adversarial Networks (GANs), have been used to learn rack rotor profiles for the design of conventional twin screw rotors using the rack method [8]. This line of work opens a largely unexplored direction with substantial potential for further progress in rotor profiling.

This section presents an initial adaptation and training strategy for the GAN architecture in [8] to synthesise rotor profiles for internally geared screw machines, augmented with layers that enforce continuous contact throughout a full revolution.

6.3.1 Training Data

Deep neural networks generally require large datasets to learn meaningful features, thus a reliable rotor profiling method is essential. Here, the circular pin generation approach from Section 4.1.1 is used to produce single lobe main rotor profiles for training dataset. The profile shape is governed by the non-dimensional pair $(\lambda, \bar{\sigma})$, the main rotor lobe count N_1, and either the outer rotor diameter D_2 or the axis distance E (related via Equation (2.12)).

To simplify the initial training of rotor shapes, the lobe count is fixed at $N_1 = 4$ and the main rotor diameter at $D_1 = 1$. The varied profile parameter ranges are listed in Table 6.3, yielding 60,000 configurations.

For consistent scaling and normalisation, lobes are represented in a polar coordinate system, turning the task into learning a single period of a periodic, signal-like curve with period $T = 2\pi/N_1$ and peak-to-peak amplitude $A = 2E$. Each lobe is converted to polar coordinates and discretised with $S = 300$ samples. The dataset is stored in matrix form, one configuration per row where the first three columns contain the profile parameters $(N_1, \lambda, \bar{\sigma})$. The next block of S entries stores the radial coordinate $\rho_{1,p}$ and the final block of S entries stores the angular coordinate $\varphi_{1,p}$ of the single main rotor lobe. The row structure is illustrated in Figure 6.17.

Table 6.3: Varied parameter ranges used to generate the training set of single lobe main rotor profiles with the circular pin-generation method.

Parameter	**Symbol**	**Value**	**Note**
Main rotor lobe count	N_1	4	fixed
Outer rotor diameter	D_2	1	fixed
Pin generation parameter	λ	[1.1, 3.0]	varied
Pin generation parameter	$\bar{\sigma}$	[0.20, 0.99]	varied
Total configurations	—	**60,000**	

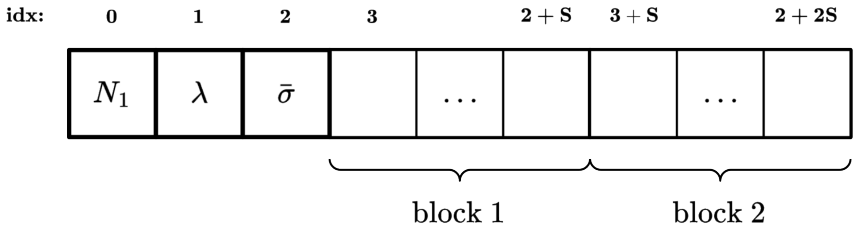

Figure 6.17: Dataset row structure for the GAN: each row encodes one single lobe main rotor profile in polar form.

Each profile lobe is scaled with a per-sample min–max method so that all values lie in $[-1, 1]$. This normalisation reduces dynamic range imbalance and helps the model distinguish shape differences rather than absolute scale. For each main rotor single lobe independently in polar form, radial and angular polar coordinates are scaled as defined in Equations (6.35) and (6.36). Figure 6.18 illustrates representative main rotor single lobe profiles before normalisation and after per-sample min–max scaling to $[-1, 1]$.

$$\rho_{\min} = \min_p \rho_{1,p}, \qquad \rho_{\max} = \max_p \rho_{1,p}, \qquad \bar{\rho}_{1,p} = 2\,\frac{\rho_{1,p} - \rho_{\min}}{\rho_{\max} - \rho_{\min}} - 1 \tag{6.35}$$

$$\varphi_{\min} = \min_p \varphi_{1,p}, \qquad \varphi_{\max} = \max_p \varphi_{1,p}, \qquad \bar{\varphi}_{1,p} = 2\,\frac{\varphi_{1,p} - \varphi_{\min}}{\varphi_{\max} - \varphi_{\min}} - 1. \tag{6.36}$$

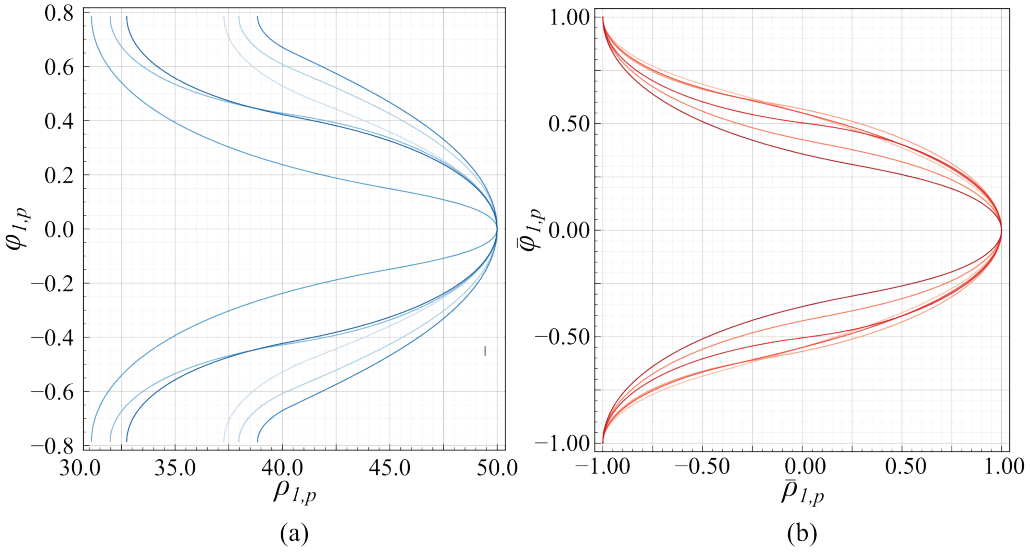

Figure 6.18: Representative main rotor single lobe profiles from the training dataset: (a) original (non-scaled) polar coordinates; (b) per-sample min–max scaled to $[-1, 1]$ for both radius and angle.

6.3.2 Model Development and Training

Motivated by prior work [8], this study adopts a Generative Adversarial Network (GAN) to synthesise rotor profiles for internally geared screw machines, while enforcing constraints that guarantee continuous contact throughout a full revolution.

A GAN is consisted of two separate neural networks trained in opposition: a generator, which produces synthetic samples intended to resemble the training data, and a critic (discriminator), which scores their realism. Through this adversarial interplay, the generator progressively improves until the synthetic outputs closely match the distribution of real samples. As the training data are unlabelled, this constitutes unsupervised learning [73]. Following [8], a Wasserstein GAN (WGAN) objective is employed to enhance stability and mitigate mode collapse.

To enforce geometric smoothness and differentiability, both essential for valid rotor profiles, a Bézier layer [74] is embedded within the generator. Representing each single lobe profile with a rational Bézier curve yields a compact parametrisation that improves training stability and reduces computational cost.

Let the control points in polar coordinates be $\{\mathbf{P}_i\}_{i=0}^{n}$, with $\mathbf{P}_i = [\rho_{p,i},\, \varphi_{p,i}]^\top$, and let the associated rational weights be $\{w_i\}_{i=0}^{n}$, constrained to $[0, 1]$. With the Bernstein basis $B_i^{(n)}(t) = \binom{n}{i} t^{\,i}(1-t)^{\,n-i}$,

the n-th degree rational Bézier curve is given by Equation (6.37), where $t \in [0, 1]$ denotes the curve parameter that increases monotonically from the start control point $\mathbf{P}_0$ at $t = 0$ to the end control point $\mathbf{P}_n$ at $t = 1$.

$$\mathbf{r}(t) = \frac{\mathbf{N}(t)}{D(t)}, \qquad \mathbf{N}(t) = \sum_{i=0}^{n} w_i \, B_i^{(n)}(t) \, \mathbf{P}_i, \qquad D(t) = \sum_{i=0}^{n} w_i \, B_i^{(n)}(t). \tag{6.37}$$

Using $B_i^{(n)\prime}(t) = n\Big(B_{i-1}^{(n-1)}(t) - B_i^{(n-1)}(t)\Big)$, the first derivative follows from the quotient rule as defined in Equation (6.38).

$$\mathbf{r}'(t) = \frac{\mathbf{N}'(t)\, D(t) - \mathbf{N}(t)\, D'(t)}{D(t)^2}, \qquad \mathbf{N}'(t) = \sum_{i=0}^{n} w_i \, B_i^{(n)\prime}(t) \, \mathbf{P}_i, \quad D'(t) = \sum_{i=0}^{n} w_i \, B_i^{(n)\prime}(t). \tag{6.38}$$

This parametrisation yields smooth, differentiable profiles with few learnable parameters, namely the control points, the weights, and the curve parameter, providing a compact basis for learning. The generator is organised into three subnetworks: one produces the Bézier parameter grid $t \in [0, 1]$, one outputs the control points $\{\mathbf{P}_i\}_{i=0}^{n}$ constrained coordinate-wise to $[-1, 1]$, and one outputs the rational weights $\{w_i\}_{i=0}^{n} \in [0, 1]$. Their outputs are passed through a Bézier layer, which, by the convex-hull property, returns a normalised rational Bézier curve $\bar{\mathbf{r}}(t) \in [-1, 1]$ and its first derivative $\bar{\mathbf{r}}'(t)$. The normalised curve is then presented to the critic, which distinguishes normalised real from synthetic profiles.

Back scaling from the normalised space is not trivial because per sample minimum and maximum of the generated curves are unknown in advance. To address this, the angular scale is fixed by the target lobe count as $s_\varphi = N_1/\pi$ (here fixed to $N_1 = 4$), while a single auxiliary head predicts the learnable radial scale $s_\rho \in [0.3, 0.5]$ mm (range selected to match the training data).

Let the normalised Bézier outputs be $\bar{\mathbf{r}}(t) = [\,\bar{\rho}(t),\, \bar{\varphi}(t)\,]^\top$ and $\bar{\mathbf{r}}'(t) = [\,\bar{\rho}'(t),\, \bar{\varphi}'(t)\,]^\top$. After determining per–coordinate scale factors $s_\rho > 0$ and $s_\varphi > 0$, the normalised Bézier output $(\bar{\rho}(t), \bar{\varphi}(t))$ with $t \in [0, 1]$ is mapped to the physical domain by diagonal scaling. The same factors apply to the derivatives as:

$$\rho(t) = s_\rho\, \bar{\rho}(t), \qquad \varphi(t) = s_\varphi\, \bar{\varphi}(t),$$
$$\rho'(t) = s_\rho\, \bar{\rho}'(t), \qquad \varphi'(t) = s_\varphi\, \bar{\varphi}'(t).$$

Equivalently, in vector form with $\mathbf{r}(t) = [\rho(t),\, \varphi(t)]^\top$ and $\bar{\mathbf{r}}(t) = [\bar{\rho}(t),\, \bar{\varphi}(t)]^\top$,

$$\mathbf{r}(t) = \begin{bmatrix} s_\rho & 0 \\ 0 & s_\varphi \end{bmatrix} \bar{\mathbf{r}}(t), \qquad \mathbf{r}'(t) = \begin{bmatrix} s_\rho & 0 \\ 0 & s_\varphi \end{bmatrix} \bar{\mathbf{r}}'(t).$$

The pair $\big(\mathbf{r}(t),\, \mathbf{r}'(t)\big)$, is passed to the penalty module that evaluates the continuous contact constraint via the geometric meshing formulation in Section 6.1. Any violation adds a penalty to the generator loss.

The critic uses four linear layers and outputs a scalar score $C(\cdot) \in \mathbb{R}$. Higher values indicate samples judged more real and lower values indicate samples judged more fake. The score is not a probability, but a Wasserstein potential whose input gradients, constrained by the 1-Lipschitz condition, provide the learning signal for the generator.

Losses and Training Objectives

Let $x \sim p_{\text{data}}$ denote a real, per sample normalised profile and $z \sim p_z$ a latent vector. The generator output is written $G(z)$ and is the normalised Bézier curve produced by the three subnetworks and the Bézier layer. Following the Wasserstein formulation with a gradient penalty, the critic is treated as a 1-Lipschitz function. With

$$\hat{x} = \epsilon\, x + (1 - \epsilon)\, G(z), \qquad \epsilon \sim \mathcal{U}(0, 1),$$

where $\mathcal{U}(0, 1)$ denotes the continuous uniform distribution on the unit interval and ϵ is a random scalar, the critic objective minimised in practice is

$$\mathcal{L}_{\text{critic}} = \mathbb{E}_{z\sim p_z}\big[C\big(G(z)\big)\big] \;-\; \mathbb{E}_{x\sim p_{\text{data}}}\big[C(x)\big] \;+\; \lambda_{\text{gp}}\, \mathbb{E}_{\hat{x}}\Big(\big\|\nabla_{\hat{x}} C(\hat{x})\big\|_2 - 1 \Big)^2,$$

where $\lambda_{\text{gp}} > 0$ weights the gradient penalty that enforces the Lipschitz constraint.

The generator is trained to increase the critic score of its outputs while satisfying the continuous contact requirement. Let $\mathcal{P}_{\text{contact}}\big(\mathbf{r}(z), \mathbf{r}'(z)\big) \geq 0$ be the penalty that measures violation of the geometric meshing condition in Section 6.1, where $\mathbf{r}(z) = \mathbf{r}(t(z))$ and $\mathbf{r}'(z) = \mathbf{r}'(t(z))$. In particular, the contact penalty includes a term based on the angle $\gamma(t)$ defined in Equation (6.28), which enforces

$$\max_{t\in[0,1]} \gamma(t) \;\to\; \frac{\pi}{2}, \qquad \min_{t\in[0,1]} \gamma(t) \;\to\; -\frac{\pi}{2}.$$

A convenient penalty that vanishes when $\gamma(t) \in [-\frac{\pi}{2},\, \frac{\pi}{2}]$ for all $t \in [0, 1]$ is

$$\mathcal{P}_{\text{contact}} = \left(\max_{t\in[0,1]} \gamma(t) - \tfrac{\pi}{2}\right)^2 + \left(\min_{t\in[0,1]} \gamma(t) + \tfrac{\pi}{2}\right)^2.$$

This yields the generator objective

$$\mathcal{L}_{\text{gen}} = \; - \mathbb{E}_{z\sim p_z}\big[C\big(G(z)\big)\big] \;+\; \lambda_{\text{c}}\, \mathbb{E}_{z\sim p_z}\Big[\mathcal{P}_{\text{contact}}\big(\mathbf{r}(z), \mathbf{r}'(z)\big)\Big], \tag{6.39}$$

where $\lambda_{\text{c}} > 0$ controls the strength of the contact constraint.

The overall network structure is shown in Figure 6.19 and the implemented hyperparameters are summarised in Table 6.4. The hyperparameter values were selected empirically by trial and error. Extracts from intermediate training states are illustrated in Figure 6.20. Four snapshots taken over 1000 iterations are shown, presenting the generated curves at each state of the trained model and demonstrating the progression during training. All curves are normalised and are displayed alongside the corresponding generated control points for each snapshot.

Figure 6.21 presents examples of generated profiles that satisfy the continuous contact condition, showcasing the ability of the network to learn constrained features specific to internally geared screw machines that are essential for the validity of the profiles.

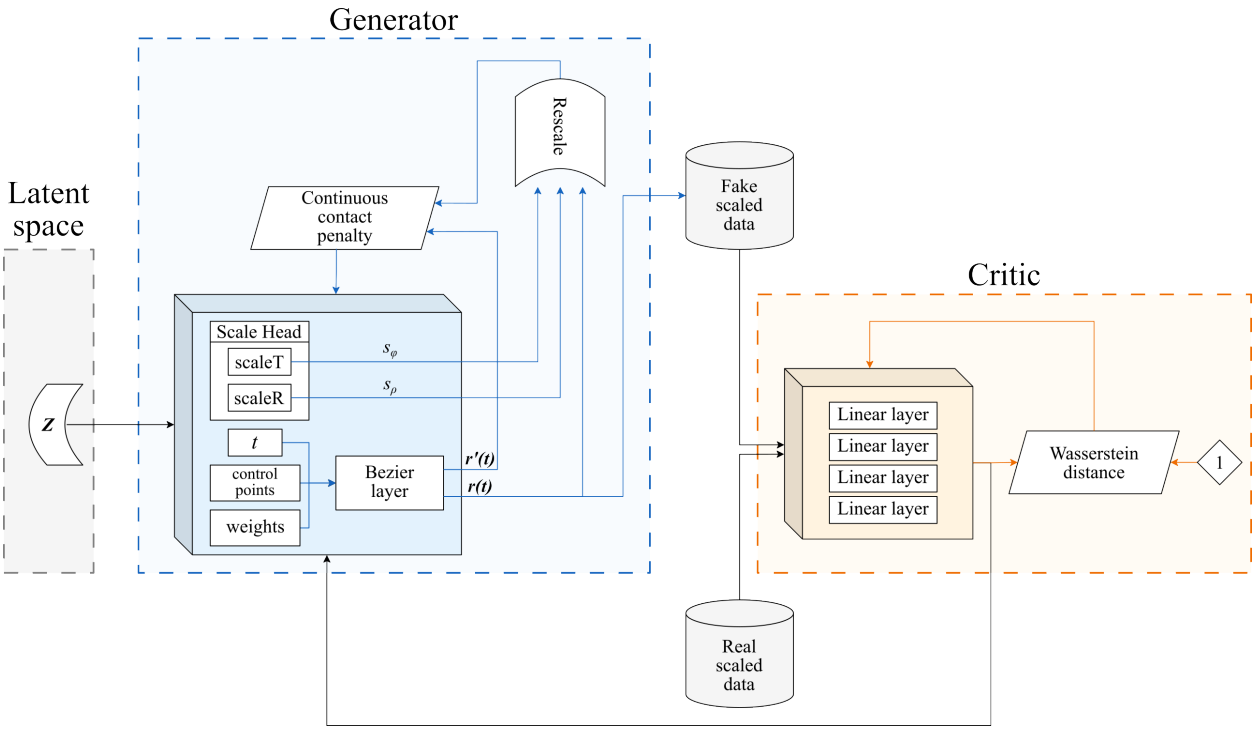

Figure 6.19: Structure of the GAN used for rotor profiling. The generator comprises three sub-networks that output the Bézier parameter grid t, control points $\{\mathbf{P}_i\}$ (constrained to $[-1, 1]$), and rational weights $\{w_i\}$. These feed a Bézier layer that produces a normalised curve $\bar{\mathbf{r}}(t)$ and derivative $\bar{\mathbf{r}}'(t)$. A radial scaling head and a fixed angular scale map the output to the physical domain for contact validation. The critic has four linear layers and outputs a scalar score $C(\cdot) \in \mathbb{R}$.

Table 6.4: Hyperparameters used in the implemented GAN. Values were determined empirically by trial and error.

Symbol / name	**Description**	**Value**
Z_{dim}	Latent vector dimension	512
n	Number of control points per lobe	20
S	Samples per lobe	300
N_1	Target lobe count	4
s_ρ range	Radial scale bounds	[0.3, 0.5] mm
s_φ	Angular scale	N_1/π
Batch size	Minibatch size	512
n_{critic}	Critic updates per generator update	3
λ_{gp}	Gradient penalty weight	20
λ_{c}	Contact penalty weight	30
Iterations	Total training steps	1000

While GAN based models are effective at learning complex geometric patterns, their outputs are inherently uncertain, since the generator can produce a range of plausible solutions within the learned distribution. The presented approach serves as a basis for further analysis of deep neural network utilisation in rotor profiling where continuous contact is required. Additional development is needed to prepare generated profiles for downstream geometry and performance analysis, to provide meaningful conditioning and context so that the network learns distributions of profiles better suited to compression applications, and to steer it towards more efficient designs. Promising directions include parallelisation of geometry calculations and the implementation of surrogate performance prediction models that can be integrated directly into the training loop as differentiable objectives or constraints.

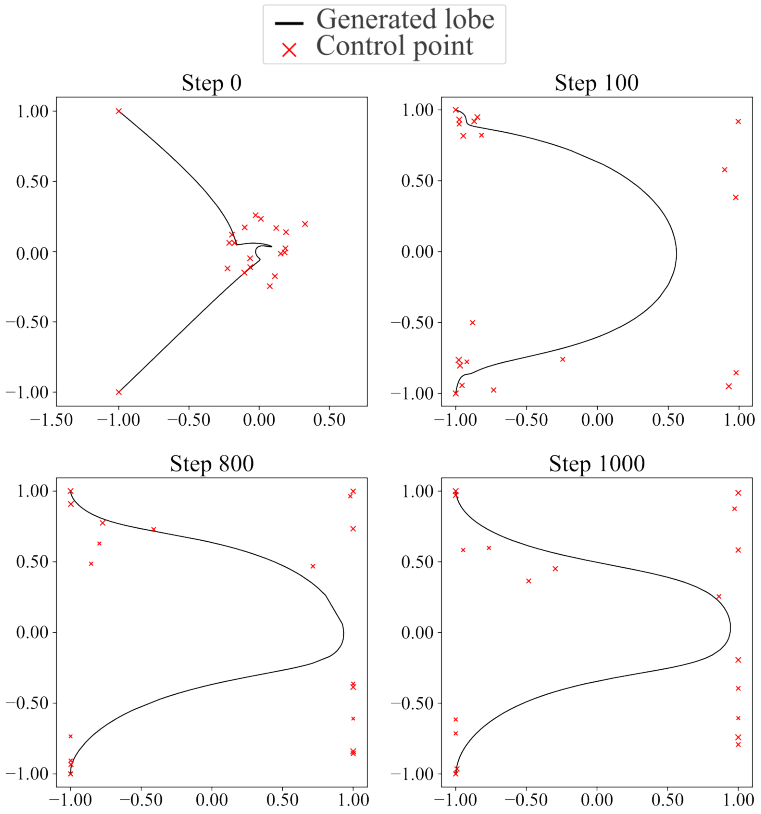

Figure 6.20: Progression of the GAN during training. Four snapshots over 1000 iterations are shown, illustrating how the generated, normalised single-lobe curves and their corresponding control points evolve from early to later stages of training.

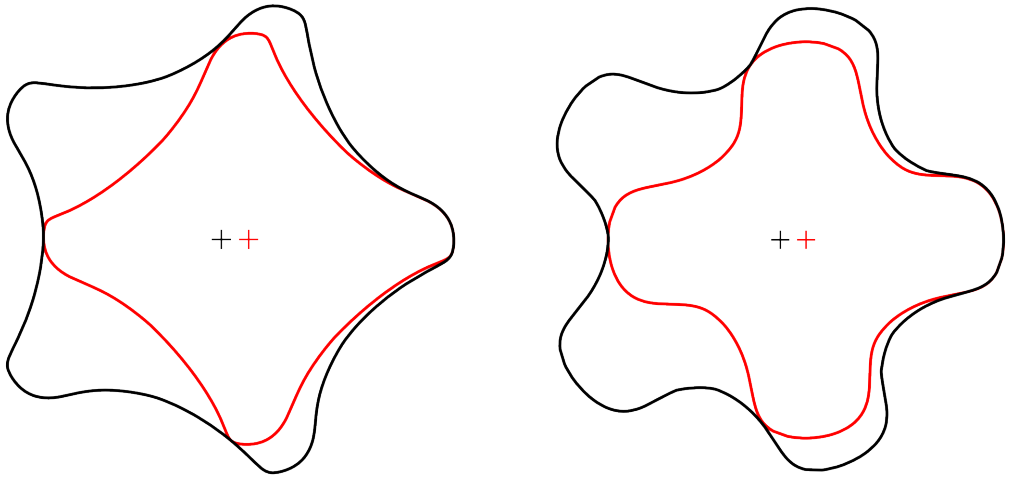

Figure 6.21: Resulting main and gate rotor profiles for $N_1 = 4$ and $N_2 = 5$. The gate rotor is obtained as the envelope of the main rotor.

6.4 Outcome

This chapter defines continuous contact for internally geared screw machine rotor profiles and states the conditions required for its existence. Building on these conditions, a rack method approach, commonly used for profile generation in conventional twin screw machines, is investigated. Although continuous contact is satisfied in the trivial case of cycloid based rack profiles, the method does not, on its own, ensure both continuous contact between the rotors and a zero minimum working chamber area, which are essential for efficient compression in internally geared screw machines.

To support generalisation of the approach, a broader cycloidal family, namely trochoids, is examined for rack profiles, and guidance is provided on constructing a main rotor from a trochoid based rack together with the derivation of the gate rotor as the envelope of the rack generated main rotor.

To further demonstrate generality, two additional rack profiles are introduced: one based on a sinusoidal curve and one formed by a combination of two circular arcs. These profiles are first assessed through swept volume analysis.

These profiles serve to illustrate the proposed approach and are not intended to be conclusive. A detailed study of rack curve combinations and their limitations should be undertaken with respect to machine performance. To enable this, the method ought to be extended to support full geometry and performance analysis for machines that employ profiles generated by this approach.

In addition, to support data driven methods, a demonstration is presented that builds on previous work applying deep neural networks to rotor profiling. The inherited network architecture is augmented with additional layers and constraints that enforce continuous contact between the rotors. This direction shows promise for generating more efficient profiles suitable for internally geared screw machine applications.

7 Conclusions and Future Work

This thesis addressed the development of geometry, profiling, and performance prediction methodologies for internally geared screw machines, with the aim of improving their analysis and supporting future design exploration. The principal objectives of the work were achieved through the development of a detailed geometry model, its integration with an established one-dimensional chamber framework, the introduction of computational acceleration strategies, and the investigation of new profiling methodologies for internally geared rotor design.

A main contribution of the thesis is the development of a generalised geometry model for internally geared screw machines capable of evaluating the phase dependent geometric quantities required for machine analysis. These include rotor profiling based on the circular pin-generation method, contact point identification and tracking, working chamber construction, helical area and volume evaluation, end port formation with port flow areas, and radial and axial leakage measures. In addition, a surrogate model for port flow area prediction based on principal component analysis and Gaussian process regression was shown to provide substantial reductions in computational cost within the studied bounds while maintaining good accuracy. This creates a practical route for accelerated exploration of large design spaces.

A further contribution is the integration of the developed geometry model with the one-dimensional multi-chamber model implemented in `SCORG`, thereby establishing an efficient performance prediction framework for internally geared screw machines. In the absence of experimental data, comparison with published computational fluid dynamics results for representative cases provided initial confidence in the predictive capability of the framework. Within the investigated bounds, the parametric studies showed that lower values of the non-dimensional pin-generation shape parameter λ tend to improve predicted efficiency, while increasing the main rotor lobe count N_1 generally reduces it. The results also indicated that a representative internally geared configuration can outperform a small scale conventional twin screw baseline in both flow and efficiency across the examined operating range, leading to lower specific power. These findings support the view that internally geared screw machines have genuine potential as efficient machines at small scale.

The thesis also advances the state of the art in rotor profiling for internally geared configurations. Conditions required for continuous rotor contact were formalised, and the rack method was extended to internally geared screw machine profiles for the first time. Analytical solutions were

presented for cycloidal and trochoidal rack forms, together with general procedures for generating valid profiles from arbitrary rack curves under the geometric constraints required for internally geared operation. The resulting profiles were assessed in terms of contact continuity and zero minimum working chamber area, which are necessary conditions for effective compression. In addition, an initial data-driven profiling strategy based on deep neural networks with embedded geometric constraints was demonstrated. Although still at an early stage, this approach showed the potential to generate feasible profiles while preserving key geometric requirements, suggesting a promising complementary route for future profile generation and exploration.

Overall, the thesis demonstrates that internally geared screw machines can be analysed using a computationally efficient integrated framework capable of supporting comparative studies, profiling development, and future optimisation. It also introduces new profiling methodologies that broaden the available design space for this machine type. Although further validation and development are still required, particularly in relation to experiments and full performance assessment of newly generated profiles, the work provides a substantial step towards reliable design and prediction tools for internally geared screw machines.

7.1 Future Work

The most immediate priority is experimental validation of the developed framework through a dedicated internally geared screw machine test facility. Measurements of mass flow, pressure, temperature, and power are needed to assess model accuracy and quantify prediction error across operating conditions. This is identified as a necessary next step in the further development of the research programme.

The port area surrogate should be extended beyond the present configuration bounds through adaptive sampling and active learning. In parallel, uncertainty quantification should be incorporated so that confidence intervals can be reported for predicted port areas and resulting performance quantities, improving reliability in future exploration and optimisation studies.

Further investigation is also required into the application range of internally geared screw machines relative to existing technologies. In particular, their potential to extend the lower size bound of conventional screw compressor designs should be assessed under realistic loss, leakage, and manufacturing constraints. Comparisons with conventional twin screw machines at larger scales and with representative scroll compressors at smaller scales would help clarify their most suitable application domain.

Finally, the new profiling directions introduced in this thesis require further development. Rack families should be explored systematically and their feasible design regions mapped in detail. The data-driven generator should be improved using larger datasets, stronger physics based constraints, and direct coupling with geometry validation and chamber model based performance assessment. This would allow future generated profiles to be evaluated not only for geometric feasibility but also for expected thermodynamic performance.

List of Publications

Journal papers

1. Lacevic, H., Kovacevic, A., Stosic, N., & Read, M. (2025). Application of rack method in generation of internally geared rotor profiles. *Mechanism and Machine Theory*, 215, 106168. https://doi.org/10.1016/j.mechmachtheory.2025.106168

2. Lacevic, H., Kovacevic, A., Rane, S., & Read, M. (2026). Geometry and performance modelling of internally geared screw machines with comparison to a conventional twin screw compressor. *Results in Engineering*, 29, 108793. https://doi.org/10.1016/j.rineng.2025.108793

Conference papers

1. Lacevic, H., Kovacevic, A., & Read, M. (2024). An investigation of internally geared screw compressor performance using a chamber modelling approach. In M. Read, S. Rane, I. Ivkovic-Kihic, & A. Kovacevic (Eds.), *Proceedings of the 13th International Conference on Compressors and Their Systems (ICCS 2023)* (Springer Proceedings in Energy). Springer, Cham. https://doi.org/10.1007/978-3-031-42663-6_40

2. Lacevic, H., Kovacevic, A., & Read, M. (2024). Optimization of internally geared screw machine geometry for an air compression application. *International Compressor Engineering Conference*, Paper 2830. https://docs.lib.purdue.edu/icec/2830

3. Lacevic, H., Kovacevic, A., Stosic, N., & Read, M. (2024). On rotor profiling of internally geared screw machines. *IOP Conference Series: Materials Science and Engineering*, 1322(1), 012006. https://doi.org/10.1088/1757-899X/1322/1/012006

4. Lacevic, H., Kovacevic, A., Read, M., Ponnusami, S.A. (2026). Rotor Profile Design for Internally Geared Screw Machines Using Deep Neural Network. In: Kovacevic, A., Read, M., Rane, S., Ivkovic-Kihic, I., Lacevic, H. (eds) 14th International Conference on Compressors and Their Systems. ICCS 2025. Springer Proceedings in Energy. Springer, Cham. https://doi.org/10.1007/978-3-032-04102-9_26

References

[1] Kui Lu, Ibrahim A. Sultan, and Truong H. Phung. A literature review of the positive displacement compressor: Current challenges and future opportunities. *Energies*, 16(20):7035, 2023. doi: 10.3390/en16207035.

[2] Nikola Stosic, Ian Smith, and Ahmed Kovacevic. *Screw Compressors: Mathematical Modelling and Performance Calculation*. Springer, Berlin, 2005. ISBN 978-3-540-24275-8. doi: 10.1007/b137216.

[3] M. G. Read, I. K. Smith, and N. Stosic. Geometrical comparison of conventional and gerotor-type positive displacement screw machines. In *IOP Conference Series: Materials Science and Engineering*, volume 604, page 011011, 2019.

[4] M. G. Read, N. Stosic, and I. K. Smith. The influence of rotor geometry on power transfer between rotors in gerotor-type screw compressors. *ASME Journal of Mechanical Design*, 142:073501, 2020.

[5] M. G. Read, I. K. Smith, and N. Stosic. Influence of rotor geometry on tip leakage and port flow areas in gerotor-type twin screw compressors. *Proceedings of the Institution of Mechanical Engineers, Part E: Journal of Process Mechanical Engineering*, 236(1):94–102, 2020. doi: 10.1177/0954408920962412.

[6] M. G. Read, I. K. Smith, and N. Stosic. Internally geared screw machines with ported end plates. In *IOP Conference Series: Materials Science and Engineering*, volume 232, page 012058, 2017.

[7] Andrew Robison. *Design of Gerotor Gear Geometry by Multi-Objective Optimization*. Ph.d. thesis, Purdue University, 2021.

[8] R. Nakka, S. Patil, A. Kovacevic, and S. A. Ponnusami. Rotor profile design of twin screw compressor using generative deep learning. In publication, 2025, 2025.

[9] A. Kovacevic, N. Stosic, and I. K. Smith. *Screw Compressors: Three-Dimensional Computational Fluid Dynamics and Solid Fluid Interaction*. Springer, 2006. ISBN 3540363025.

[10] Ivan A. Sakun. *Screw Compressors*. Mashgiz, Moscow, 1960. In Russian.

[11] P. A. Andreev. *Vintovie kompresornie machinii (Screw Compressor Machines)*. SUDPROM, Leningrad, 1961.

[12] K. Hanjalic and N. Stosic. Development and optimization of screw machines with a simulation model—part ii: Thermodynamic performance simulation and design optimization. *Journal of Fluids Engineering*, 119(3):664–670, 1997. doi: 10.1115/1.2819296.

[13] Chuang Wang, Ziwen Xing, Wenqing Chen, Qiaoming Yang, and Zhilong He. Development of an oil free water-lubricated twin-screw air compressor. *Applied Thermal Engineering*, 143:396–402, 2018. doi: 10.1016/j.applthermaleng.2018.07.119.

[14] Stuart Kennedy, Maria Wilson, and Sham Rane. Combined numerical and analytical analysis of an oil-free twin screw compressor. *IOP Conference Series: Materials Science and Engineering*, 232:012080, 2017. doi: 10.1088/1757-899X/232/1/012080.

[15] N. Stosic, Lj. Milutinovic, K. Hanjalic, and A. Kovacevic. Investigation of the influence of oil injection

upon the screw compressor working process. *International Journal of Refrigeration*, 15(4):206–220, 1992. ISSN 0140-7007. doi: https://doi.org/10.1016/0140-7007(92)90051-U.

[16] VMC Italy. *V60 Oil Injected Screw Compressor – Technical Catalogue*. VMC Italy, Italy.

[17] M. Rundo. Models for flow rate simulation in gear pumps: a review. *Energies*, 10:1261, 2017.

[18] Pedro Javier Gamez-Montero, Esteve Codina, and Robert Castilla. A review of gerotor technology in hydraulic machines. *Energies*, 12(12):2423, 2019. doi: 10.3390/en12122423.

[19] M. G. Read, I. K. Smith, and N. Stosic. Operational characteristics of internally geared positive displacement screw machines. In *International Mechanical Engineering Congress and Exposition*, page V006T08A032, New York, 2017. ASME.

[20] Leonhard Euler. De aptissima figura rotarum dentibus tribuenda [on the most suitable shape given to the teeth of wheels]. *Novi Commentarii Academiae Scientiarum Petropolitanae*, 5:176–193, 1760.

[21] F. L. Litvin. *Teoria zubchanih zaceplenii (Theory of Gearing)*. Nauka, Moscow, 2 edition, 1968.

[22] F. L. Litvin and P. H. Feng. Computerized design, generation, and simulation of meshing of rotors of screw compressor. *Mechanism and Machine Theory*, 32:137–160, 1997.

[23] D. Zaytsev and C. A. Infante Ferreira. Profile generation method for twin screw compressor rotors based on the meshing line. *International Journal of Refrigeration*, 28:744–755, 2005.

[24] L. Rinder. Screw compressor rotors with involute lobes. In *VDI Tagung Schraubenmaschinen 84*, number 521 in VDI Report, 1984.

[25] Nikola Stosic and Kemal Hanjalic. Development and optimization of screw machines with a simulation model—part i: Profile generation. *Journal of Fluids Engineering*, 119(3):659–663, 1997. doi: 10.1115/1.2819295.

[26] J. R. Colbourne. The geometry of trochoid envelopes and their application in rotary pumps. *Mechanism and Machine Theory*, 9:421–435, 1974.

[27] J. E. Beard, D. W. Yannitell, and G. R. Pennock. The effects of the generating pin size and placement on the curvature and displacement of epitrochoidal gerotors. *Mechanism and Machine Theory*, 27: 373–389, 1992.

[28] D. Vecchiato, A. Demenego, J. Argyris, and F. L. Litvin. Geometry of a cycloidal pump. *Computer Methods in Applied Mechanics and Engineering*, 190:2309–2330, 2001.

[29] Shih-Hsi Tong, Jun Yan, and Daniel C. H. Yang. Design of deviation-function based gerotors. *Mechanism and Machine Theory*, 44(8):1595–1606, 2009. doi: 10.1016/j.mechmachtheory.2009.01.001.

[30] Jia Yan, Daniel C. H. Yang, and Shih-Hsi Tong. On the generation of analytical noncircular multilobe internal pitch curves. *Journal of Mechanical Design*, 130(9):092601, 2008. doi: 10.1115/1.2943298.

[31] Daniel C. H. Yang, Jia Yan, and Shih-Hsi Tong. Flowrate formulation of deviation function based gerotor pumps. *Journal of Mechanical Design*, 132(6):064503, 2010. doi: 10.1115/1.4001595.

[32] Hao Cai, Zhiqiang Li, and Yujie Zhang. Design of gerotor oil pump with new rotor profile for improving performance. *Proceedings of the Institution of Mechanical Engineers, Part C: Journal of Mechanical*

Engineering Science, 229(6):1061–1071, 2015. doi: 10.1177/0954406215618228.

[33] Mohammad Reza Karamooz. Elliptical lobe shape gerotor pump design to minimize wear. *Frontiers of Mechanical Engineering*, 6:429–434, 12 2011. doi: 10.1007/s11465-011-0247-6.

[34] Halil Lacevic, Ahmed Kovacevic, and Matthew Read. An investigation of internally geared screw compressor performance using a chamber modelling approach. In Matthew Read, Shashank Rane, Ivona Ivkovic-Kihic, and Ahmed Kovacevic, editors, *13th International Conference on Compressors and Their Systems. ICCS 2023*, Springer Proceedings in Energy. Springer, Cham, 2024. doi: 10.1007/978-3-031-42663-6_40.

[35] Halil Lacevic, Ahmed Kovacevic, and Matthew Read. Optimization of internally geared screw machine geometry for air compression application. In *Proceedings of the 25th International Compressor Engineering Conference at Purdue*, West Lafayette, Indiana, 2024.

[36] Matthew Read. Epitrochoidal gerotor profiles with asymmetric lobes. In *International Compressor Engineering Conference*, 2022. Paper 2788.

[37] D. Genta, G. Ghigo, M. Milanese, and A. Pennacchi. Influence of rotor profile geometry on the performance of an original low-pressure gerotor pump. *Mechanism and Machine Theory*, 105:245–261, 2016. doi: 10.1016/j.mechmachtheory.2016.02.012.

[38] Heinz Wolfgang Guggenheimer. *Differential Geometry*. Dover Publications, New York, 1977.

[39] Nikola Stosic. On gearing of helical screw compressor rotors. *Proceedings of the Institution of Mechanical Engineers, Part C: Journal of Mechanical Engineering Science*, 212(7):587–594, 1998. doi: 10.1243/0954406981521556.

[40] Matthew Read, Nikola Stosic, and Ian Smith. Performance analysis of internally geared positive displacement machines. In *Proceedings of the 24th International Compressor Engineering Conference*. Purdue University, 2018. Paper 2532.

[41] C. F. Hsieh and Y. W. Hwang. Geometric design for a gerotor pump with high area efficiency. *Journal of Mechanical Design*, 129:1269–1277, 2007.

[42] C. F. Hsieh. Influence of gerotor performance in varied geometrical design parameters. *Journal of Mechanical Design*, 131:121008, 2009.

[43] G. P. Adams and J. E. Beard. Comparison of helical and skewed axis gerotor pumps. *Mechanism and Machine Theory*, 32:729–742, 1997.

[44] Nikola Stosic, Ian K. Smith, Ahmed Kovacevic, and Elvedin Mujic. Geometry of screw compressor rotors and their tools. *Journal of Zhejiang University-SCIENCE A*, 12:310–326, 2011. doi: 10.1631/jzus.A1000393.

[45] A. Kovačević. *Three dimensional numerical analysis for flow prediction in positive displacement screw machines*. PhD thesis, City University, London, 2002.

[46] Hitesh H. Patel, Vikas J. Lakhera, and Ahmed Kovacevic. Validation of leakage model for an oil-free twin-screw compressor. In Suvanjan Bhattacharyya and Ali Cemal Benim, editors, *Fluid Mechanics*

and Fluid Power (Vol. 2), Lecture Notes in Mechanical Engineering, pages 273–278, Singapore, 2023. Springer. ISBN 978-981-19-6970-6. doi: 10.1007/978-981-19-6970-6_49.

[47] H. H. Patel and V. J. Lakhera. A critical review of the experimental studies related to twin screw compressors. *Proceedings of the Institution of Mechanical Engineers, Part E: Journal of Process Mechanical Engineering*, 234(1):157–170, 2020. doi: 10.1177/0954408919869534.

[48] René Moineau. Gear mechanism. U.S. Patent 1,892,217, December 1932. Issued 27 Dec 1932.

[49] Lozica Ivanović and Miloš Matejić. Improving gerotor pump performance trough design, modeling and simulation. *International Journal of Fluid Power*, 21(3):327–346, 2021. doi: 10.13052/ijfp1439-9776.2132.

[50] Juan C. Pareja-Corcho, Michael Bartoň, Asier Pedrera-Busselo, Daniel Mejia-Parra, Aitor Moreno, and Jorge Posada. On shape design and optimization of gerotor pumps. *Computer Graphics Forum*, 43(5): e15140, 2024. doi: 10.1111/cgf.15140.

[51] Giovanni Jacazio and Andrea De Martin. Influence of rotor profile geometry on the performance of an original low-pressure gerotor pump. *Mechanism and Machine Theory*, 100:296–312, 2016. doi: 10.1016/j.mechmachtheory.2016.02.012.

[52] Qiuwan Du, Tianyuan Liu, Like Yang, Liangliang Li, Di Zhang, and Yonghui Xie. Airfoil design and surrogate modeling for performance prediction based on deep learning method. *Physics of Fluids*, 34 (1):015111, 2022. doi: 10.1063/5.0075784.

[53] Yang Shen, Wei Huang, Zheng-Guo Wang, Da-Fu Xu, and Chao-Yang Liu. A deep learning framework for aerodynamic pressure prediction on general three-dimensional configurations. *Physics of Fluids*, 35 (10):107111, 2023. doi: 10.1063/5.0172437.

[54] Hao Zhang. A novel deep-learning-based pressure distribution prediction approach of airfoils. *Proceedings of the Institution of Mechanical Engineers, Part G: Journal of Aerospace Engineering*, 237(16): 3786–3799, 2023. doi: 10.1177/09544100231206570.

[55] Ming-Yi Wu, Yi Wu, Xiao-Yu Yuan, Zhen-Hua Chen, Wen-Tao Wu, and Nadine Aubry. Fast prediction of flow field around airfoils based on deep convolutional neural network. *Applied Sciences*, 12(23):12075, 2022. doi: 10.3390/app122312075.

[56] S. Rane, A. Kovačević, and M. Read. Development of numerical grid and cfd model for analysis of oil-injected igsm. In M. Read, S. Rane, I. Ivkovic-Kihic, and A. Kovacevic, editors, *13th International Conference on Compressors and Their Systems (ICCS 2023)*, Springer Proceedings in Energy. Springer, Cham, 2024. doi: 10.1007/978-3-031-42663-6_41.

[57] G. Ramchandran and J. Harrison. A thermodynamic chamber modelling approach for oil-free and oil-injected twin screw compressors. *IOP Conference Series: Materials Science and Engineering*, 1180(1): 012002, 2021. doi: 10.1088/1757-899X/1180/1/012002.

[58] Sham Rane, Ahmed Kovačević, and Nikola Stošić. Grid generation for cfd analysis and design of a variety of twin screw machines. *Designs*, 3(2), 2019. doi: 10.3390/designs3020030.

[59] Kisorthman Vimalakanthan, Matthew Read, and Ahmed Kovacevic. Numerical modelling and experimental validation of twin-screw expanders. *Energies*, 13(18), 2020. doi: 10.3390/en13184700.

[60] Yiqiao Li, Xing Zhao, Shan Liu, Chen Wang, Shenqiang Shen, and Yali Guo. Review and prospects of numerical simulation research on internal flow and performance optimization of twin-screw compressors. *Energies*, 18(10), 2025. doi: 10.3390/en18102608.

[61] Huagen Wu, Hao Huang, Beiyu Zhang, Baoshun Xiong, and Kanlong Lin. Cfd simulation and experimental study of working process of screw refrigeration compressor with r134a. *Energies*, 12(11), 2019. doi: 10.3390/en12112054.

[62] Karl Pearson. Note on regression and inheritance in the case of two parents. *Proceedings of the Royal Society of London*, 58:240–242, 1895.

[63] I. T. Jolliffe and J. Cadima. *Principal Component Analysis*. Springer, 2016.

[64] J. O. Ramsay and B. W. Silverman. *Functional Data Analysis*. Springer, 2nd edition, 2005.

[65] Carl Edward Rasmussen and Christopher K. I. Williams. *Gaussian Processes for Machine Learning*. MIT Press, 2006.

[66] Radford M. Neal. *Bayesian Learning for Neural Networks*, volume 118 of *Lecture Notes in Statistics*. Springer, New York, NY, 1996. ISBN 978-0-387-94724-2. doi: 10.1007/978-1-4612-0745-0.

[67] Alexander I. J. Forrester, Andŕás Sobester, and Andy J. Keane. *Engineering Design via Surrogate Modelling: A Practical Guide*. Wiley, Chichester, UK, 2008. ISBN 978-0-470-06068-1. doi: 10.1002/9780470770801.

[68] Christopher K. I. Williams and Carl Edward Rasmussen. Gaussian processes for regression. In David S. Touretzky, Michael C. Mozer, and Michael E. Hasselmo, editors, *Advances in Neural Information Processing Systems 8*, pages 514–520, Cambridge, MA, USA, 1996. MIT Press.

[69] Xiuyong Shi, Degang Jiang, Weiwei Qian, and Yunfang Liang. Application of the gaussian process regression method based on a combined kernel function in engine performance prediction. *ACS Omega*, 7(45):41732–41743, 2022. doi: 10.1021/acsomega.2c05952.

[70] SKF. Speed limitations. URL `https://www.skf.com/group/products/rolling-bearings/principles-of-rolling-bearing-selection/bearing-selection-process/operating-temperature-and-speed/speed-limitations`.

[71] Earle Buckingham. *Analytical Mechanics of Gears*. Dover Publications, New York, 1988. ISBN 978-0486654061. Reprint of the 1949 edition, McGraw-Hill.

[72] Halil Lacevic, Ahmed Kovacevic, Nikola Stosic, and Matthew Read. On rotor profiling of internally geared screw machines. *IOP Conference Series: Materials Science and Engineering*, 1322:012006, 2024. doi: 10.1088/1757-899X/1322/1/012006.

[73] Ian Goodfellow, Jean Pouget-Abadie, Mehdi Mirza, Bing Xu, David Warde-Farley, Sherjil Ozair, Aaron Courville, and Yoshua Bengio. Generative adversarial nets. In *Advances in Neural Information Processing Systems 27 (NeurIPS 2014)*, pages 2672–2680. Curran Associates, Inc., 2014.

[74] Wenda Chen and Mark Fuge. Béziergan: Automatic generation of smooth curves from interpretable low-dimensional parameters. *arXiv preprint arXiv:1808.08871*, 2018. doi: 10.48550/arXiv.1808.08871.

[75] Faydor L. Litvin and Alfonso Fuentes. *Gear Geometry and Applied Theory*. Cambridge University Press, Cambridge, 2nd edition, 2004. ISBN 9780521815178.

[76] S. Yang, H. Ouyang, Y. Wu, L. Wang, L. Mei, and H. Wang. Cfd simulation for the internal pressure characteristics of an oil-injected twin-screw refrigeration compressor. *International Journal of Refrigeration*, 126:143–154, 2021. doi: 10.1016/j.ijrefrig.2021.01.020.

[77] Nausheen Basha, Ahmed Kovacevic, and Sham Rane. Analysis of oil-injected twin-screw compressor with multiphase flow models. *Designs*, 3(4), 2019. doi: 10.3390/designs3040054.

A Meshing Condition

Rotary positive displacement machines consist of meshing rotors that form a sequence of working chambers. To ensure proper engagement of the rotors, the *Fundamental Law of Gearing* (also referred to as the meshing condition) must be satisfied. This law states that, in order for a pair of rotors (gears) to maintain a constant velocity ratio, the common normal at the point of contact between their tooth profiles must always pass through a fixed point on the line of centres, known as the pitch point [75].

The coordinates of the pitch point, expressed in the main rotor's local coordinate system, are given in Equation (A.1), where $\varphi_1 = \varphi$ denotes the rotational position of the main rotor. The coordinates of the main rotor profile in its local system are defined in Equation (A.2), with θ representing the general curve parameter of the rotor profile. The vector from the the rotor point $\left(x_1^{S_1}(\theta),\, y_1^{S_1}(\theta)\right)$ to the pitch point $\left(p_x^{S_1}(\varphi),\, p_y^{S_1}(\varphi)\right)$ is defined in Equation (A.3). The corresponding normal vectors for each point on the main rotor are determined as shown in Equation (A.4). The general form of the meshing condition, as formulated by Vecchiato et al. [28], is expressed in Equation (A.5) where $\varphi = \sigma$ represents the solutions to the meshing condition. The same condition applies analogously to the gate rotor in its local coordinate system. This condition forms the theoretical basis for generating meshing rotor profiles in screw compressor design.

$$\mathbf{p}_1^{S_1}(\varphi) = \left[p_x^{S_1}(\varphi),\ p_y^{S_1}(\varphi),\ 0\right] \tag{A.1}$$

$$\mathbf{r}_1^{S_1}(\theta) = \left[x_1^{S_1}(\theta),\ y_1^{S_1}(\theta),\ 0\right] \tag{A.2}$$

$$\overrightarrow{\mathbf{r}_1\mathbf{p}_1^{S_1}}(\theta,\sigma) = \left[x_1^{S_1}(\theta) - p_x^{S_1}(\varphi),\ y_1^{S_1}(\theta) - p_y^{S_1}(\varphi),\ 0\right] \tag{A.3}$$

$$\overrightarrow{\mathbf{n}_1^{S_1}}(\theta) = \left[-\frac{dy_1^{S_1}(\theta)}{d\theta},\ \frac{dx_1^{S_1}(\theta)}{d\theta},\ 0\right] \tag{A.4}$$

$$\overrightarrow{\mathbf{r}_1\mathbf{p}_1^{S_1}}(\theta,\sigma) \times \overrightarrow{\mathbf{n}_1^{S_1}}(\theta) = \left(x_1^{S_1}(\theta) - p_x^{S_1}(\sigma)\right)\frac{dx_1^{S_1}(\theta)}{d\theta} + \left(y_1^{S_1}(\theta) - p_y^{S_1}(\sigma)\right)\frac{dy_1^{S_1}(\theta)}{d\theta} = 0 \tag{A.5}$$

B Transformations Between the Coordinate Systems

Rotor profile design is typically carried out in two dimensions, where the profile geometry is defined and transformations between local and global coordinate systems are applied. Depending on the machine configuration, the rotors may rotate either in the same or in opposite directions. The relationship between two coordinate systems is expressed through a transformation matrix. A general transformation matrix, $[\mathbf{R}|\mathbf{t}]$, combines a rotation matrix $\mathbf{R}$ and a translation vector $\mathbf{t}$ into a unified representation. This formulation captures both the orientation ($\mathbf{R}$) and positional displacement ($\mathbf{t}$) of an object, thereby enabling efficient manipulation of points and coordinate systems in space. Detailed descriptions of transformation theory in gear systems are provided by Litvin and Fuentes [75].

When the initial positions of the rotors are defined in their respective local coordinate systems, S_1 and S_2, their rotational motion can be represented by applying a rotation within the local system, followed by a translation to the global system. The global angular position parameter may be expressed as $\varphi = \varphi_1 = m_{21}\varphi_2$, where φ_1 and φ_2 denote the angular positions of the main and gate rotors, respectively, and m_{21} is the gearing ratio.

For conventional twin screw compressor designs, the transformation matrices that map rotor profile points from the local coordinate systems S_1 and S_2 to the global coordinate system S_f are given in Equations (B.1) and (B.2). The corresponding inverse matrices may be used to transform points from the global coordinate system back to their respective local frames.

$$\mathbf{M}_{1f}^{(C)}(\varphi) = \begin{bmatrix} \cos\varphi & \sin\varphi & 0 & 0 \\ -\sin\varphi & \cos\varphi & 0 & 0 \\ 0 & 0 & 1 & 0 \\ 0 & 0 & 0 & 1 \end{bmatrix} \tag{B.1}$$

$$\mathbf{M}_{2f}^{(C)}(\varphi) = \begin{bmatrix} \cos\big((1/m_{21})\varphi\big) & -\sin\big((1/m_{21})\varphi\big) & 0 & -E \\ \sin\big((1/m_{21})\varphi\big) & \cos\big((1/m_{21})\varphi\big) & 0 & 0 \\ 0 & 0 & 1 & 0 \\ 0 & 0 & 0 & 1 \end{bmatrix} \tag{B.2}$$

The transformation matrices for an internally geared design, which map the rotor coordinate points from their local coordinate systems S_1 and S_2 to the global coordinate system S_f, are provided in Equations (B.3) and (B.4), respectively. The corresponding inverse matrices can be used to transform points from the global coordinate system back to their respective local coordinate systems.

$$\mathbf{M}_{1f}^{(I)}(\varphi) = \begin{bmatrix} \cos\varphi & \sin\varphi & 0 & 0 \\ -\sin\varphi & \cos\varphi & 0 & 0 \\ 0 & 0 & 1 & 0 \\ 0 & 0 & 0 & 1 \end{bmatrix} \tag{B.3}$$

$$\mathbf{M}_{2f}^{(I)}(\varphi) = \begin{bmatrix} \cos\big((1/m_{21})\varphi\big) & \sin\big((1/m_{21})\varphi\big) & 0 & -E \\ -\sin\big((1/m_{21})\varphi\big) & \cos\big((1/m_{21})\varphi\big) & 0 & 0 \\ 0 & 0 & 1 & 0 \\ 0 & 0 & 0 & 1 \end{bmatrix} \tag{B.4}$$

The transformation matrices that map coordinate points from the main rotor's local coordinate system S_1 to the gate rotor's local coordinate system S_2 are provided in Equations (B.5) and (B.6) for the traditional and internally geared designs, respectively. The corresponding inverse matrices can be used to transform points from the gate rotor's local coordinate system S_2 back to the main rotor's local coordinate system S_1.

$$\mathbf{M}_{12}^{(C)}(\varphi) = \begin{bmatrix} \cos(\varphi(1+1/m_{21})) & \sin(\varphi(1+1/m_{21})) & 0 & -E\cos(\varphi(1+1/m_{21})) \\ -\sin(\varphi(1+1/m_{21})) & \cos(\varphi(1+1/m_{21})) & 0 & E\sin(\varphi(1+1/m_{21})) \\ 0 & 0 & 1 & 0 \\ 0 & 0 & 0 & 1 \end{bmatrix} \tag{B.5}$$

$$\mathbf{M}_{12}^{(I)}(\varphi) = \begin{bmatrix} \cos(\varphi(1-m_{21})) & \sin(\varphi(1-m_{21})) & 0 & E\cos(m_{21}\varphi) \\ -\sin(\varphi(1-m_{21})) & \cos(\varphi(1-m_{21})) & 0 & E\sin(m_{21}\varphi) \\ 0 & 0 & 1 & 0 \\ 0 & 0 & 0 & 1 \end{bmatrix} \tag{B.6}$$

C Existing Chamber Model

The existing chamber model solves the unsteady internal energy conservation equation, enabling the calculation of thermodynamic and fluid properties within the machine over multiple cycles until convergence is achieved [12]. This process is governed by Equation (C.1), which accounts for the energy gain due to gas inflow, denoted as $(\dot{m}h)_{\text{in}}$, and the energy loss resulting from gas outflow, given by $(\dot{m}h)_{\text{out}}$, where $\dot{m}$ is the mass flow rate and h is the specific enthalpy of the fluid. The internal energy of the gas is denoted by U, and $\dot{Q}$ represents the heat transfer between the working fluid and the compressor surroundings. Instantaneous pressure within the control volume is denoted by p, while the rate of change of volume with respect to the rotor's rotational position is expressed as $\frac{dV}{d\varphi_1}$. The angular velocity and angular position of the main rotor are denoted by ω_1 and φ_1, respectively.

$$\omega_1 \frac{dU}{d\varphi_1} = (\dot{m}h)_{in} - (\dot{m}h)_{out} + \dot{Q} - \omega_1 p \frac{dV}{d\varphi_1} \tag{C.1}$$

The mass continuity equation used in the chamber model is given by Equation (C.2), which expresses the rate of change of mass within the control volume. Both the inflow mass rate, $\dot{m}_{\text{in}}$, and the outflow mass rate, $\dot{m}_{\text{out}}$ are defined using Equation (C.3), where w is the fluid velocity, ρ is the instantaneous fluid density, and A is the corresponding flow cross-sectional area. The instantaneous density ρ is computed as the ratio of mass m to control volume V.

$$\omega_1 \frac{dm}{d\varphi_1} = \dot{m}_{\text{in}} - \dot{m}_{\text{out}} \tag{C.2}$$

$$\dot{m} = w\,\rho\,A \tag{C.3}$$

By solving the energy and continuity equations simultaneously, the model yields the variation of internal energy $U(\varphi_1)$ and mass $m(\varphi_1)$ over the rotor angle. Alongside the known chamber volume $V(\varphi_1)$, this allows for the calculation of specific internal energy $u = \frac{U}{m}$ and specific volume $v = \frac{V}{m}$. Assuming an ideal gas, the corresponding temperature T and pressure p inside the working chamber can be obtained using Equation (C.4), where γ is the adiabatic exponent and R is the gas constant. Both γ and R, as well as the values of u and v, are known or determined from the model.

$$T = (\gamma - 1)\frac{u}{R}, \qquad p = \frac{RT}{v} \tag{C.4}$$

Clearance leakage mass flow rate, denoted by $\dot{m}_l$, is expressed in terms of local variables along the leakage path using Equation (C.3). Leakage paths are assumed to have a rectangular cross-section with sealing line length L and clearance δ. The leakage velocity w_l is obtained from the differential momentum equation (Equation (C.5)), which accounts for wall friction f as a function of the local Reynolds number, Mach number and clearance gap geometry. In this formulation, dx denotes the differential path length and D_e is the equivalent hydraulic diameter.

For machines with liquid injection, the effective clearance gap is reduced by the instantaneous volume ratio of gas to the gas-liquid mixture in the working chamber. If only gas is present, this ratio is equal to 1, whereas it approaches 0 when the chamber is completely filled with liquid. During operation, it can take any value between these two limits.

$$w_l dw_l + \frac{dp}{\rho} + f\frac{w_l^2}{2}\frac{dx}{D_e} = 0. \tag{C.5}$$

Assuming an isothermal throttling process, the temperature variation of the working fluid across the leakage path is small, so the density may be treated as a function of pressure only. Under this assumption, the governing equations can be integrated over the pressure drop between the high and low pressure sides, yielding the leakage mass flow rate given in Equation (C.6), where p_2 and p_1 are

the high and low side pressures, a is the speed of sound, and ζ is a dimensionless flow-resistance parameter.

$$\dot{m}_l = A_l \rho_l w_l = A_l \sqrt{\frac{\gamma \left(p_2^2 - p_1^2\right)}{a^2 \left[\zeta + 2 \ln \left(p_2/p_1\right)\right]}}. \tag{C.6}$$

D CFD Setup for the Representative Validation Case

The main purpose of the CFD model in this study was to be able to verify the implementation of the IGSM geometry and thermodynamics calculation algorithms. Previous studies using the same CFD modelling methodology have shown that variations in integral quantities such as volumetric and adiabatic efficiency with grid density and time step size remain within 2–10% and are therefore not significant for validation purposes [76]. In this thesis, the quantities of interest are the cyclic integrals of mass flow rate and rotor torque, and the clearance gap size is predefined in the deforming mesh. In addition, the time step size is directly determined from the deforming mesh transition in degrees per step and the operating rotational speed of the inner rotor, which yields a fixed time step for each rotational speed. For these reasons, additional grid and time step independence studies have not been performed.

All wall boundaries in the CFD model are treated as adiabatic. The simulations use a pressure-based coupled transient solver with 20 iterations per time step, and a relaxation factor of 0.5 is applied to maintain stability over the pressure cycles.

A representative case study, summarised in Table 5.1 and drawn from the CFD investigation of an internally geared screw machine conducted by Rane et al. [56], is adopted to benchmark the integrated one-dimensional chamber model. The geometry and operating conditions reported in that study are used here to compare and validate model predictions. This prototype IGSM was evaluated with an oil injection located on the high-pressure end plate with the injection timed to begin at 30 degrees past the suction port closure. Main parts of the CFD model are the rotors (volume deforms with time during the simulation), suction, discharge, and oil injection ports. Additionally, the operating clearances were specified as $100\,\mu m$ between the rotors, the axial clearance at suction side was set to $100\,\mu m$ and that at the discharge end was set at $50\,\mu m$. Oil injection diameter was $5\,mm$ and the injection pressure was set equal to the discharge pressure. The description of the dry air CFD model for screw compressors [14] and two fluid CFD model suitable for oil injected compressors [77] has been used in [56] and in the current study. The same

parameters for the ANSYS CFX solver, air and oil properties have been used. Mesh deformation is managed using a user defined function, all advection and transient schemes are set to second order accuracy. The SST k-Omega turbulence model is a common practise in these models and has been applied. At the Inlet and Oil injection a total pressure and temperature boundary condition is applied, while at the outlet a static pressure is applied. Flow of the air as well as oil is produced as a solution variable. Cyclically repetitive flow field is obtained after several time steps and data from the final compression cycles is used to estimate the average performance parameters such as mass flow rate (this quantifies leakage and volumetric efficiency), indicated power, specific power, discharge temperature, oil flow rate, and adiabatic efficiency. This data is then used to verify the chamber model predictions under similar operating conditions.